

SENSING MECHANISMS OF ROUGH PLASMONIC SURFACES FOR  
PROTEIN BINDING OF SURFACE PLASMON RESONANCE DETECTION

SIRATCHAKRIT SHINNAKERDCHOKE



A THESIS SUBMITTED IN PARTIAL FULFILMENT  
OF THE REQUIREMENT FOR THE DEGREE OF  
MASTER OF ENGINEERING IN BIOMEDICAL ENGINEERING  
SCHOOL OF ENGINEERING  
KING MONGKUT'S INSTITUTE OF TECHNOLOGY LADKRABANG  
2023

KMITL-2023-EN-M-317-087

เอกสารนี้เป็นเอกสารที่สงวนไว้สำหรับการใช้งานเพื่อการศึกษาเท่านั้น ไม่อนุญาตให้นำไปใช้ประโยชน์ด้านการค้า  
ไม่ว่ากรณีใดๆ ทั้งสิ้น อีกทั้งห้ามมิให้ดัดแปลงเนื้อหา และต้องอ้างอิงถึงเจ้าของเอกสารทุกครั้งที่มีการนำไปใช้



COPYRIGHT 2023

SCHOOL OF ENGINEERING

KING MONGKUT'S INSTITUTE OF TECHNOLOGY LADKRABANG

เอกสารนี้เป็นเอกสารที่สงวนไว้สำหรับการใช้งานเพื่อการศึกษาเท่านั้น ไม่อนุญาตให้นำไปใช้ประโยชน์ด้านการค้า  
ไม่ว่ากรณีใดๆ ทั้งสิ้น อีกทั้งห้ามมิให้ดัดแปลงเนื้อหา และต้องอ้างอิงถึงเจ้าของเอกสารทุกครั้งที่มีการนำไปใช้

Thesis	Sensing Mechanisms of Rough Plasmonic Surfaces for Protein Binding of Surface Plasmon Resonance Detection
Student	Mr. Siratchakrit Shinnakerdchoke
Student ID.	65016097
Degree	Master of Engineering
Program	Biomedical Engineering
Year	2023
Thesis Advisor	Asst. Prof. Dr. Treesukon Treebupachatsakul
Thesis Co-Advisor	Asst. Prof. Dr. Suejit Pechprasarn

## ABSTRACT

SPR (surface plasmon resonance) has been employed in a variety of optical applications, including biosensors. Because of its ultrasensitivity on the plasmonic metal surface, the SPR-based sensor is the gold standard for protein kinetic monitoring. However, even minor modifications to surface morphology, such as roughness or pattern, may result in a substantial effect on performance. The objective of this investigation is to propose a theoretical framework to clarify sensing mechanisms and quantifying sensing performance parameters of angular surface plasmon resonance detection for binding kinetic sensing at different levels of surface roughness. Two models were used in the theoretical study: a protein layer coating on a rough plasmonic surface with and without sidewall coatings. The two models allow us to separate and quantify the enhancement factors caused by localized surface plasmon polaritons at the rough surfaces' sharp edges, as well as the increased surface area for protein binding produced by roughness. To create rough metal surfaces, the Gaussian random surface technique was utilized. Rigorous coupled-wave analysis and Monte Carlo simulation were employed to simulate and quantify reflectance spectra and quantitative performance parameters. Plasmonic angle, sensitivity, intensity contrast, full width at half maximum, and figure of merits are among the parameters. Depending on the roughness levels, roughness can have a crucial influence on the intensity measurement of binding kinetics, either positively or negatively. A tradeoff between

เอกสารนี้เป็นเอกสารที่สงวนไว้สำหรับการใช้งานเพื่อการศึกษาเท่านั้น ไม่นิยมนำไปเผยแพร่โดยไม่ได้รับอนุญาต  
ไม่ว่ากรณีใดๆ ทั้งสิ้น อีกทั้งห้ามมิให้ดัดแปลงเนื้อหา และต้องอ้างอิงถึงเจ้าของเอกสารทุกครั้งที่มีการนำไปใช้

sensitivity and increased roughness results in a widened plasmonic reflectance dip as a result of increased scattering loss. Some roughness profiles can produce negative and increased sensitivity without broadening the SPR spectra. We also discuss how the enhanced sensitivity of rough surfaces is primarily due to the localized surface wave, rather than increased binding domain density.



เอกสารนี้เป็นเอกสารที่สงวนไว้สำหรับการใช้งานเพื่อการศึกษาเท่านั้น ไม่อนุญาตให้นำไปใช้ประโยชน์ด้านการค้า  
ไม่ว่ากรณีใดๆ ทั้งสิ้น อีกทั้งห้ามมิให้ดัดแปลงเนื้อหา และต้องอ้างอิงถึงเจ้าของเอกสารทุกครั้งที่มีการนำไปใช้

## ACKNOWLEDGEMENTS

First and foremost, I would like to express my heartfelt gratitude to my advisor, Asst. Prof. Dr Treesukon Treebupachatsakul for providing me with ongoing support, vast knowledge, and access to laboratory and research facilities while guiding me through this master's degree research project. This research project would not have been completed without her assistance at every stage.

In addition, I would like to sincerely thank Assc. Prof. Dr Suejit Pechprasarn, who provided guidance, valuable suggestions, and encouragement. This research would not have been possible without his support. I must also thank my family and friends for their unwavering support during these intense academic years.

Lastly, I acknowledge the research funding supported by a scholarship from King Mongkut's Institute of Technology Ladkrabang, contract number KREF016601, and the College of Biomedical Engineering, Rangsit University (RSU).

Siratchakrit Shinnakerdchoke

## TABLE OF CONTENTS

	Page
ABSTRACT .....	i
ACKNOWLEDGEMENTS .....	iii
TABLE OF CONTENTS .....	iv
LIST OF TABLES .....	vii
LIST OF FIGURES .....	viii
LIST OF SYMBOLS / ABBREVIATIONS .....	xii
CHAPTER 1 INTRODUCTION .....	1
1.1 Background of Research .....	1
1.2 Objectives .....	3
1.3 Hypothesis .....	3
1.4 Research Scope .....	3
1.5 Research Plan .....	4
CHAPTER 2 RELATED THEORIES .....	5
2.1 Theories of Light .....	5
2.1.1 Corpuscular Theory .....	5
2.1.2 Wave Theory .....	7
2.1.3 Electromagnetic Theory .....	7
2.1.4 Quantum Theory .....	7
2.2 Properties of Light .....	8
2.2.1 Electromagnetic Properties .....	8
2.2.2 Reflection and Refraction of Light .....	10
2.2.3 Dispersion of Light .....	10
2.2.4 Polarization of Light .....	11
2.3 Total Internal Reflection .....	12
2.4 Evanescent Wave .....	13
2.5 Surface Plasmon Resonance Theory .....	18
2.5.1 Surface Plasmon Excitation .....	20
2.6 Surface Plasmon Resonance Experiment .....	22
2.6.1 Protein Binding Application in SPR Detection .....	23
2.7 Quantitative Sensing Performance Parameters .....	26

เอกสารนี้เป็นเอกสารที่สงวนไว้สำหรับการใช้งานเพื่อการศึกษาเท่านั้น ไม่อนุญาตให้นำไปใช้ประโยชน์ด้านการค้า  
ไม่ว่ากรณีใดๆ ทั้งสิ้น อีกทั้งห้ามมิให้ดัดแปลงเนื้อหา และต้องอ้างอิงถึงเจ้าของเอกสารทุกครั้งที่มีการนำไปใช้

2.7.1 Plasmonic Angle .....	26
2.7.2 Sensitivity .....	27
2.7.3 Full Width at Half Maximum .....	28
2.7.4 Intensity Contrast .....	29
2.7.5 Plasmonic Intensity .....	29
2.7.6 Figure of Merit .....	30
CHAPTER 3 METHODOLOGY .....	31
3.1 Simulation of Rough Surface Structures .....	31
3.2 Simulated Structures for Rigorous Coupled-Wave Analysis .....	32
3.2.1 Identifying and Quantifying the Roots of Changes in Performance .....	32
3.2.2 Theoretically Investigated SPR-based Sensor .....	34
3.2.3 Simulation of the SPR Detection .....	35
3.3 Enhancement and Deterioration Ratio .....	36
CHAPTER 4 RESULTS .....	37
4.1 Convergence Test .....	37
4.2 Simulation VS Experiment .....	38
4.3 Quantitative Performance Parameters for Investigated Surfaces .....	39
4.3.1 Quantitative Performance for Ideal Uniform Gold Sensor .....	39
4.3.2 Rough SPR-based Sensor: Plasmonic Angle .....	39
4.3.3 Rough SPR-based Sensor: Sensitivity .....	40
4.3.4 Rough SPR-based Sensor: Full Width at Half Maximum .....	44
4.3.5 Rough SPR-based Sensor: Intensity Contrast .....	44
4.3.6 Rough SPR-based Sensor: Plasmonic Intensity .....	45
4.3.7 Rough SPR-based Sensor: Figure of Merits .....	46
4.3.8 Rough SPR-based Sensor: Performances of Operating Surfaces and Their EDRs .....	47
4.3.9 Linearity Test .....	49
CHAPTER 5 DISCUSSION .....	51
5.1 The LSPR Effect and Sidewall Protein Increment .....	51
5.2 Intensity and Phase Detection .....	51
5.3 Field Plots of SPR-based Sensor Structures .....	52
CHAPTER 6 CONCLUSION .....	55
REFERENCES .....	57

เอกสารนี้เป็นเอกสารที่สงวนไว้สำหรับการใช้งานเพื่อการศึกษาเท่านั้น ไม่อนุญาตให้นำไปใช้ประโยชน์ด้านการค้า  
ไม่ว่ากรณีใดๆ ทั้งสิ้น อีกทั้งห้ามมิให้ดัดแปลงเนื้อหา และต้องอ้างอิงถึงเจ้าของเอกสารทุกครั้งที่มีการนำไปใช้



เอกสารนี้เป็นเอกสารที่สงวนไว้สำหรับการใช้งานเพื่อการศึกษาเท่านั้น ไม่อนุญาตให้นำไปใช้ประโยชน์ด้านการค้า  
ไม่ว่ากรณีใดๆ ทั้งสิ้น อีกทั้งห้ามมิให้ดัดแปลงเนื้อหา และต้องอ้างอิงถึงเจ้าของเอกสารทุกครั้งที่มีการนำไปใช้

## LIST OF TABLES

Table	Page
Table 1.1 Shows the RMS Roughness values for different surface treatment techniques .....	2
Table 1.2 Shows research plan for the theoretical investigation .....	4
Table 4.1 Indicates the plasmonic angle obtained from an experiment proceeded by Yang et al. [108] and the RCWA simulation for the purposed rough surfaces .....	39
Table 4.2 Shows the lists of performance parameters obtained from the five proposed operating surfaces .....	48
Table 4.3 Shows the <i>EDR</i> for different operating surfaces and its quantification for $EDR_{LSPR}$ and $EDR_{protein}$ .....	49

เอกสารนี้เป็นเอกสารที่สงวนไว้สำหรับการใช้งานเพื่อการศึกษาเท่านั้น ไม่อนุญาตให้นำไปใช้ประโยชน์ด้านการค้า  
ไม่ว่ากรณีใดๆ ทั้งสิ้น อีกทั้งห้ามมิให้ดัดแปลงเนื้อหา และต้องอ้างอิงถึงเจ้าของเอกสารทุกครั้งที่มีการนำไปใช้

## LIST OF FIGURES

Figure	Page
Figure 2.1 Shows schematics of (a) the law of reflection and (b) the law of refraction for the corpuscular theory .....	5
Figure 2.2 Shows the structure of an electromagnetic wave generated from the oscillation of a molecular dipole .....	9
Figure 2.3 Shows a schematic of an incident light approaching an interface between media, resulting in a reflected and a transmitted (refracted) light .....	10
Figure 2.4 Shows a schematic of white light entering a glass prism and diffracting into different colour beams .....	11
Figure 2.5 Shows schematics of (a) linearly polarized and (b) circular polarized electromagnetic waves .....	11
Figure 2.6 Shows schematics of (a) TE-polarized light and (b) TM-polarized light as it enters a different medium .....	12
Figure 2.7 Shows the reflectivity of TM (red line) and TE-polarized light (blue line) as it approaches an interface between media at different incident angles. Note that $\theta_c$ , $\theta_p$ , $\theta_B$ indicate a critical angle, a principal angle, and Brewster's angle, respectively .....	13
Figure 2.8 Shows the parallel and perpendicular evanescent intensity at multiple incident angles at $n$ of 0.887, which corresponds to $\theta_c$ of $62.46^\circ$ .....	15
Figure 2.9 Shows the schematics of (a) a Goos-Hanchen shift at the total reflection between two media and (b) electric field vectors of an incident and evanescent light with the $\parallel$ polarization. Note that the vectors refer to the $z=0$ position, and $\delta_{\parallel}$ indicates the phase lag .....	17
Figure 2.10 Shows schematics of (a) surface plasmon polariton along the metallic layer and (b) localized surface plasmon resonance around the metallic nanoparticle .....	18
Figure 2.11 Shows (a) a graphical illustration of a dispersion relation for surface plasmons where lines "a" and "b" indicate a dispersion relation for normal light in regions with $\epsilon_2$ and $\epsilon_1$ , respectively, and corresponds to an incident	

angle $\theta_i$ ; and (b) an experimental setup which yields dispersion relation curves shown previously .....	21
Figure 2.12 Shows (a) the Kretschmann configuration for an SPR-based sensor and (b) the SPR response with a sensing region as air (refractive index of 1.00) ...	22
Figure 2.13 Shows (a) the change in plasmonic angle during the baseline (1), association (2), disassociation (3), and regeneration (4) of a kinetic binding experiment, and (b) a schematic of protein binding during each phase .....	23
Figure 2.14 Shows the sensorgram's plots of the plasmonic angle responses for protein binding with different concentrations .....	25
Figure 2.15 Shows the SPR responses from an ideal uniform gold sensor (blue) and a rough gold sensor (red) which indicate the difference between their detection ranges .....	26
Figure 2.16 Shows schematics of (a) a bulk sensitivity detection and (b) a binding sensitivity detection with an initial sensing region as a water-based environment and an alternated sensing region as BSA solution (bulk) and BSA binding layer (binding) .....	27
Figure 2.17 Shows (a) a schematic of the <i>FWHM</i> measurement for SPR detection and (b) a comparison between small and large <i>FWHM</i> responses simulated from an air-based and water-based sensing region, respectively. Note that the angular scanning ranges are identical .....	28
Figure 2.18 Shows (a) a schematic of the $\Delta I$ measurement for SPR detection and (b) a comparison between strong and weak $\Delta I$ responses simulated from an ideal SPR-based sensor and a sensor with 20% degraded in the intensity, respectively .....	29
Figure 2.19 Shows a schematic of the $I_{SP}$ measurement for SPR detection .....	30
Figure 3.1 Shows the process of the Gaussian random surfaces technique, which includes (a) an illustration of function $d(x)$ , (b) a multiplication step of $D(\omega)$ and $Z(\omega)$ , and (c) the resulting surface profile, $s(x)$ .....	31
Figure 3.2 Shows schematics of (a) the rough bare gold model, (b) the BSA with no sidewall model, and (c) the BSA with sidewall model, simulated using $h$ of 18 nm and $cl$ of 10 nm, and their zoom-in visuals of the surface structures .....	33
Figure 3.3 Shows the SPR-based sensor structure which was employed in the theoretical investigation .....	34

Figure 3.4 Shows the flowchart which represents the procedures for the theoretical investigation [106] .....	35
Figure 4.1 Shows results of (a) a convergence test on the number of diffraction orders and (b) a convergence test on the number of columns employed for four extreme cases of roughness profile [106] .....	37
Figure 4.2 Shows the SPR spectra simulated based on the proposed roughness parameters reported by Yang et al. [106,108] .....	38
Figure 4.3 Shows (a) the average plasmonic angle as $n_0 \sin \theta_{sp}$ for different roughness profiles, and (b) the SPR spectra simulated from surfaces with $h$ of 0 nm (ideal uniform surface), 5 nm, 15 nm, and 20 nm, and equivalent $cl$ of 20 nm [106] .....	40
Figure 4.4 Shows the sensitivity in $\text{rad}/\mu\text{m}^2$ obtained at different roughness profiles from (a) the BSA with no sidewall model and (b) the BSA with sidewall model [106] .....	40
Figure 4.5 Shows the reflectance spectra obtained from (a) the operating surface “i”, (b) the operating surface “ii”, (c) the operating surface “iii”, (d) the operating surface “iv”, and (e) the operating surface “v”. Note that the dashed lines indicate the SPR response from the theoretical smooth surface sensor [106] .....	42
Figure 4.6 Shows the protein increment in percent due to the presence of sidewall protein on roughness profiles [106] .....	43
Figure 4.7 Shows the average $FWHM$ of SPR responses from BSA with no sidewall and BSA with sidewall models at different roughness levels [106] .....	44
Figure 4.8 Shows the average $\Delta I$ of SPR-based sensor outputs simulated based on BSA with no sidewall and BSA with sidewall models [106] .....	45
Figure 4.9 Shows the average $I_{sp}$ of SPR-based sensor responses obtained from BSA with no sidewall and BSA with sidewall models [106] .....	45
Figure 4.10 Shows the (a) $FOM_0$ for the BSA with no sidewall model and (b) the BSA with sidewall model, and (c) the $FOM_{SPR}$ for the BSA with no sidewall model and (d) the BSA with a sidewall model in different roughness levels [106] .....	46
Figure 4.11 Shows the linearity test of sensitivity and varying the BSA thickness for the ideal uniform gold model, the BSA with no sidewall model, and the	

เอกสารนี้เป็นเอกสารที่สงวนไว้สำหรับการใช้งานเพื่อการศึกษาเท่านั้น ไม่อนุญาตให้นำไปใช้ประโยชน์ด้านการค้า  
ไม่ว่ากรณีใดๆ ทั้งสิ้น อีกทั้งห้ามมิให้ดัดแปลงเนื้อหา และต้องอ้างอิงถึงเจ้าของเอกสารทุกครั้งที่มีการนำไปใช้

BSA with sidewall model with roughness employed as the operating surface “iv” [106] .....	49
Figure 5.1 Shows the results for (a) intensity detection and (b) phase detection for the purposed operating surfaces [106] .....	52
Figure 5.2 Shows the intensity of electric fields represent as $ E_x ^2 +  E_z ^2$ for (a) the ideal uniform surface sensor, (c) the SPR-based sensor with gratings structure, and (c) the SPR-based sensor with roughness as $h$ of 9 nm and $cl$ of 8 nm (operating point “iv”) [106] .....	53



## LIST OF SYMBOLS / ABBREVIATIONS

Symbols/Abbreviations	Terms
SPR	Surface plasmon resonance
LSPR	Localized surface plasmon resonance
BSA	Bovine serum albumin
TM	Transverse magnetic
TE	Transverse electric
TIR	Total internal reflection
TIRF	Total internal reflection fluorescence
SPP	Surface plasmon polariton
CFCA	Calibration-free concentration analysis
$\theta_{sp}$	Plasmonic/Resonance angle
FWHM	Full width at half maximum
$\Delta I$	Intensity contrast
$I_{sp}$	Plasmonic intensity
FOM	Figure of merit
h	Roughness height
cl	Roughness correlation length
RCWA	Rigorous coupled-wave analysis
RWG	Resonance wave gratings
MADG	Metal-layer-assisted double-grating
HeNe	Helium-Neon
EDR	Enhancement and Deterioration Ratio
RMS	Root-mean-square
AFM	Atomic force microscope
NA	Numerical Aperture

เอกสารนี้เป็นเอกสารที่สงวนไว้สำหรับการใช้งานเพื่อการศึกษาเท่านั้น ไม่อนุญาตให้นำไปใช้ประโยชน์ด้านการค้า  
ไม่ว่ากรณีใดๆ ทั้งสิ้น อีกทั้งห้ามมิให้ดัดแปลงเนื้อหา และต้องอ้างอิงถึงเจ้าของเอกสารทุกครั้งที่มีการนำไปใช้

# CHAPTER 1

## INTRODUCTION

### 1.1 Background of the Research

Surface plasmon resonance (SPR) is a guided electromagnetic phenomenon that occurs when electrons oscillate between a noble metal, such as gold, silver, and bronze, and a dielectric [1]. This effect commonly initiates from the illumination of an external electric field from an incident light with a matching momentum [2]. A dark band is produced in the plasmonic reflectance spectra due to optical energy absorption caused by the coupling between the incident photon and electron oscillation [3]. The development of sensors based on SPR and many other optical sensing technologies has been prompted by the coupling of SPR's potential for real-time monitoring and hyper-sensitivity measurement of binding interactions [4]. Host-pathogen detection [5,6], biochemical interactions [7,8], refractive index sensing [9,10], drug discovery [11,12], microscopic imaging [13], therapeutic monitoring [14], ultrasonic detection [15], and voltage sensing [16] are a few examples of applications using SPR. Despite the advantages and versatilities of SPR detection, the sensor has a crucial drawback from its hyper-sensitivity property. A slight change within the sensor's compositions, for example, the material's purity, the fingerprint on a glass prism, and the surface profile (roughness), can significantly impact the SPR output.

A commonly utilized SPR-based sensor comprises a glass substrate, a noble metal film, and a sensing region. This structure is also known as the Kretschmann configuration [17]. In addition, there are numerous techniques for SPR detection, such as wavelength scanning detection [18], intensity detection [19], and phase detection [20]. In this thesis, the mainly investigated SPR detection technique is so-called angular scanning [21]. The sensor's structure and measurement schemes will be explained in detail in later sections.

Multiple studies [22-27] have found that the surface profile of the metal film, including its thickness and roughness, significantly impacts the performance of the SPR-based sensor for bulk refractive index sensing. For instance, Kurihara et al. [26] explained that SPR dips could be classified into small, large, and equivalent absorption and excitation frequency relationships, depending on the frequency correlation between the optical property of the light source and the thickness of the metal layer. Moreover, Hoffman et

เอกสารนี้เป็นเอกสารที่สงวนไว้สำหรับการใช้งานเพื่อการศึกษาเท่านั้น ไม่อนุญาตให้นำไปใช้ประโยชน์ด้านการค้า  
ไม่ว่ากรณีใดๆ ทั้งสิ้น อีกทั้งห้ามมิให้ดัดแปลงเนื้อหา และต้องอ้างอิงถึงเจ้าของเอกสารทุกครั้งที่มีการนำไปใช้

al. [25] found that the dielectric functions and SPR wave vectors changed significantly as the roughness amplitudes increased. Our recent investigation [27] has also discovered that the sensitivity, full width at half maximum, intensity contrast, plasmonic dip position, and figure of merit of the refractive index measurement strongly degrade when using an SPR-based sensor with rough gold films.

According to several papers [28,29], the sensitivity of binding kinetic measurement increases with roughness level due to a larger surface area and more protein in contact with the plasmonic metal. It is worth mentioning that branching molecules, such as dextran, have prepared binding surfaces to increase binding density. In contrast to rough plasmonic surfaces, Liu et al. [29] used a Ni seed layer on a silver-based SPR sensor to reduce surface roughness, resulting in a smaller FWHM. Furthermore, Byun et al. [28] investigated the localized surface plasmon resonance (LSPR) on a nanowire-based structure with varying roughness levels. They also concluded that the effect from localized surface plasmon resonance caused a change in the extinction peak amplitude.

**Table 1.1** Shows the RMS Roughness values for different surface treatment techniques.

Surface Treatment Techniques	RMS Roughness
Sputter Coating (No Treatment) [31]	1.4 nm–2.5 nm
Laser Ablation [34]	0.17 nm
Mica Substrate Utilizing [35]	0.2 nm
Helium Ion Beam [33]	0.267 nm
Chemical Polishing [37,38]	0.38 ± 0.05 nm
Chemically Grown Single-Crystalline Gold [35]	<1 nm
Thermal Annealing [32]	<1 nm

Various surface treatment methods have been utilized as a postprocessing procedure in metal film manufacturing to reduce surface roughness. The metal layer of the SPR-based sensor was traditionally manufactured using a sputter coating with a root-mean-square (RMS) roughness of 1.4 nm to 2.5 nm [30]. Surface treatments such as laser ablation [31], mica substrate utilizing [32], helium ion beam [33], and thermal annealing [34] may be employed to smooth the metal film further. Table 1.1 summarizes the surface roughness for the treatment techniques mentioned.

เอกสารนี้เป็นเอกสารที่สงวนไว้สำหรับการใช้งานเพื่อการศึกษาเท่านั้น ไม่อนุญาตให้นำไปใช้ประโยชน์ด้านการค้า  
ไม่ว่ากรณีใดๆ ทั้งสิ้น อีกทั้งห้ามมิให้ดัดแปลงเนื้อหา และต้องอ้างอิงถึงเจ้าของเอกสารทุกครั้งที่มีการนำไปใช้

## 1.2 Objectives

1. To theoretically investigate the effect of the surface roughness of a gold film on the performance of the protein binding application for an SPR-based sensor.
2. To analyze the change in the quantitative performance parameters, include plasmonic angle, binding sensitivity, full width at half maximum, intensity contrast, plasmonic intensity, and figure of merits due to roughness.
3. To separate and quantify the enhancement and deterioration effect of SPR detection as an LSPR effect and the binding surface area provided by rough surfaces.

## 1.3 Research Hypothesis

1. Due to the surface roughness, full width at half maximum, intensity contrast, and plasmonic angle degrade inevitably. However, the sensitivity can significantly enhance at a higher roughness level due to a wider protein binding area.
2. Roughness establishes a greater surface area and the LSPR effect. The change in SPR detection mainly relies on the LSPR effect, while the protein increment will only be available at the extreme roughness region.

## 1.4 Research Scope

This research provides a theoretical investigation for the protein binding application of SPR detection. The study mainly involves a simulation of the angular scanning technique on the Kretschmann configuration-based sensor with the noble metal layer employed as a gold film. Gold material was chosen for this study due to its chemical stability and biocompatibility in biochemical and bioscience-based applications. In addition, the sensing region is employed as a water-based environment and a 5nm-thick Bovine serum albumin (BSA) layer with refractive indices of 1.33 and 1.35, respectively. Apart from an angular scanning scheme, intensity detection and phase detection are also partially investigated at significant operating points.

## 1.5 Research Plan

Table 1.2 Shows the research plan for the theoretical investigation

Operation Plan	Research Progress / 2 Months											
	2	4	6	8	10	12	14	16	18	20	22	24
1. Research preparation and literature reviews	■											
2. Research plan and procedure authorization		■										
3. Theoretical investigation on convergence test			■									
4. Theoretical investigation of SPR performance				■								
5. Theoretical investigation of surface's electric fields					■							
6. Theoretical investigation of supplementary parts						■						
7. Manuscript preparation							■					
8. Publication process of the manuscript								■				

เอกสารนี้เป็นเอกสารที่สงวนไว้สำหรับการใช้งานเพื่อการศึกษาเท่านั้น ไม่อนุญาตให้นำไปใช้ประโยชน์ด้านการค้า  
ไม่ว่ากรณีใดๆ ทั้งสิ้น อีกทั้งห้ามมิให้ดัดแปลงเนื้อหา และต้องอ้างอิงถึงเจ้าของเอกสารทุกครั้งที่มีการนำไปใช้

## CHAPTER 2

### RELATED THEORIES

#### 2.1 Theories of Light

Human understands the world through five senses: smell, touch, hearing, taste, and vision. Light is an element which stimulates our sense of vision, or our eyes. Our eyes convert light particles, known as photons [35], to an electrical signal sent to the brain, which processes into images in our mind afterwards. The nature of light can be studied and explained based on various theories. This thesis provides four crucial theories, including corpuscular theory, wave theory, electromagnetic theory, and quantum theory [35].

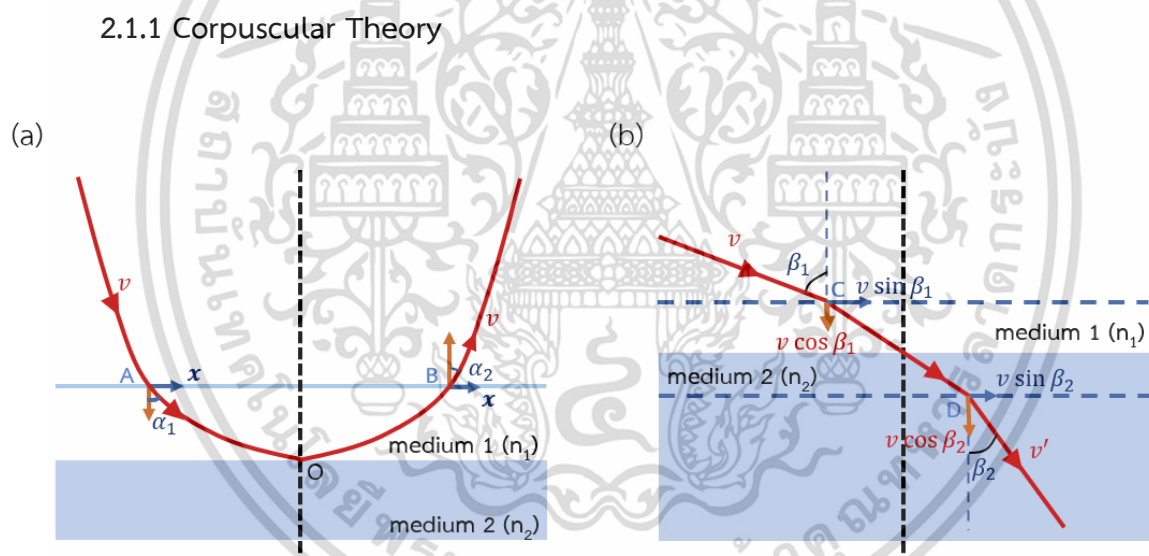


**Figure 2.1** Shows schematics of (a) the law of reflection and (b) the law of refraction for the corpuscular theory.

The ancient Greeks claimed the corpuscular theory [35,36] and were supported by Sir Isaac Newton. The theory indicates that light comprises tiny elastic particles, so-called corpuscles emitting in every direction. These corpuscles can travel through the interstice of matter's particles with the speed of light due to their tiny size. In addition, since the particles are emitted from the luminescence body at high speed, they are unaffected by external forces. Thus, according to Newton's second law of motion, the corpuscles move in a straight line.

เอกสารนี้เป็นเอกสารที่สงวนไว้สำหรับการใช้งานเพื่อการศึกษาเท่านั้น ไม่อนุญาตให้นำไปใช้ประโยชน์ด้านการค้า  
ไม่ว่ากรณีใดๆ ทั้งสิ้น อีกทั้งห้ามมิให้ดัดแปลงเนื้อหา และต้องอ้างอิงถึงเจ้าของเอกสารทุกครั้งที่มีการนำไปใช้

The corpuscular's reflection and refraction theories are slightly more complex than the standard theories. As the light approaches the reflection interface, the particles experience a repulsion force at a significantly small distance above it, indicated as a solid light-blue line in Figure 2.1a [35]. The light's velocity can be resolved in x and y components at point A at an angle  $\alpha_1$  concerning y-axis. The velocity in the y direction decreases at this near-field region until it reaches zero at point O. The light then increases its speed as it repulses back to point B, where its speed is equivalent to point A. Furthermore, the reflected angle, expressed as  $\alpha_2$ , is identical to the incident angle  $\alpha_1$ . Despite the various vertical velocity, the velocity in the x direction remains constant and can be calculated using Equation (2.1).

$$x = v \sin \alpha_1 = v \sin \alpha_2, \alpha_1 = \alpha_2 \quad (2.1)$$

Where  $x$  is the velocity in the x-direction.

$v$  is a resultant velocity.

Light in corpuscular theory also experiences a different effect in the refraction system. An attraction force from the interface gives rise to the incident beam's velocity in the y-direction [35]. Furthermore, its incident angle  $\beta_1$  at point C is slightly reduced before approaching the interface, as illustrated in Figure 2.1b. As it passes into the new medium, its velocity and reflected angle are altered as it reaches point D, which depends on the refractive index. This correlation can be explained via a mathematical equation, as expressed in Equations (2.2) and (2.3), which was later known as Snell's law of refraction [37,38].

$$v \sin \beta_1 = v' \sin \beta_2, \text{ or } \frac{\sin \beta_1}{\sin \beta_2} = \frac{v'}{v} \quad (2.2)$$

$$\frac{v'}{v} = \mu_2^1 \quad (2.3)$$

Where  $v$  and  $v'$  are the velocity in the first and second media.

$\mu_2^1$  is the refractive index of the incident medium with respect to the refracted medium's refractive index.

### 2.1.2 Wave Theory

While the corpuscular theory was accepted among scientists in the seventeenth century, Christian Huygens proposed light's wave theory [39]. Based on this theory, the luminous body is defined as a source of disturbance in a hypothetical medium, the ether [40]. This source generates disturbance propagating in every direction with an equally distributed energy. According to Huygens, the vibration from the luminous source behaves the same as in solid or liquid, which is in mechanical nature. Huygens also assumed this wave is longitudinal, where the particles vibrate in the same direction as the medium. The theory can effectively explain the reflection and refraction properties in crystals. However, the polarization property could not be described with the unsymmetrical characteristics of the longitudinal wave. Fresnel and Young overcame this issue, who stated that light is propagated in a transverse wave manner with ether particles vibrating perpendicularly to the medium [41,42].

### 2.1.3 Electromagnetic Theory

Maxwell successfully synthesized electricity and magnetism and proposed equations linking the significant nineteenth-century theories [43]. Moreover, he discovered that electromagnetic waves travel at the speed of light, which later concluded that light is an electromagnetic wave. Initially, ether was presumed to be a medium for propagating waves. Nevertheless, the ether must be rigid and pliable to make the light wave, which possesses high frequency, propagates, and allows free passage to heavenly bodies. Finally, in 1887, Michelson and Morey proved that no such medium exists [44].

### 2.1.4 Quantum Theory

Max Planck discovered that the absorption of radiation energy is not continuous through an experiment in black body radiation [45-47]. He explained that thermal radiation is emitted and absorbed by indivisible entities, the so-called quantum. In addition, each quantum particle possesses an energy,  $h\nu$ , where  $h$  is Planck's constant and  $\nu$  is a velocity. Einstein later employed quantum theory on photoelectric emission [48,49]. He also described that these entities travel separately in space with a speed  $c$  (approximately  $300 \times 10^6$  m/s) known as photons. In 1923, Compton experimented with a confirmation of quantum theory [50]. The experiment involved emitting monochromatic X-rays on the matter and observing the scattering effects. The Compton effect illustrates that the เอกสารนี้เป็นเอกสารที่สงวนไว้สำหรับการใช้งานเพื่อการศึกษาเท่านั้น ไม่อนุญาตให้นำไปใช้ประโยชน์ด้านการค้า  
ไม่ว่ากรณีใดๆ ทั้งสิ้น อีกทั้งห้ามมิให้ดัดแปลงเนื้อหา และต้องอ้างอิงถึงเจ้าของเอกสารทุกครั้งที่มีการนำไปใช้

scattered rays had slightly longer wavelengths than the original. Despite the benefits of understanding radiation interaction, the theory cannot account for some properties of light, including polarization, interference, and diffraction. Therefore, radiation is considered as both particles and waves.

## 2.2 Properties of Light

This section provides significant properties of light which are involved in this investigation. These properties include electromagnetic waves, reflection, refraction, dispersion, and polarization.

### 2.2.1 Electromagnetic Properties

Electromagnetic waves are non-mechanical and transverse waves which propagate at the speed of light in a vacuum [51,52]. These are the properties of electromagnetic waves which light also possesses:

- (1) Electromagnetic waves are generated from the acceleration of any charge.
- (2) The propagation of electromagnetic waves does not require a medium; therefore, it is not a mechanical wave.
- (3) Naturally, electromagnetic waves are transverse waves which consist of an electric field, magnetic field, and propagation vectors perpendicular to each other, as illustrated in Figure 2.2. The vectors' direction can be identified using the "right-hand rule" [52].
- (4) Electromagnetic waves propagate at the speed of light in a vacuum based on the equation,  $c = 1/\sqrt{\epsilon_0\mu_0}$ , where  $\epsilon_0$  and  $\mu_0$  are free space's permittivity and permeability, respectively.
- (5) The speed of electromagnetic wave propagation in a medium with permittivity,  $\epsilon$ , and permeability,  $\mu$ , is always less than its speed in free space or vacuum. The refractive index of the medium can be defined as expressed in Equation (2.4).
- (6) An electric or magnetic field cannot deflect electromagnetic waves.
- (7) Electromagnetic waves possess interference, polarization, and diffraction behaviour.
- (8) Electromagnetic waves are composed of energies, linear momentum and angular momentum, similar to other locks.

$$n = \frac{c}{v} = \frac{1}{\sqrt{\epsilon_0 \mu_0}} / \frac{1}{\sqrt{\epsilon \mu}}, \therefore n = \sqrt{\epsilon \mu_r} \quad (2.4)$$

Where  $\epsilon$  is a relative permittivity of the medium known as the dielectric constant.

$\mu_r$  is a relative permeability of the medium.

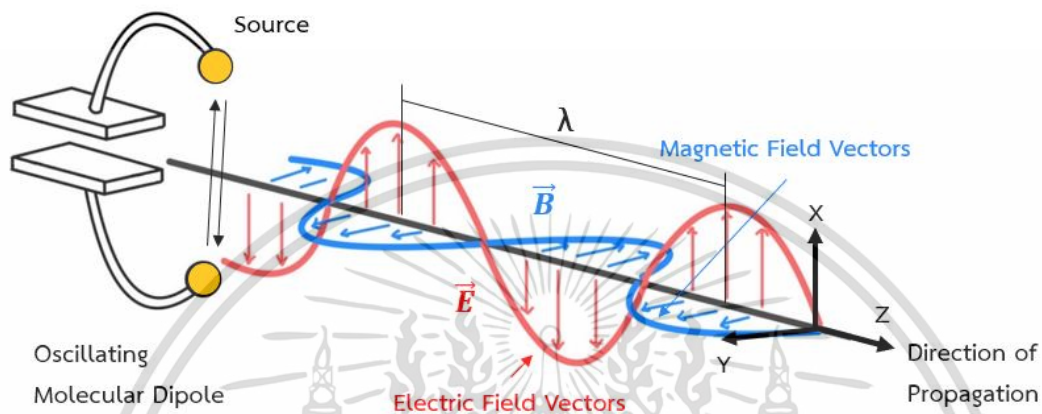


Figure 2.2 Shows the structure of an electromagnetic wave generated from the oscillation of a molecular dipole.

In addition to property (1), any charge produces an electric field when stationary. However, if the charge moves with a uniform velocity, it generates a substantial current and emits a magnetic field consequently. The amplitude of the electric and magnetic fields can be calculated based on Equations (2.5) and (2.6), respectively. Moreover, the produced fields from an oscillation of the charges define the speed of light as expressed in Equation (2.7) [51].

$$E_x = E_0 \sin(kz - \omega t) \quad (2.5)$$

$$H_y = H_0 \sin(kz - \omega t) \quad (2.6)$$

$$c = E_0 / H_0 \quad (2.7)$$

Where  $E_x$  and  $H_y$  are the vectors of electric and magnetic fields in the propagating wave.

$E_0$  and  $H_0$  are the vectors of electric and magnetic fields produced by the oscillated charge.

$k$  is the wave vector.

เอกสารนี้เป็นเอกสารที่สงวนไว้สำหรับการใช้งานเพื่อการศึกษาเท่านั้น ไม่อนุญาตให้นำไปใช้ประโยชน์ด้านการค้า  
ไม่ว่ากรณีใดๆ ทั้งสิ้น อีกทั้งห้ามมิให้ดัดแปลงเนื้อหา และต้องอ้างอิงถึงเจ้าของเอกสารทุกครั้งที่มีการนำไปใช้

$z$  is the propagating distance.

$\omega$  is the angular frequency of the wave vector.

## 2.2.2 Reflection and Refraction of Light

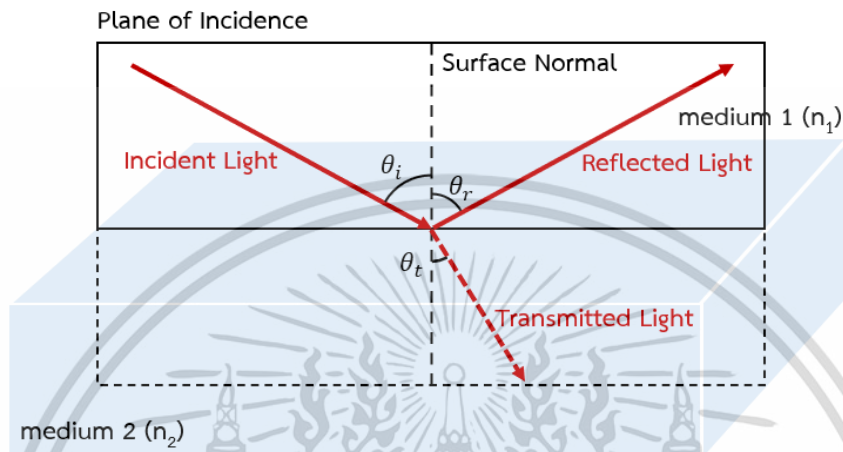


Figure 2.3 Shows a schematic of an incident light approaching an interface between media, resulting in a reflected and a transmitted (refracted) light.

Some light reflects its incident medium when light travels from one medium to another. This phenomenon is known as the reflection of light [53]. Light can undergo two types of reflection: Regular and diffuse reflection [54]. Regular reflection occurs when light bounces against a uniform interface. On the other hand, if light reflects from a rough surface, its direction is random, and the phenomenon is so-called diffuse reflection. Figure 2.3 indicates the schematic of a light reflection. When the light approaches at an incident angle,  $\theta_i$ , and intersects with the planar, known as the point of incidence; it reflects to the same medium and same plane of incidence with an equivalent angle,  $\theta_r$ , measuring toward the surface normal. Despite the light reflection, some light penetrates another medium with the transmitted angle,  $\theta_t$ . This light behaviour was described as Snell's Law described earlier [38]

### 2.2.3 Dispersion of Light

Wavelength also has an impact on the refractive index. Naturally, there is a decrease in the refractive index in response to an increase in wavelength. Therefore, the light is separated according to its wavelength as it propagates through a medium [55]. This

เอกสารนี้เป็นเอกสารที่สงวนไว้สำหรับการใช้งานเพื่อการศึกษาเท่านั้น ไม่อนุญาตให้นำไปใช้ประโยชน์ด้านการค้า  
ไม่ว่ากรณีใดๆ ทั้งสิ้น อีกทั้งห้ามมิให้ดัดแปลงเนื้อหา และต้องอ้างอิงถึงเจ้าของเอกสารทุกครั้งที่มีการนำไปใช้

phenomenon is known as chromatic dispersion. When white light enters a glass prism, it splits into numerous colours, so-called a spectrum, as illustrated in Figure 2.4.

Furthermore, a glass prism, in this case, a medium which gives rise to this effect, is known as a dispersive medium. When numerous beams of different wavelengths pass through a prism, each beam's refractive indices vary. Thus, the refracted angles are different, with a violet beam suffering the most from this effect, while the red colour is slightly affected [55].

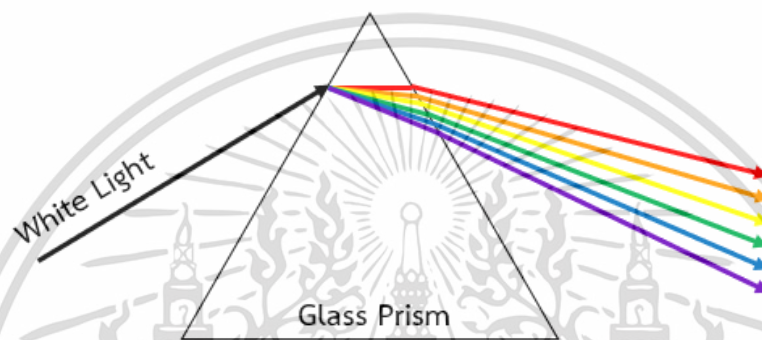


Figure 2.4 Shows a schematic of white light entering a glass prism and diffracting into different color beams.

#### 2.2.4 Polarization of Light

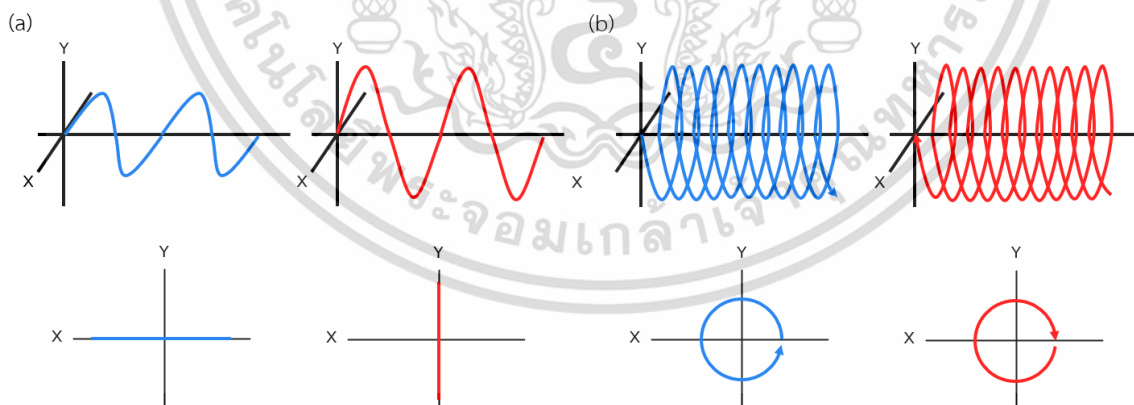


Figure 2.5 Shows schematics of (a) linearly polarized and (b) circularly polarized electromagnetic waves.

As mentioned earlier, light is an electromagnetic field, and the term and theory of polarization define the direction of the electric field vector oscillations. Figures 2.5a and 2.5b indicate two significant types of polarization of light: Linear and circular polarization

เอกสารนี้เป็นเอกสารที่สงวนไว้สำหรับการใช้งานเพื่อการศึกษาเท่านั้น ไม่นิยมนำไปใช้ประโยชน์ด้านการค้า  
ไม่ว่ากรณีใดๆ ทั้งสิ้น อีกทั้งห้ามมิให้ดัดแปลงเนื้อหา และต้องอ้างอิงถึงเจ้าของเอกสารทุกครั้งที่มีการนำไปใช้

[56, 57]. Linear polarization defines an electromagnetic wave with the electric field oscillating on the same plane. On the other hand, if the electromagnetic wave propagates in a spiral direction, the direction of the electric fields' oscillation varies along the propagating wave, so-called circular polarization. The trajectories observed from the directions in which the waves propagate are illustrated as the bottom images.

This research and many optical instruments mainly involve linear polarization, relying on the light that reflects or transmits at an interface. As light approaches a surface, linear polarization can be further classified into two sub-types: TE-polarization (transverse electric field) or s-polarization and TM-polarization (transverse magnetic field) or p-polarization, as shown in Figures 2.6a and 2.7b, respectively [58]. In the TE-polarization case, the electric field is perpendicular to the interface. On the other hand, the perpendicular vector of the TM-polarized light is the magnetic field. Generally, light comprises electric fields in every direction, so-called non-polarized light. Nevertheless, the polarization characteristic can be provided by allowing the non-polarized light to enter the polariser optical device [59].

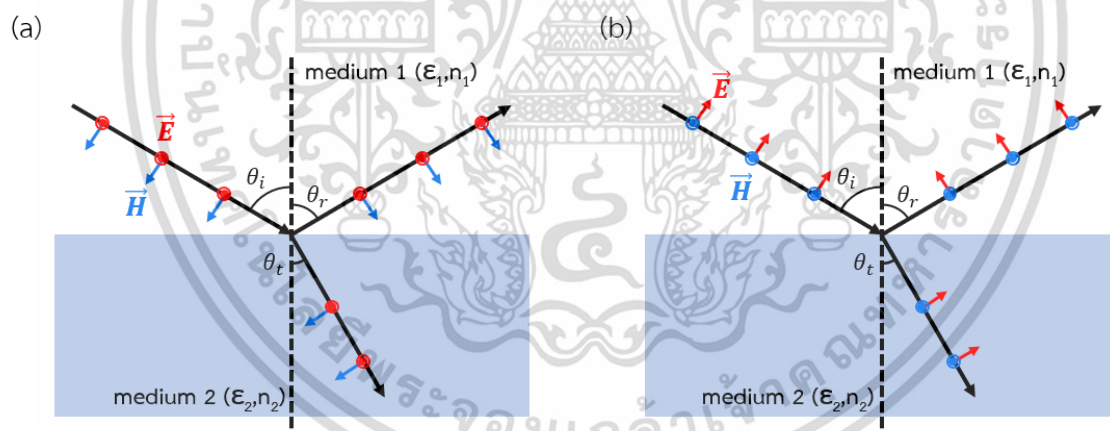


Figure 2.6 Shows schematics of (a) TE-polarized light and (b) TM-polarized light as it enters a different medium.

### 2.3 Total Internal Reflection

As mentioned in the previous sections, light possesses a reflectivity property that relies on the reflected surface's nature. If the surface is theoretically uniform, the light will obey a simple law of reflection, stating that the reflected angle is identical to the incident angle [35, 53]. External reflection occurs when light approaches from a lower refractive index region to a higher refractive index region [60]. In addition, this optical property

เอกสารนี้เป็นเอกสารที่สงวนลิขสิทธิ์ไว้เพื่อการเรียนการสอน เมื่อผู้ใดเห็นไปใช้ประโยชน์ในการค้า  
ไม่ว่ากรณีใดๆ ทั้งสิ้น อีกทั้งห้ามมิให้ตัดแปลงเนื้อหา และต้องอ้างอิงถึงเจ้าของเอกสารทุกครั้งที่มีการนำไปใช้

depends on an incident angle and type of polarization. On the other hand, when light propagates from a higher refractive index medium to a lower refractive index medium, it reflects an equal amount of optical energy at the interface, acting similarly to a mirror if the incident angle is greater than the critical angle. Total internal reflection (TIR) was the name given to this optical effect [61]. Mirage, for instance, is an optical phenomenon in which light reflects at an interface between heated air on a hot surface, which has a lower refractive index than ambient air, resulting in a water or mirror-like image from a distance (high incident angle) [61]. Figure 2.7 illustrates a reflectivity of an external reflection and a total internal reflection case for both TM ( $\perp$ ) and TE ( $\parallel$ ) polarization, and an incident angle ranges from zero to  $90^\circ$ .

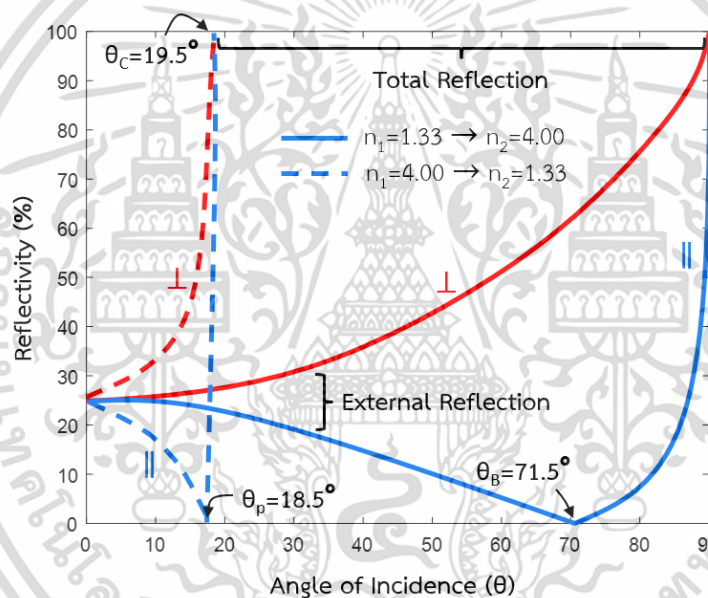


**Figure 2.7** Shows the reflectivity of TM (red line) and TE-polarized light (blue line) as it approaches an interface between media at different incident angles. Note that  $\theta_c$ ,  $\theta_p$ ,  $\theta_B$  indicate a critical angle, a principal angle, and Brewster's angle, respectively.

## 2.4 Evanescent Wave

Despite the reflected optical energy from TIR, there is a loss in the electromagnetic fields as the light shifts from one to another medium with different refractive indices. This alternation in electromagnetic properties generates a travelling wave, known as an evanescent wave, on the surface of the transmitted region [62]. The wave propagates slightly into the lower refractive index area, resulting in a change in the characteristics of the wave vector,  $\mathbf{k}$ . The wave vector in the x-direction,  $\mathbf{k}_x$ , which is parallel to the surface

เอกสารนี้เป็นเอกสารที่สงวนไว้สำหรับการใช้งานเพื่อการศึกษาเท่านั้น ไม่อนุญาตให้นำไปใช้ประโยชน์ด้านการค้า  
ไม่ว่ากรณีใดๆ ทั้งสิ้น อีกทั้งห้ามมิให้ดัดแปลงเนื้อหา และต้องอ้างอิงถึงเจ้าของเอกสารทุกครั้งที่มีการนำไปใช้

and remains the same as it penetrates a different medium. Based on Equation (2.2) of Snell's Law, Equation (2.7) is derived and  $k_y$  which alternatively is perpendicular to the plane of incidence, can be calculated as expressed in Equation (2.8).

$$k = \sqrt{k_x^2 + k_y^2 + k_z^2} = n \frac{2\pi}{\lambda} = n \frac{\omega}{c} \quad (2.7)$$

$$k_{y_2}^2 = n_1^2 \left(\frac{2\pi}{\lambda}\right)^2 \left(\frac{n_2^2}{n_1^2} - \sin^2\theta\right) \quad (2.8)$$

As mentioned earlier, the evanescent effect occurs in the TIR, where the incident angle is greater than the critical angle and  $n_1$  is more than  $n_2$ . In consequence, according to Equation (2.8),  $k_y$  will be purely imaginary. In this regard, we can conclude that the only travelling wave in the transmitted region is in the x-direction. The electric field here, given as  $E_2$ , can be calculated as expressed in Equation (2.9) and decays as it travels along the surface. This field is also denoted as the evanescent field [62].

$$E_2 = E_0 e^{-\kappa_{y_2} y} \exp(j\omega t - jk_x x) \quad (2.9)$$

Where  $E_0$  is the electric field's amplitude.

$\kappa_{y_2}$  is a variable for calculating a characteristic distance for the electric field decaying along the y-direction. The characteristic distance is known as a penetration depth, which can be calculated as  $1/\kappa_{y_2}$  and is also equivalent to  $1/jk_{y_2}$ .

Moreover, the evanescent intensity,  $I(z)$  can decline as the penetration depth increases or the incident angle becomes wider; this relationship was expressed in Equation (2.10).

$$I(z) = I_0 e^{-z/d} \quad (2.10)$$

Where  $I_0$  is the intensity at  $z$  equal to zero, which also relies on the intensity and polarization of the approaching electric field, as expressed in Equations (2.11) and (2.12).

$z$  is the perpendicular distance from the interface between media.

$d$  is the penetration depth, which is unaffected by the polarization of the incident light and decreases as the incident angle increases. Equation (2.13) shows the calculation for  $d$ .

เอกสารนี้เป็นเอกสารที่สงวนไว้สำหรับการใช้งานเพื่อการศึกษาเท่านั้น ไม่อนุญาตให้นำไปใช้ประโยชน์ด้านการค้า  
ไม่ว่ากรณีใดๆ ทั้งสิ้น อีกทั้งห้ามมิให้ดัดแปลงเนื้อหา และต้องอ้างอิงถึงเจ้าของเอกสารทุกครั้งที่มีการนำไปใช้

$$I_0^{\parallel} = \epsilon^{\parallel} \cdot \frac{4\cos^2\theta(2\sin^2\theta - n^2)}{n^4\cos^2\theta + \sin^2\theta - n^2} \quad (2.11)$$

$$I_0^{\perp} = \epsilon^{\perp} \cdot \frac{4\cos^2\theta}{1 - n^2} \quad (2.12)$$

$$d = \frac{\lambda_0}{4\pi} \sqrt{n_1^2 \sin^2\theta - n_2^2} \quad (2.13)$$

Where  $I_0^{\parallel, \perp}$  are the evanescent intensity parallel and perpendicular to the plane of incidence, respectively.

$\epsilon^{\parallel, \perp}$  are the incident electric field intensity with polarizations parallel and perpendicular to the incident plane.

$n$  is a ratio of the incident region's refractive index and the transmitted region's refractive index, which can be calculated as  $n = n_2/n_1$ .

$\theta$  is an angle of incidence.

Calculating using Equation (2.11) and (2.12), both parallel and perpendicular evanescent intensity can be stronger than the incident intensity with an incident angle as a critical angle and exponentially decrease as it approaches 90°, as illustrated in Figure 2.8 [62]. In addition, the  $I_0^{\perp}$  is always lower than  $I_0^{\parallel}$  at this range.

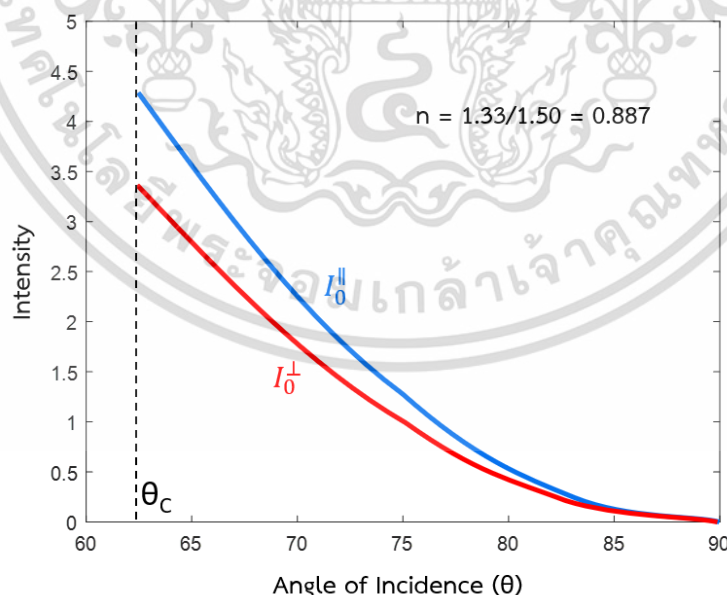


**Figure 2.8** Shows the parallel and perpendicular evanescent intensity at multiple incident angles at  $n$  of 0.887 which corresponds to  $\theta_c$  of 62.46°.

เอกสารนี้เป็นเอกสารที่สงวนไว้สำหรับการใช้งานเพื่อการศึกษาเท่านั้น ไม่อนุญาตให้นำไปใช้ประโยชน์ด้านการค้า  
ไม่ว่ากรณีใดๆ ทั้งสิ้น อีกทั้งห้ามมิให้ดัดแปลงเนื้อหา และต้องอ้างอิงถึงเจ้าของเอกสารทุกครั้งที่มีการนำไปใช้

The electric field and magnetic field components in consequence of the TIR can be computed using Equation (2.14) to (2.19), where the plane of incidence is in an x-z plane [62]. Generally, the evanescent intensity which affected fluorescence excitation is represented in the term  $|\mathbf{E}|^2$ . In addition, the electromagnetic field's energy flux can be expressed as a real part of the Poynting vector,  $\mathbf{S} = (c/4\pi)\mathbf{E} \times \mathbf{H}$ , where  $\mathbf{H}$  is the magnetic field. Note that  $|\mathbf{S}|$  is proportional to  $|\mathbf{E}|^2$  for the transverse field case only, not for the evanescent field domain [62].

$$E_x = \left[ \frac{2 \cos \theta (\sin^2 \theta - n^2)^{1/2}}{(n^4 \cos^2 \theta + \sin^2 \theta - n^2)^{1/2}} \right] A_{\parallel} e^{-i(\delta_{\parallel} + \pi/2)} \quad (2.14)$$

$$E_y = \left[ \frac{2 \cos \theta}{(1 - n^2)^{1/2}} \right] A_{\perp} e^{-i\delta_{\perp}} \quad (2.15)$$

$$E_z = \left[ \frac{2 \cos \theta \sin \theta}{(n^4 \cos^2 \theta + \sin^2 \theta - n^2)^{1/2}} \right] A_{\parallel} e^{-i\delta_{\parallel}} \quad (2.16)$$

$$H_x = \left[ \frac{2 \cos \theta (\sin^2 \theta - n^2)^{1/2}}{(1 - n^2)^{1/2}} \right] A_{\perp} e^{-i(\delta_{\perp} - \pi)} \quad (2.17)$$

$$H_y = \left[ \frac{2n^2 \cos \theta}{(n^4 \cos^2 \theta + \sin^2 \theta - n^2)^{1/2}} \right] A_{\parallel} e^{-i(\delta_{\parallel} - \pi/2)} \quad (2.18)$$

$$H_z = \left[ \frac{2 \cos \theta \sin \theta}{(1 - n^2)^{1/2}} \right] A_{\perp} e^{-i\delta_{\perp}} \quad (2.19)$$

Where  $A_{\parallel, \perp}$  are the electric field's amplitudes in parallel and perpendicular directions, respectively.

$\delta_{\parallel, \perp}$  are the phase factors relative to the incident  $\mathbf{E}$  and  $\mathbf{H}$ 's phases at the z-axis equal to zero and can be calculated using equations;  $\delta_{\parallel} \equiv \tan^{-1} \left[ \frac{(\sin^2 \theta - n^2)^{1/2}}{n^2 \cos^2 \theta} \right]$  and  $\delta_{\perp} \equiv \tan^{-1} \left[ \frac{(\sin^2 \theta - n^2)^{1/2}}{\cos^2 \theta} \right]$ , respectively.

The appearance of the phase factors,  $\delta_{\parallel, \perp}$ , lead to a finite longitudinal shift of the incident light, known as the Goos-Hanchen shift [63-65], as indicated in Figure 2.9a. In this regard, a portion of the energy is penetrated to the lower refractive index medium and skimming along the Goos-Hanchen distance, ranging from a fraction of wavelength to infinite when  $\theta$  is equal to  $90^\circ$  and  $\theta_c$ , respectively. The penetrated energy is then reflected in the incident region. In most total internal reflection fluorescence (TIRF) experiments [66-69], incident light with a finite intensity passes through a converging lens, enters a prism, and focuses on the incident plane between the higher refractive index and lower refractive index media. This uniform beam geometry generates an evanescent illumination with an

เอกสารนี้เป็นเอกสารที่สงวนลิขสิทธิ์เพื่อการเรียนเพื่อการศึกษาเท่านั้น เมื่ออนุญาตให้เผยแพร่ไปยังระบบวิชาการ

ไม่ว่ากรณีใดๆ ทั้งสิ้น อีกทั้งห้ามมิให้ดัดแปลงเนื้อหา และต้องอ้างอิงถึงเจ้าของเอกสารทุกครั้งที่มีการนำไปใช้

elliptical Gaussian profile. Moreover, the polarization and the penetration depth are approximately identical to the planar wave [63].

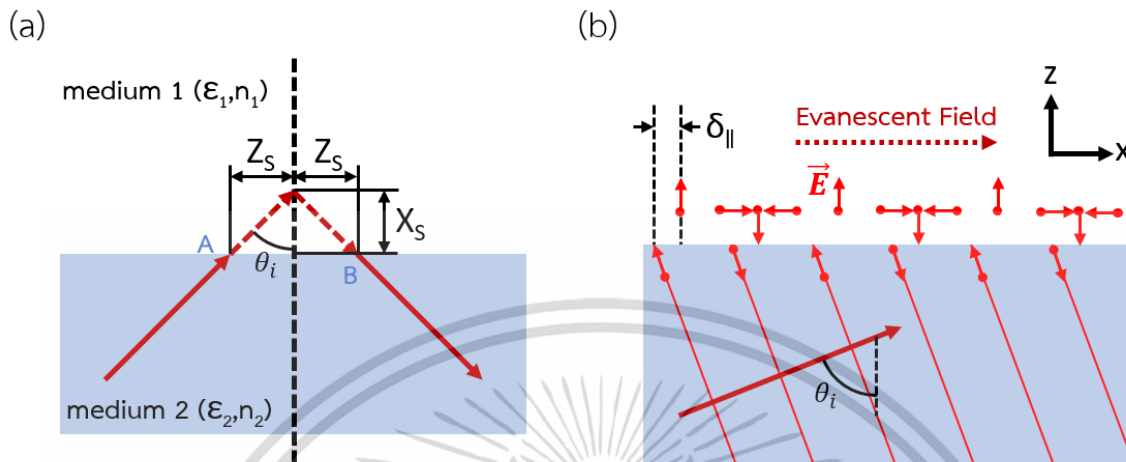


**Figure 2.9** Shows the schematics of (a) a Goos-Hanchen shift at the total reflection between two media and (b) electric field vectors of an incident and evanescent light with the  $\parallel$  polarization. Note that the vectors refer to the  $z=0$  position, and  $\delta_{\parallel}$  indicates the phase lag.

In the theoretical investigation of TIRF, the light absorbance, the light scattering, the unmatched layers of refractive indices, and the electrical conductivity are generally omitted. It is undeniable that these factors have a substantial impact on the produced evanescent wave. The material's absorbance property disturbs the evanescent wave and consequently affects the linearity between the surface concentration's actual absorbance and the observed fluorescence. The magnitude of this non-linear effect was investigated by Burghardt and Axelrod [62]. They proposed a function of the surface concentration and the arbitrary thickness.

Nevertheless, the linearity between the surface concentration and the emitted fluorescence is still acceptable. Similarly, Harrick [70,71] studied the quantitative correlation between the absorbance effect and the reflected beam's intensity. In addition, intermediate layers with a homogeneous dielectric material significantly impact the evanescent wave's intensity and propagating distance [61]. Furthermore, an additional TIR between an intermediate layer and the lower refractive index area can occur.

On the other hand, a completely different phenomenon can be observed if the metallic conductor is deposited on the surface. In this regard, the evanescent wave-excited

เอกสารนี้เป็นเอกสารที่สงวนไว้สำหรับการใช้งานเพื่อการศึกษาเท่านั้น ไม่อนุญาตให้นำไปใช้ประโยชน์ด้านการค้า  
ไม่ว่ากรณีใดๆ ทั้งสิ้น อีกทั้งห้ามมิให้ดัดแปลงเนื้อหา และต้องอ้างอิงถึงเจ้าของเอกสารทุกครั้งที่มีการนำไปใช้

molecules and their energy are transferred to the intermediate metallic layer instead of emitting fluorescence. Furthermore, if the metallic layer is adequately thin, the result can be observed as a hollow cone at a particular angle among the reflected light. This effect was utilized as a hyper-sensitive sensor, known as the surface plasmon resonance-based sensor [72], which will be explained in the next sections.

## 2.5 Surface Plasmon Resonance Theory

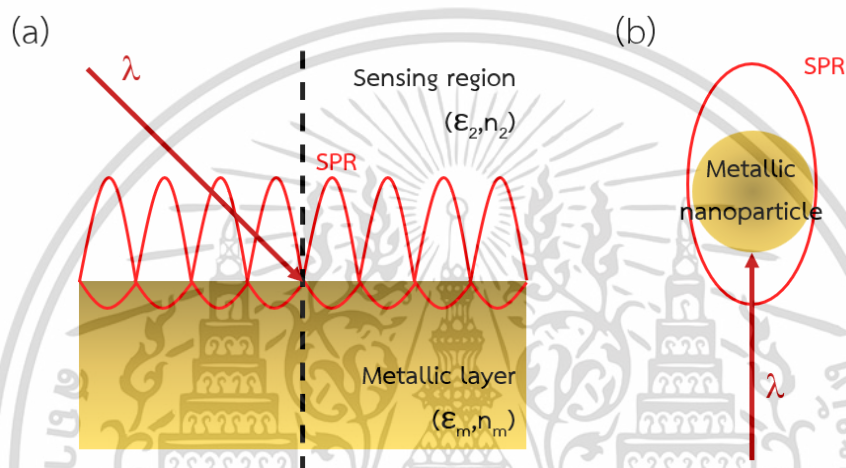


**Figure 2.10** Shows schematics of (a) surface plasmon polariton along the metallic layer and (b) localized surface plasmon resonance around the metallic nanoparticle.

The surface plasmons are electromagnetic waves generated from the free-electrons conduction of a noble metal, such as gold and silver. This metallic layer generally possesses a negative dielectric constant, giving high material reflectivity. In addition, the produced free-electron gas can sustain the oscillation of surface and volume charge-density, known as plasmons, at optical frequencies. This phenomenon significantly enhances the optical near fields if it occurs between a metal and a dielectric [73]. Furthermore, when the external electromagnetic wave with a matching momentum approaches the system, surface plasmons' resonating effect is generated, also known as surface plasmon resonance (SPR) [1,2]. The SPR can be found under two main circumstances: Localized surface plasmon resonance (LSPR) [74] and surface plasmon polariton (SPP) [75]. The LSPR is produced around the surface of a metallic nanoparticle which has a diameter ranging between 10 nm to 100 nm, as illustrated in Figure 2.10a. On the other hand, the SPP can be produced along the surface of a metallic layer with a

เอกสารนี้เป็นเอกสารที่สงวนไว้สำหรับการใช้งานเพื่อการศึกษาเท่านั้น ไม่อนุญาตให้นำไปใช้ประโยชน์ด้านการค้า  
ไม่ว่ากรณีใดๆ ทั้งสิ้น อีกทั้งห้ามมิให้ดัดแปลงเนื้อหา และต้องอ้างอิงถึงเจ้าของเอกสารทุกครั้งที่มีการนำไปใช้

thickness between 20 nm and 60 nm when it is excited by an external beam, as indicated in Figure 2.10b.

One approach for the dispersion relation analysis is utilizing the relationship between the angular frequency ( $\omega$ ) and the wave vector ( $\mathbf{k}$ ). In the p-polarized beam case, the complex reflection coefficient,  $r_p$ , can be computed using Fresnel's equations [76], as expressed in Equation (2.20). Moreover, the reflectance ( $R_p$ ) is defined as a ratio of the reflected intensities and can be calculated as  $|r_p|^2$ .

$$r_p = \frac{E_i}{E_r} = |r_p| e^{j\varphi} = \left| \frac{\tan(\theta - \theta_r)}{\tan(\theta + \theta_r)} \right| e^{j\varphi} \quad (2.20)$$

Where  $E_i$ ,  $E_r$  and  $E_t$  are the incident and reflected electric fields.

$\varphi$  is a phase change.

According to the equation, at the angle where  $\theta + \theta_r$  is  $90^\circ$ , the  $r_p$  is equal to zero. In this regard, there will be no light reflected. This position is known as the Brewster angle [77,78], where all the p-polarized light is absorbed and transmitted. On the other hand, if  $\theta - \theta_r$  is  $90^\circ$ , the nominator and the reflection coefficient become infinite, respectively. Nevertheless,  $E_r$  is not infinite for a small  $E_i$ . This phenomenon corresponds to resonance. Furthermore, we can deduce the dispersion relation at the resonance angle. Thus,  $\cos\theta = -\sin\theta_r$  and  $\tan\theta = k_{1x}/k_{1y} = -n_2/n_1$ . Here, the wave vectors can be rewritten as expressed in Equation (2.21) to Equation (2.23). These equations are crucial for analyzing the SPR dispersion relation for an interface between the two-half infinite media.

$$k_x^2 = k_1^2 - k_{y1}^2 = k_1^2 - k_x^2 \frac{\varepsilon_1}{\varepsilon_2} \quad (2.21)$$

$$k_x = \frac{\omega}{c} \sqrt{\frac{\varepsilon_1 \varepsilon_2}{\varepsilon_1 + \varepsilon_2}} \quad (2.22)$$

$$k_{yi} = \frac{\omega}{c} \sqrt{\frac{\varepsilon_i^2}{\varepsilon_1 + \varepsilon_2}} \quad (2.23)$$

Where  $\varepsilon_1$  and  $\varepsilon_2$  are dielectric constants of the incident and transmitted medium, respectively.

เอกสารนี้เป็นเอกสารที่สงวนไว้สำหรับการใช้งานเพื่อการศึกษาเท่านั้น ไม่อนุญาตให้นำไปใช้ประโยชน์ด้านการค้า  
ไม่ว่ากรณีใดๆ ทั้งสิ้น อีกทั้งห้ามมิให้ดัดแปลงเนื้อหา และต้องอ้างอิงถึงเจ้าของเอกสารทุกครั้งที่มีการนำไปใช้

$i$  is either one or two. Despite the constant  $k_x, k_y$  varies depending on its medium.

The results are further analysed when a metallic film is located between a glass prism and a low refractive index region, such as water. Equation (2.23) depicts a calculation for the dielectric constant of the employed metal film. The metallic layer contains many free electrons, which gives its angular frequency,  $\omega$ , less than the plasma frequency,  $\omega_p$ . Equation (2.25) indicates the calculation of  $\omega_p$ . In this regard, the electromagnetic field cannot propagate along the metal. Despite this absence, the electromagnetic field alternatively exists at the interface, with evanescent waves extending into both sides. Moreover, it has been investigated that  $k_{yi}$  is imaginary while  $k_x$  is a real number when  $\epsilon_2$  is greater than  $\epsilon_1$ . In the term of the sensor, the change in the sensing region results in the difference in a dielectric constant, wave vectors, and the resonance angle, respectively, as long that the shift occurs within the penetration depth, calculated using Equation (2.13).

$$\epsilon_m(\omega) = 1 - \frac{\omega_p^2}{\omega^2} \quad (2.24)$$

$$\omega_p = \sqrt{\frac{4\pi n_e e^2}{m_e}} \quad (2.25)$$

Where  $\epsilon_m$  is a dielectric constant of the metallic layer.

$n_e$  is the free electron density.

$e$  is the electron charge.

$m_e$  is the mass of electron.

### 2.5.1 Surface Plasmon Excitation

By substituting Equation (2.21) and (2.24) with Equation (2.25), a graphical plot of results can be acquired, as illustrated in Figure 2.11a. The blue solid and dashed curves indicate the surface plasmons dispersion for interfaces  $\epsilon_3/\epsilon_m$  and  $\epsilon_1/\epsilon_m$ , respectively. In a 2-media system case, the “normal” light, depicted as a solid red line, is not intersected with the surface plasmons curve. The result can be explained as this normal light does not have a matching wave vector and angular frequency that excite the surface plasmons.

This issue is solved by providing a thin metallic layer between both regions, as indicated in Figure 2.11b. Using Fresnel's equations [76], a more complicated version of Equation

เอกสารนี้เป็นเอกสารที่สงวนไว้สำหรับการใช้งานเพื่อการศึกษาเท่านั้น ไม่อนุญาตให้นำไปใช้ประโยชน์ด้านการค้า

ไม่ว่ากรณีใดๆ ทั้งสิ้น อีกทั้งห้ามมิให้ดัดแปลงเนื้อหา และต้องอ้างอิงถึงเจ้าของเอกสารทุกครั้งที่มีการนำไปใช้

(2.21) is carried out and two dispersion equations for  $k_x$  are established. In this regard, the incoming wave vector of the normal incident light can be tunable by adjusting the angle of incidence. The adjusted light, indicated as a dashed red line, is now intersected with the surface plasmons dispersion curves, and any line between the line “a” and “b” can excite the surface plasmons. This technique is known as attenuated total reflection (ATR) demonstrated by Kretschmann and Raether [79,80]. Moreover, Otto [81] developed a similar configuration, with a sensing region being a gap between the noble metallic layer and a glass prism. However, Otto’s model was less versatile than Kretschmann’s configuration; thus, Kretschmann’s design is more prevalent in the recent SPR experiments.

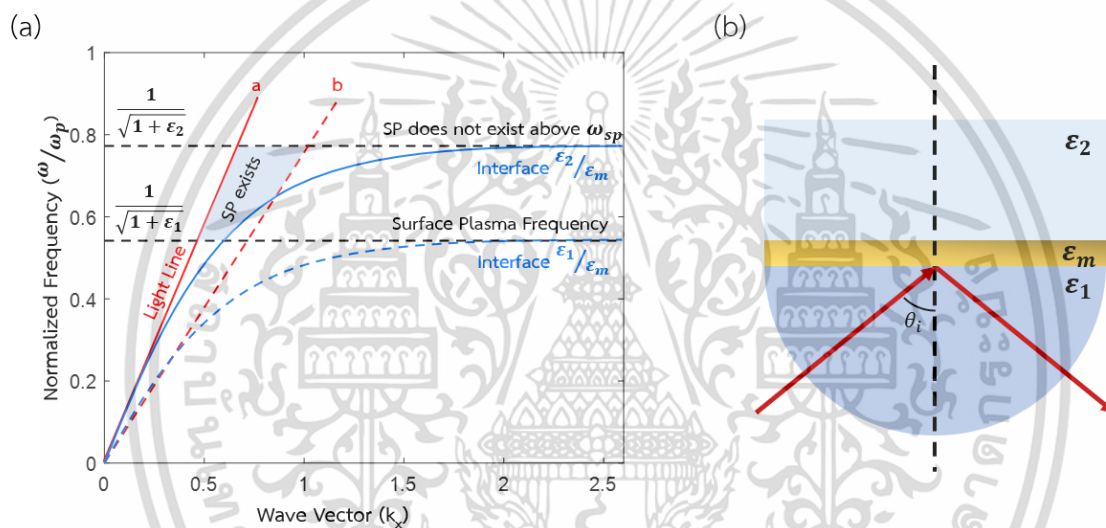


**Figure 2.11** Shows (a) a graphical illustration of a dispersion relation for surface plasmons where lines “a” and “b” indicate a dispersion relation for normal light in regions with  $\epsilon_2$  and  $\epsilon_1$ , respectively, and corresponds to an incident angle  $\theta_i$ ; and (b) an experimental setup which yields dispersion relation curves shown previously.

Nevertheless, various factors can affect the SPR conditions in the presented graph. For example, each medium's dielectric constant can affect the surface plasmons' frequency area. Moreover, the refractive indices of some media can be significantly altered due to the temperature change. The incident beam's wavelength also influences the normal light line, as indicated in Figure 2.11a, and the surface plasmons condition. Therefore, to preserve the instrument's linearity between refractive index change and plasmonic dip position, all other parameters must be controlled with the only alternation

เอกสารนี้เป็นเอกสารที่สงวนไว้สำหรับการใช้งานเพื่อการศึกษาเท่านั้น ไม่อนุญาตให้นำไปใช้ประโยชน์ด้านการค้า  
ไม่ว่ากรณีใดๆ ทั้งสิ้น อีกทั้งห้ามมิให้ดัดแปลงเนื้อหา และต้องอ้างอิงถึงเจ้าของเอกสารทุกครั้งที่มีการนำไปใช้

in the incident angle, which affected  $k_x$ . Equation (2.26) expresses the calculation of the change in the plasmonic angle,  $\Delta \sin \theta_{sp}$ .

$$\Delta \sin \theta_{sp} = \sqrt{\frac{\Delta \epsilon_2}{\epsilon_1 + \epsilon_2 + \epsilon_m}} \sim \Delta n_2 \quad (2.26)$$

The light's polarization also crucially affects the SPR. As mentioned earlier, surface plasmons are the conductivity from an oscillation of the surface charge density of free electrons. Furthermore, only the electromagnetic wave with an electric field perpendicular to the surface can induce this surface charge density. Due to this reason, only the p-polarized beam can excite SPR, while the s-polarized beam generates the TIR without the plasmons excitation.

## 2.6 Surface Plasmon Resonance Experiment

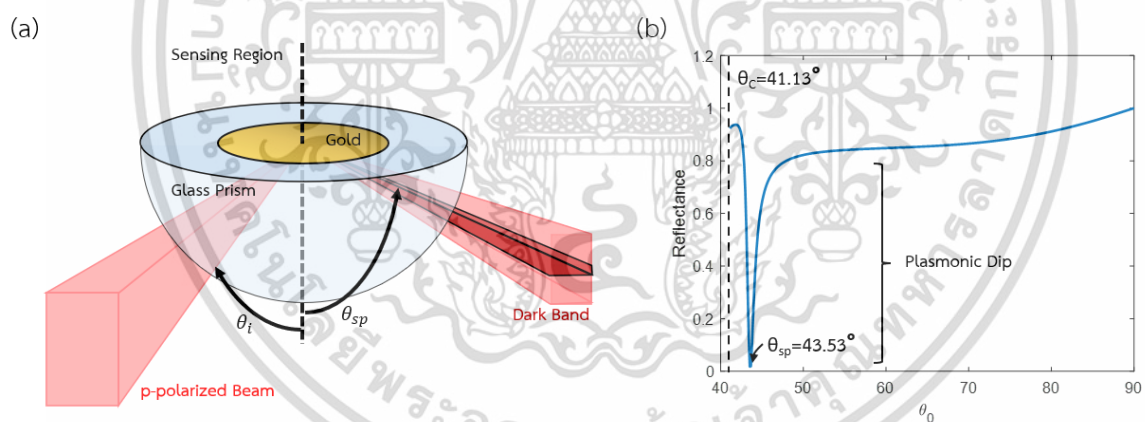


**Figure 2.12** Shows (a) the Kretschmann configuration for an SPR-based sensor and (b) the SPR response with a sensing region as air (refractive index of 1.00).

A simple experimental setup for the SPR is illustrated in Figure 2.12a, also known as the Kretschmann configuration [17]. The system comprises a noble metallic film, a glass prism, and an incident p-polarized beam. It reflects when a p-polarized light approaches through a glass prism to the metal layer. If multiple angles of incidence are employed, the monitored reflected light intensity would be significantly low (practically zero) at the

เอกสารนี้เป็นเอกสารที่สงวนไว้สำหรับการใช้งานเพื่อการศึกษาเท่านั้น ไม่อนุญาตให้นำไปใช้ประโยชน์ด้านการค้า  
ไม่ว่ากรณีใดๆ ทั้งสิ้น อีกทั้งห้ามมิให้ดัดแปลงเนื้อหา และต้องอ้างอิงถึงเจ้าของเอกสารทุกครั้งที่มีการนำไปใช้

specific angle, known as the plasmonic angle ( $\theta_{sp}$ ) or resonance angle. This phenomenon is due to the excitation of surface plasmons and SPR at that incident angle, resulting in a “dip” in the reflected light intensity, as shown in Figure 2.12b. In addition, the SPR-dip angle depends on various factors in the system, including the incident wavelength, refractive indices of the media (a glass prism and a sensing region), and the type of the utilized metal film.

### 2.6.1 Protein Binding Application in SPR Detection

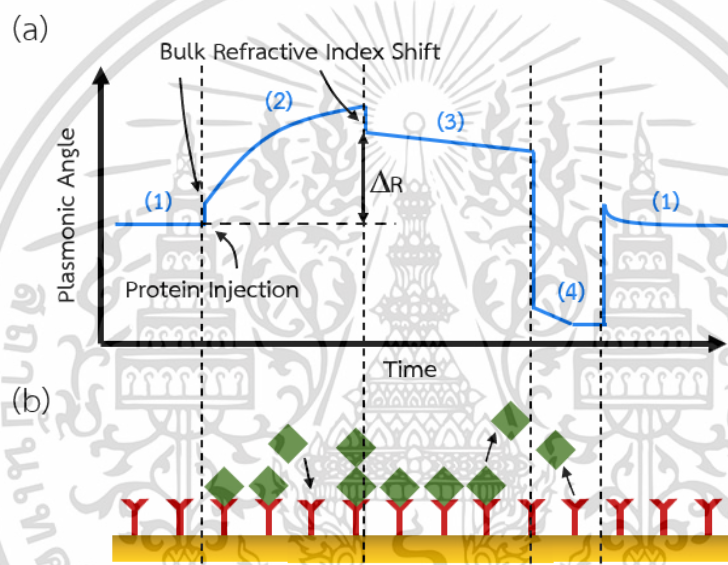


**Figure 2.13** Shows (a) the change in plasmonic angle during the baseline (1), association (2), disassociation (3), and regeneration (4) of a kinetic binding experiment, and (b) a schematic of protein binding during each phase.

SPR detection is an effective technique for monitoring a change in the refractive index near the metallic film [8-10]. Figure 2.13a illustrates the shift of a plasmonic angle when there is protein association or disassociation, also known as a sensorgram [82]. In this regard, biomolecular interaction can be investigated in real-time. Nevertheless, only the change within the penetration depth of an evanescent wave of approximately a few hundred nanometer can be detected. Furthermore, in this simple SPR system, there is a lack of intrinsic selectivity. In other words, any alternation in the refractive index will change the detected signal. To establish an SPR-based sensor with a selective property,

เอกสารนี้เป็นเอกสารที่สงวนลิขสิทธิ์หรือการเชิงงานเพื่อการศึกษาเท่านั้น เมื่ออนุญาตให้เผยแพร่ไปยังเว็บไซต์ด้านการค้า

ไม่ว่ากรณีใดๆ ทั้งสิ้น อีกทั้งห้ามมิให้ดัดแปลงเนื้อหา และต้องอ้างอิงถึงเจ้าของเอกสารทุกครั้งที่มีการนำไปใช้

modifying the metallic film with the ligand that captures the targeted molecules is necessary. This characteristic of SPR detection led to sensing applications concerning both a label-free sensor and a selective sensor.

In present times, various modified ligand-based sensors are commercially available, and numerous ligands can be customized. Moreover, the SPR detection technique is often employed to study biomolecular interactions between proteins and immunoassay applications [83-85]. Before conducting the SPR test, the sensor surface is conditioned with a suitable buffer solution to stabilize the baseline, as labelled as “(1)” in Figure 2.13a. Here, the change in temperature, hydrogel swelling, and other external factors will have no significant effect on the output signal. A solution containing the targeted molecules, known as analytes, is injected into the system. The association phase, labelled “(2),” begins as the ligand immobilizes the analytes. Other molecules could bind to the surface if an inappropriate ligand is selected. According to the sensorgram, the incident angle sharply rises at the initial of the association and slowly increases as it approaches the maximum angle. In addition, the binding kinetics of the analytes can be investigated during this stage. The system buffer solution is then flowed through the sensor’s surface during the disassociation phase, as depicted as the label “(3)”. The weakly bound analytes are flushed in this process, slightly reducing the plasmonic angle. However, the strongly bound analytes remain within the ligand complex. A regeneration solution (low-pH buffer) is injected into the system to return the detected angle to the baseline. This stage is known as the regeneration phase, labelled “(4)”. Here, the regeneration solution breaks the specific bonding between ligands and analytes. If the sensor is appropriately modified, the ligand must not be removed in this process. Finally, the sensor returns to its baseline, ready to perform another test. Figure 2.13b illustrates the binding mechanism of ligands and analytes in each phase.

SPR detection can also determine the concentration of analytes within the solution [86-88]. According to Figure 2.14, the sensorgram’s plots differ among the investigated concentrations. Firstly, the calibration curve can be acquired from the linear relation between the rate of change in the plasmonic angle concerning detection time and solution concentration. In this regard, the concentration of an unknown sample can be determined.

Another method for concentration determination without using the calibration curve is the

เอกสารนี้เป็นเอกสารที่สงวนไว้สำหรับการใช้งานเพื่อการศึกษาเท่านั้น ไม่อนุญาตให้นำไปใช้ประโยชน์ด้านการค้า  
ไม่ว่ากรณีใดๆ ทั้งสิ้น อีกทั้งห้ามมิให้ดัดแปลงเนื้อหา และต้องอ้างอิงถึงเจ้าของเอกสารทุกครั้งที่มีการนำไปใช้

so-called calibration-free concentration analysis (CFCA), introduced by Karlsson and Roos [89,90].

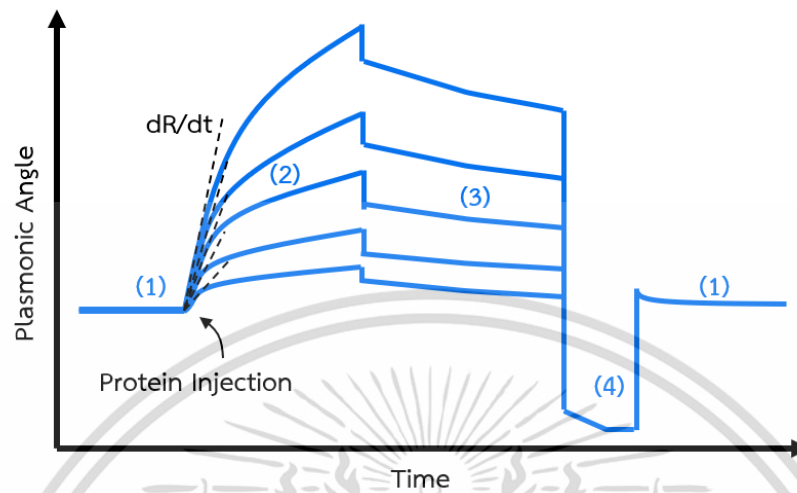
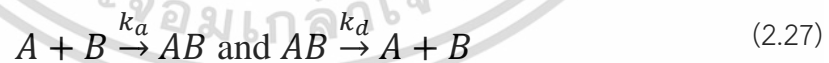


Figure 2.14 Shows the sensorgram's plots of the plasmonic angle responses for protein binding with different concentrations.

The association rate ( $k_a$ ) and disassociation rate ( $k_d$ ) are the other two crucial parameters for the study of biomolecular interaction. Equation (2.27) indicates the addition reaction between the ligand and analytes, given as A and B, respectively, where AB is the binding product. Relying on an analytes' concentrations of the solution,  $k_a$  and  $k_d$  can be computed using Equations (2.28) to (2.30). These two parameters can then be utilized to calculate the affinity constant,  $K_A$ , and the equilibrium disassociation constant,  $K_D$ , as expressed in Equations (2.31) and (2.32), respectively.



$$\frac{d[AB]}{dt} = k_a[A][B] \quad (2.28)$$

$$\frac{d[AB]}{dt} = k_d[AB] \quad (2.29)$$

$$k_a[A][B] = k_d[AB] \quad (2.30)$$

$$K_A = \frac{[AB]}{[A][B]} = \frac{k_a}{k_d} \quad (2.31)$$

$$K_D = \frac{[A][B]}{[AB]} = \frac{k_d}{k_a} \quad (2.32)$$

เอกสารนี้เป็นเอกสารที่สงวนไว้สำหรับการใช้งานเพื่อการศึกษาเท่านั้น ไม่อนุญาตให้นำไปใช้ประโยชน์ด้านการค้า  
ไม่ว่ากรณีใดๆ ทั้งสิ้น อีกทั้งห้ามมิให้ดัดแปลงเนื้อหา และต้องอ้างอิงถึงเจ้าของเอกสารทุกครั้งที่มีการนำไปใช้

Where  $[A]$ ,  $[B]$ , and  $[AB]$  are the concentration of the ligand, analytes, and their products of the biomolecular interaction.

Apart from protein kinetics, SPR technology has been employed in numerous applications, such as voltage sensing [16], microscopic imaging [9], virology [91,92], ultrasonic detection [15], and drug design [11,12]. Nevertheless, this thesis presents a theoretical investigation of the SPR limitation and sensing mechanism, which relies on biomolecular interactions. Thus, only the experiment concerning protein binding is described.

## 2.7 Quantitative Sensing Performance Parameters

In this theoretical investigation, five main quantitative performance parameters regarding angular scanning have been discussed.

### 2.7.1 Plasmonic Angle

Plasmonic angle ( $\theta_{sp}$ ) determines an angle which the SPR spectrum reaches its minimum, as illustrated in Figure 2.15. The parameter can provide a brief analysis of the range of detection. For instance, in the case where a control spectrum has a large plasmonic angle, the possible shifting distance due to refractive index changes is small. As a result, a small detection range is attained.

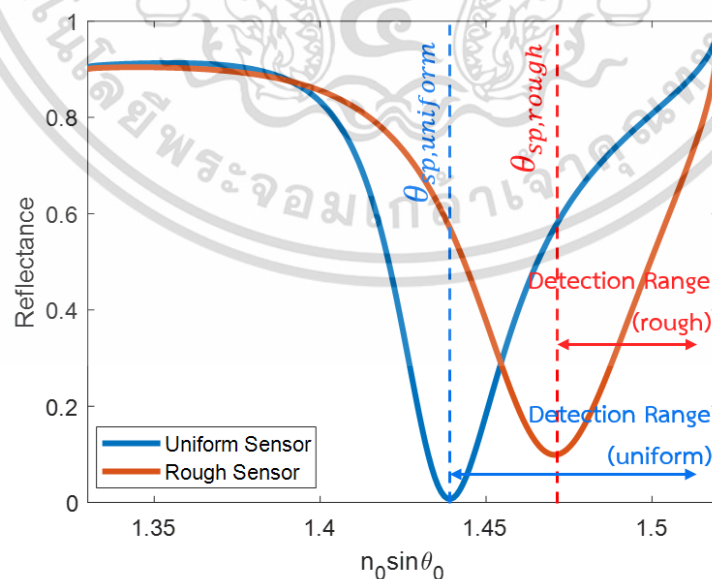


**Figure 2.15** Shows the SPR responses from an ideal uniform gold sensor (blue) and a rough gold sensor (red), indicating the difference between their detection ranges.

เอกสารนี้เป็นเอกสารที่สงวนไว้สำหรับการใช้งานเพื่อการศึกษาเท่านั้น ไม่อนุญาตให้นำไปใช้ประโยชน์ด้านการค้า ไม่ว่าจะกรณีใดๆ ทั้งสิ้น อีกทั้งห้ามมิให้ดัดแปลงเนื้อหา และต้องอ้างอิงถึงเจ้าของเอกสารทุกครั้งที่มีการนำไปใช้

### 2.7.2 Sensitivity

Sensitivity defines the shifting distance of the plasmonic angle with respect to the alternation of a sensing region's environment. Generally, sensitivity in SPR detection is classified as bulk sensitivity and binding sensitivity, as shown in Figures 2.16a and 2.16b, respectively. Bulk sensitivity indicates the sensitivity under the change of an overall refractive index in the sensing area. The factor is usually employed in the refractive index sensing. On the other hand, binding sensitivity relies on the presence of a protein binding layer in the sensing region. This study involves binding sensitivity only, which can be calculated as expressed in Equation (2.33).

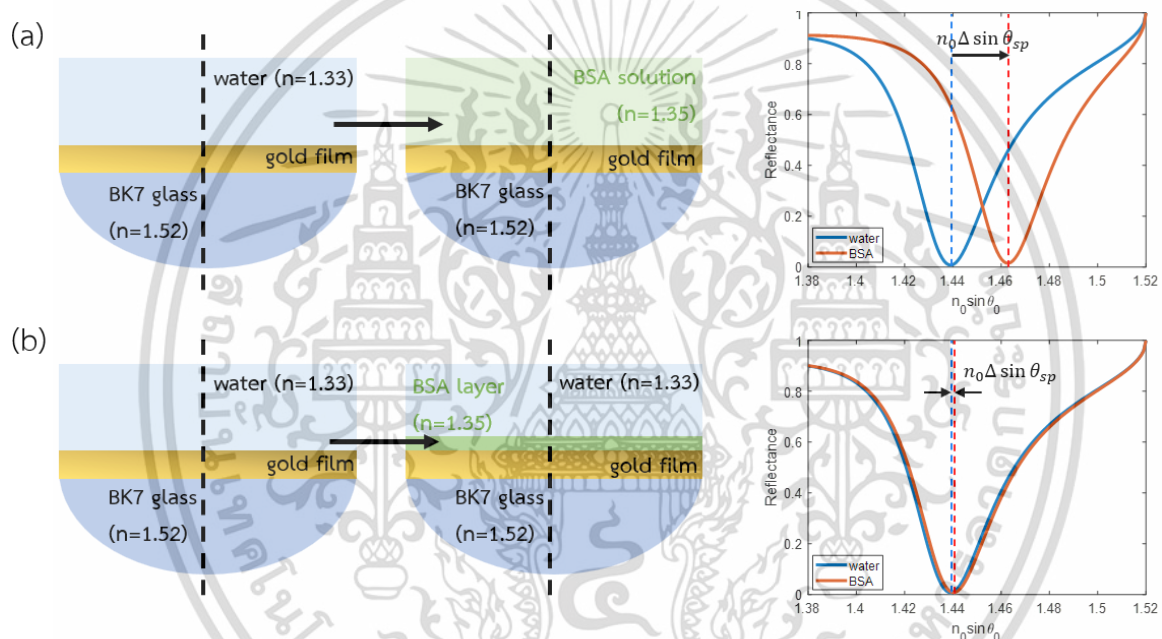


Figure 2.16 Shows schematics of (a) a bulk sensitivity detection and (b) a binding sensitivity detection with an initial sensing region as a water-based environment and an alternated sensing region as BSA solution (bulk) and BSA binding layer (binding).

$$Sensitivity = \frac{\Delta k}{\Delta n_s h_{BSA}} = \frac{2\pi n_0 \Delta \sin \theta_{sp}}{\lambda} \cdot \frac{1}{\Delta n_s h_{BSA}} \quad (2.33)$$

Where  $n_0$  is the refractive index of a glass substrate.

$\Delta \sin \theta_{sp}$  is the change in sine values of the plasmonic angles (one from the controlled environment and another from the alternated environment).

$\Delta n_s$  is the difference between the refractive indices of initial and changed sensing regions.

เอกสารนี้เป็นเอกสารที่สงวนไว้สำหรับการใช้งานเพื่อการศึกษาเท่านั้น ไม่อนุญาตให้นำไปใช้ประโยชน์ด้านการค้า  
ไม่ว่ากรณีใดๆ ทั้งสิ้น อีกทั้งห้ามมิให้ดัดแปลงเนื้อหา และต้องอ้างอิงถึงเจ้าของเอกสารทุกครั้งที่มีการนำไปใช้

$h_{BSA}$  is the thickness of protein binding layer (if available).

$\lambda$  is the incident beam's wavelength.

### 2.7.3 Full Width at Half Maximum

The full width at half maximum, or FWHM, indicates the width of an SPR curve measured at 50% of the whole intensity, as illustrated in Figure 2.17a. FWHM plays a significant role in the assessment of a sensor's performance. Figure 2.17b indicates a large FWHM detection which can result in ambiguity and uncertainty of a sensor's output, compared to a low-FWHM detection. Furthermore, there are various techniques concerning FWHM measurement, such as Horner's curve fitting [93], Green's function [94], and Lorentzian fit [95]. In this thesis, the FWHM of an SPR detection can be calculated using Equation (2.34).

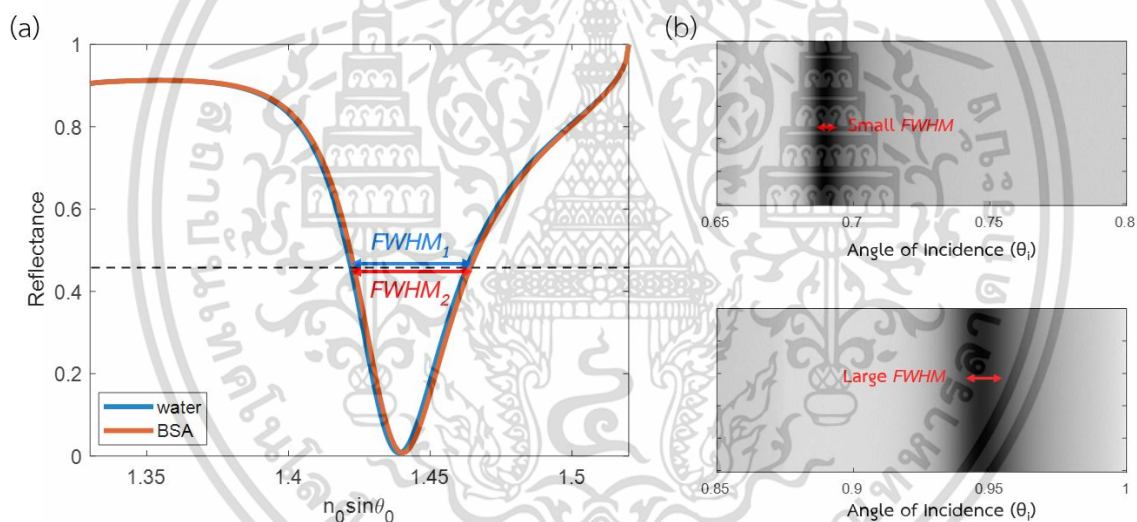


**Figure 2.17** Shows (a) a schematic of the *FWHM* measurement for SPR detection and (b) a comparison between small and large *FWHM* responses simulated from an air-based and water-based sensing region, respectively. Note that the angular scanning ranges are identical.

$$FWHM = \frac{\Delta k_{1,normalized} + \Delta k_{2,normalized}}{2} \quad (2.34)$$

Where  $\Delta k_{1,normalized}$  and  $\Delta k_{2,normalized}$  are the width of the normalized SPR spectra measured from the controlled and alternated sensing area at 50% reflectance.

เอกสารนี้เป็นเอกสารที่สงวนไว้สำหรับการใช้งานเพื่อการศึกษาเท่านั้น ไม่อนุญาตให้นำไปใช้ประโยชน์ด้านการค้า  
ไม่ว่ากรณีใดๆ ทั้งสิ้น อีกทั้งห้ามมิให้ดัดแปลงเนื้อหา และต้องอ้างอิงถึงเจ้าของเอกสารทุกครั้งที่มีการนำไปใช้

### 2.7.4 Intensity Contrast

Intensity contrast ( $\Delta I$ ) defines the difference between the SPR spectrum's highest and lowest intensity, as illustrated in Figure 2.18a. Similar to the FWHM, the  $\Delta I$  can significantly affect the clarity of the sensor's outputs. Figure 2.18b compares the low- $\Delta I$  and high- $\Delta I$  SPR detections. This theoretical investigation determines the average  $\Delta I$  using Equation (2.35).

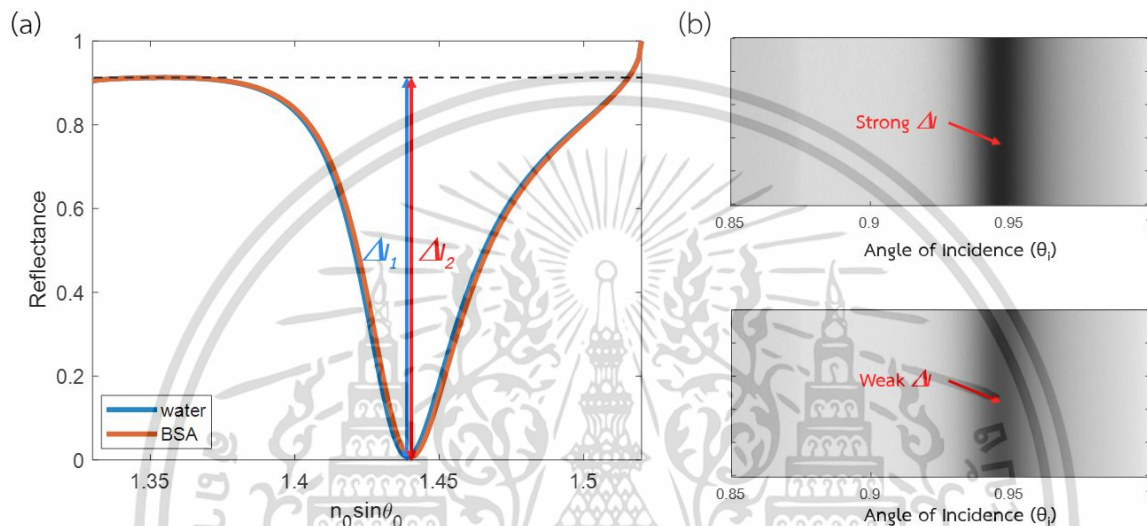


Figure 2.18 Shows (a) a schematic of the  $\Delta I$  measurement for SPR detection and (b) a comparison between strong and weak  $\Delta I$  responses simulated from an ideal SPR-based sensor and a sensor with 20% degraded in intensity, respectively.

$$\Delta I = \frac{\Delta I_1 + \Delta I_2}{2} \quad (2.35)$$

Where  $\Delta I_1$  and  $\Delta I_2$  are the intensity contrast of the SPR spectra measured from the initial and final environment.

### 2.7.5 Plasmonic Intensity

Plasmonic intensity ( $I_{sp}$ ) determines the intensity at the plasmonic angle, the SPR reflectance's lowest intensity, as shown in Figure 2.19. The parameter has a similar impact to the  $\Delta I$ . The  $I_{sp}$  in this project was calculated using Equation (2.36).

$$I_{sp} = \frac{I_{sp,1} + I_{sp,2}}{2} \quad (2.36)$$

เอกสารนี้เป็นเอกสารที่สงวนไว้สำหรับการใช้งานเพื่อการศึกษาเท่านั้น ไม่อนุญาตให้นำไปใช้ประโยชน์ด้านการค้า  
ไม่ว่ากรณีใดๆ ทั้งสิ้น อีกทั้งห้ามมิให้ดัดแปลงเนื้อหา และต้องอ้างอิงถึงเจ้าของเอกสารทุกครั้งที่มีการนำไปใช้

Where  $I_{sp,1}$  and  $I_{sp,2}$  are the intensity at the plasmonic angle of the SPR curves attained from the controlled and alternated environment.

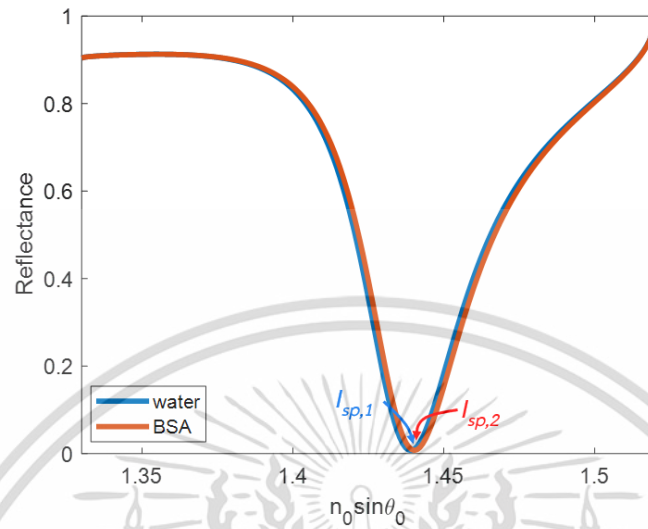


Figure 2.19 Shows a schematic of the  $I_{sp}$  measurement for SPR detection.

#### 2.7.6 Figure of Merit

The figure of merit (FOM) indicates the sensor's overall performance. Traditional sensor's FOM, given as  $FOM_0$  has sensitivity and FWHM involved only, as expressed in Equation (2.37). Nevertheless, an output of SPR detection has two other unique parameters,  $\Delta I$  and  $I_{sp}$ , which must also be considered. Treesukon et al. [96] have recently published an investigation regarding the mathematical formula for SPR detection's FOM. Equation (2.38) defines the mathematical expression for this FOM, given as  $FOM_{SPR}$ .

$$FOM_0 = \frac{\text{Sensitivity}}{FWHM} \quad (2.37)$$

$$FOM_{SPR} = \frac{\text{Sensitivity} \times \sqrt{\Delta I}}{FWHM \times \sqrt{I_{sp}}} \quad (2.38)$$

เอกสารนี้เป็นเอกสารที่สงวนไว้สำหรับการใช้งานเพื่อการศึกษาเท่านั้น ไม่อนุญาตให้นำไปใช้ประโยชน์ด้านการค้า  
ไม่ว่ากรณีใดๆ ทั้งสิ้น อีกทั้งห้ามมิให้ดัดแปลงเนื้อหา และต้องอ้างอิงถึงเจ้าของเอกสารทุกครั้งที่มีการนำไปใช้

## CHAPTER 3

### METHODOLOGY

#### 3.1 Simulation of Rough Surface Structures

The rough surface of gold film was generated using numerical modeling with Gaussian random surfaces [97], as implemented by Byun et al. [28], and was characterized by varying roughness height ( $h$ ) and roughness correlation length ( $cl$ ) from 2 nm to 20 nm and 5 nm to 50 nm, respectively. SPR excitation and its cut-off positions were covered in these ranges of roughness factors. The chosen roughness scope contains a variety of mode characteristics, including LSPR effects and increased protein binding density, which will be discussed further in the later section.

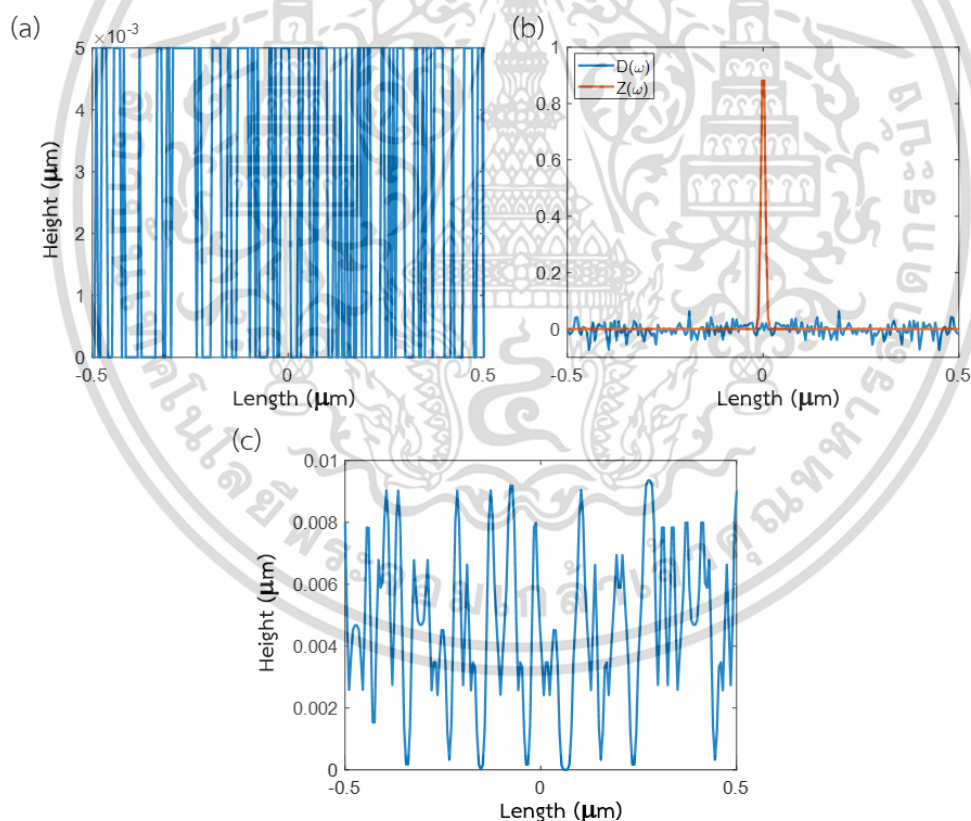


**Figure 3.1** Shows the process of the Gaussian random surfaces technique, which includes (a) an illustration of function  $d(x)$ , (b) a multiplication step of  $D(\omega)$  and  $Z(\omega)$ , and (c) the resulting surface profile,  $s(x)$ .

เอกสารนี้เป็นเอกสารที่สงวนไว้สำหรับการใช้งานเพื่อการศึกษาเท่านั้น ไม่อนุญาตให้นำไปใช้ประโยชน์ด้านการค้า  
 ไม่ว่ากรณีใดๆ ทั้งสิ้น อีกทั้งห้ามมิให้ดัดแปลงเนื้อหา และต้องอ้างอิงถึงเจ้าของเอกสารทุกครั้งที่มีการนำไปใช้

According to the Gaussian random surfaces, a function  $d(x)$  was first created, which consists of 0 and 1 arranged in random orders, where  $x$  is the spatial distance along the gold layer's surface in the  $x$ -axis. The  $d(x)$  was then multiplied by  $h$ ; here, the function is only composed of 0 and  $h$ . A frequency domain of the profile,  $D(\omega)$ , was later calculated as  $D(\omega) = F[d(x) \cdot h]$ , where  $\omega$  and  $F$  indicate the frequency domain axis and the Fourier transformation operator, respectively. Next, the frequency profile was multiplied by a Gaussian distribution function,  $Z(\omega) = e^{(-2x^2/cl^2)}$ ; the product was given as  $S(\omega)$ . The Gaussian distribution function is essentially a low-pass filter for the surface signal. Finally, the inverse Fourier transform is applied on  $S(\omega)$ , resulting in a surface function in the time domain depicted as  $s(x)$ . Figure 3.1 illustrates the procedures concerning Gaussian random surfaces in three significant steps. To summarize, the degree of roughness increases as  $h$  increases or  $cl$  decreases.

## 3.2 Simulated Structures for Rigorous Coupled-Wave Analysis

### 3.2.1 Identifying and Quantifying the Roots of Changes in Performance

Before employing the rigorous coupled-wave analysis (RCWA) [98,99], the spatial domain signals must be rearranged into a rectangular contour. The RCWA is a developed function for analysing the diffraction of an electromagnetic wave by complex structures, which can also be utilized for studying SPR detection. In this project, the  $s(t)$  was converted into a 200-column rectangular contour with a height of 0.1 nm for each layer. It is significant to point out that the greater number of columns employed will result in a more accurate model. Nevertheless, more considerable computing resources and simulation time are required. A description of an optimum number of columns will be provided in the later sections. Figure 3.2 illustrates simulated structures for the RCWA, which mainly consist of three components: a rough gold layer (yellow), a binding layer as BSA (green), and a sensing region as water (dark blue). BSA was selected as a substrate layer in this research due to its versatility in applications, including cell culture and biochemical studies. Furthermore, BSA has been broadly utilized as a protein concentration standard in laboratory experiments, including biomedical applications.

Three models were developed to study and quantify the effect from LSPR and increased surface area: no BSA model, BSA with no sidewall model (non-sidewall BSA), and BSA with sidewall (sidewall BSA). Figure 3.2a indicates the no BSA model where the

เอกสารนี้เป็นเอกสารที่สงวนไว้สำหรับการใช้งานเพื่อการศึกษาเท่านั้น ไม่อนุญาตให้นำไปใช้ประโยชน์ด้านการค้า  
ไม่ว่ากรณีใดๆ ทั้งสิ้น อีกทั้งห้ามมิให้ดัดแปลงเนื้อหา และต้องอ้างอิงถึงเจ้าของเอกสารทุกครั้งที่มีการนำไปใช้

BSA binding layer is absent. In the non-sidewall BSA model, a 5nm-thick BSA layer was employed only on the top of the roughness contour, as depicted in Figure 3.2b. This way, the protein amount is controlled and equivalent to the amount in the theoretical uniform gold sensor. Thus, this model allows us to study the LSPR effect from the rough surface. Lastly, the sidewall BSA model mimics the nature of the protein binding in the roughness profile. Here, the BSA binding layer coated the sensor's entire surface, including the rough surface's sidewall. In this regard, the SPR outputs from the third model will experience both the LSPR effect and the increased protein binding. However, at a slight roughness level, the sidewall protein can be overlapped by the protein lying on top, leading to an equivalent result in the non-sidewall model. On the other hand, the protein amount can be crucially increased at an extreme degree of roughness. This issue will be further discussed in the next chapter.

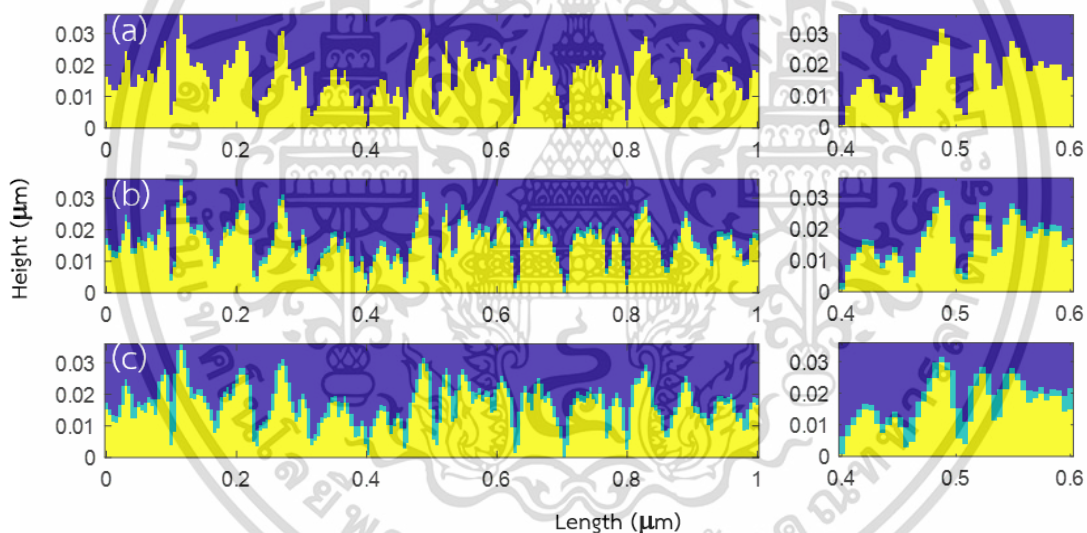


**Figure 3.2** Shows schematics of (a) the rough bare gold model, (b) the BSA with no sidewall model, and (c) the BSA with sidewall model, simulated using  $h$  of 18 nm and  $cl$  of 10 nm, and their zoom-in visuals of the surface structures.

Nonetheless, it is undeniable that the nature of protein coating on the sidewall is more complicated than the theoretical investigation. The BSA is meant to cover the rough surface and prevent it from being in contact with the buffer. However, in real cases, there could be an area, such as sharp edges, not covered by the protein binding, which can affect the precision of the investigated results. In this regard, the enhanced performance will be between the figure of merits of BSA with no sidewall and BSA with sidewall models.

เอกสารนี้เป็นเอกสารที่สงวนไว้สำหรับการใช้งานเพื่อการศึกษาเท่านั้น ไม่นิยมนำไปใช้ประโยชน์ด้านการค้า  
ไม่ว่ากรณีใดๆ ทั้งสิ้น อีกทั้งห้ามมิให้ดัดแปลงเนื้อหา และต้องอ้างอิงถึงเจ้าของเอกสารทุกครั้งที่มีการนำไปใช้

Moreover, the later sections will show that even a particular region in the non-sidewall BSA model could improve the sensor's quality due to an LSPR impact. Research on polymer technology [100-103] aid in protein fabrication control. Nuutinen et al. [101] and Saleem et al. [100] investigate the use of polymeric materials on resonant wave gratings (RWG). The protein layer was uniformly bound after  $\text{TiO}_2$  had been employed as a cover layer on the gratings structure. Mayet et al. [102] presented a similar analysis in which an oxide-nitride-oxide passivation layer was uniformly coated on the grating sidewalls. Furthermore, Zhang et al. [103] performed a theoretical investigation of protein sidewall coating on a metal-layer-assisted double-grating (MADG) biosensor. These findings demonstrate that the experimental and theoretical data agree well and that the protein coating behaviour is controllable.

### 3.2.2 Theoretically Investigated SPR-based Sensor

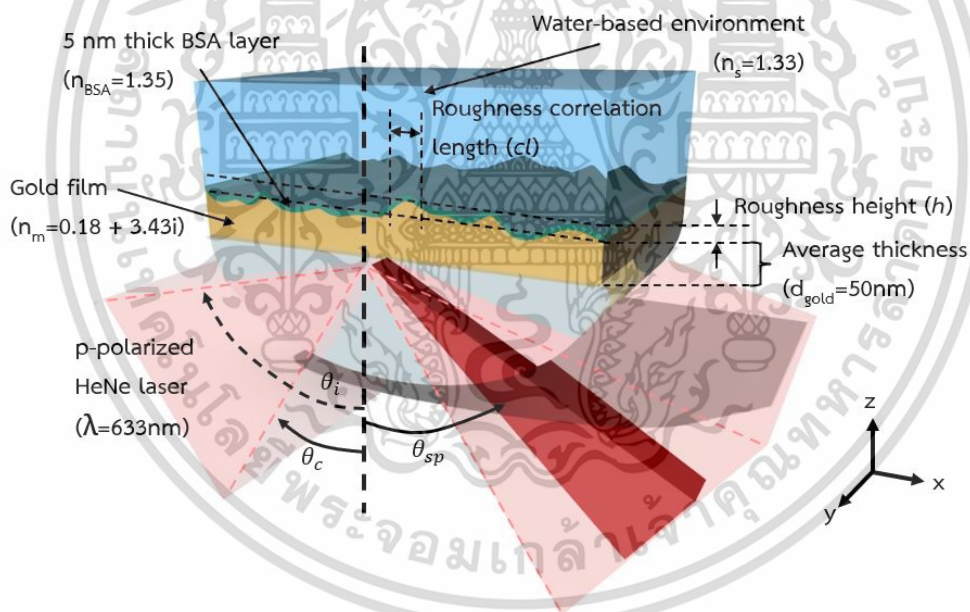


Figure 3.3 Shows the SPR-based sensor structure employed in the theoretical investigation.

Figure 3.3 illustrates the SPR-based sensor structure employed in the theoretical study. Note that the roughness structure is in x-dimension only, where the y-axis was treated as an infinite extension of the x-z planar. The model was a prism-based Kretschmann configuration and an incident beam with a TM-polarization or p-polarization.

The structure consists of a sensing region as water with a refractive index of 1.33, a 5 nm

เอกสารนี้เป็นเอกสารที่สงวนไว้สำหรับการใช้งานเพื่อการศึกษาเท่านั้น ไม่อนุญาตให้นำไปใช้ประโยชน์ด้านการค้า  
ไม่ว่ากรณีใดๆ ทั้งสิ้น อีกทั้งห้ามมิให้ดัดแปลงเนื้อหา และต้องอ้างอิงถึงเจ้าของเอกสารทุกครั้งที่มีการนำไปใช้

thick BSA binding layer with a concentration of 80 mg/mL and a refractive index of 1.35 as a binding analyte [104], a gold layer with a complex refractive index of  $0.18 + 3.43i$  [105], a glass substrate as BK7 glass prism, and an incident light as Helium-Neon (HeNe) laser with a wavelength of 633 nm. Furthermore, the gold film was classified as uniform and rough layers. To keep the gold material constant at an average height of 50 nm, the height of a uniform layer varied according to employed  $h$  in the rough layer. Here, the thickness of smooth and rough structures was given as  $2h$  and  $50 - h$  in nm, respectively. Moreover, the simulated angle of incidence was scanned from a critical angle to  $90^\circ$  (parallel to the sensor's surface).

### 3.2.3 Simulation of the SPR Detection

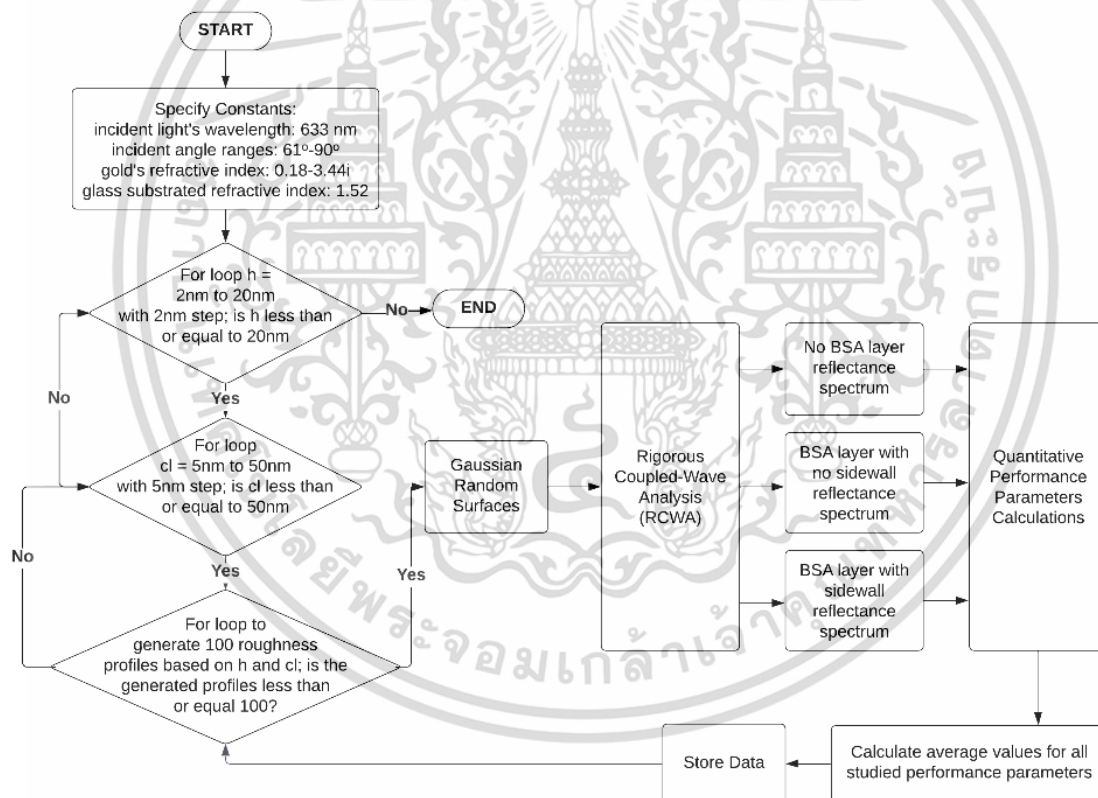


Figure 3.4 Shows the flowchart representing the theoretical investigation procedures [106].

This investigation mainly relies on the RCWA function to simulate the reflectance curves. Nonetheless, since the generated rough surfaces were randomly and physically different, lots of SPR spectra must be computed to yield high-precision quantitative

เอกสารนี้เป็นเอกสารที่สงวนไว้สำหรับการใช้งานเพื่อการศึกษาเท่านั้น ไม่อนุญาตให้นำไปใช้ประโยชน์ด้านการค้า  
ไม่ว่ากรณีใดๆ ทั้งสิ้น อีกทั้งห้ามมิให้ดัดแปลงเนื้อหา และต้องอ้างอิงถึงเจ้าของเอกสารทุกครั้งที่มีการนำไปใช้

performance factors. This process called the Monte-Carlo simulation [107], can enhance the results' accuracy and precision. The project utilized the Monte-Carlo simulation by simulating 100 reflectance spectra using RCWA for each h-cl pair and calculating the average performance value from those outputs. It is undeniable that increasing the number of simulated reflectance curves will improve even more accuracy; however, this will trade off with the computing time. In addition, parallel computing is employed to reduce the simulation time. The flow chart, depicted in Figure 3.4, shows the entire procedures for the SPR outputs simulation.

### 3.3 Enhancement and Deterioration Ratio

The LSPR effect and the protein increment were analysed from the non-sidewall BSA and sidewall BSA models in the term enhancement/deterioration ratio (*EDR*). In this part of the investigation, the relative change in sensitivity,  $FOM_0$ , and  $FOM_{SPR}$  were utilized in this calculation. In addition, the *EDR* was classified into three types: an *EDR* from the LSPR effect, an *EDR* from protein increment, and an *EDR* of both impacts, denoted as  $EDR_{LSPR,S}$ ,  $EDR_{protein,S}$ , and  $EDR_{total,S}$ . Equations (3.1) to (3.3) indicate the mathematical formulas for these terms.

$$EDR_{LSPR,S} = \frac{S_{non-sidewall}}{S_{uniform}} \quad (3.1)$$

$$EDR_{protein,S} = \frac{S_{sidewall} - S_{non-sidewall}}{S_{uniform}} \quad (3.2)$$

$$EDR_{total,S} = \frac{S_{sidewall}}{S_{uniform}} \quad (3.3)$$

Where  $S_{uniform}$ ,  $S_{non-sidewall}$ , and  $S_{sidewall}$  indicate the sensitivity values for the ideal uniform sensor model, BSA with no sidewall, and BSA with sidewall model, respectively.

$EDR_{LSPR,S}$ ,  $EDR_{protein,S}$ , and  $EDR_{total,S}$  depict the three types of *EDR* for sensitivity.

The *EDR* for  $FOM_0$  and  $FOM_{SPR}$  can be calculated using the relative change of the figure of merit value similar to an *EDR* for sensitivity.

เอกสารนี้เป็นเอกสารที่สงวนไว้สำหรับการใช้งานเพื่อการศึกษาเท่านั้น ไม่อนุญาตให้นำไปใช้ประโยชน์ด้านการค้า  
ไม่ว่ากรณีใดๆ ทั้งสิ้น อีกทั้งห้ามมิให้ดัดแปลงเนื้อหา และต้องอ้างอิงถึงเจ้าของเอกสารทุกครั้งที่มีการนำไปใช้

## CHAPTER 4

### RESULTS

#### 4.1 Convergence Tests

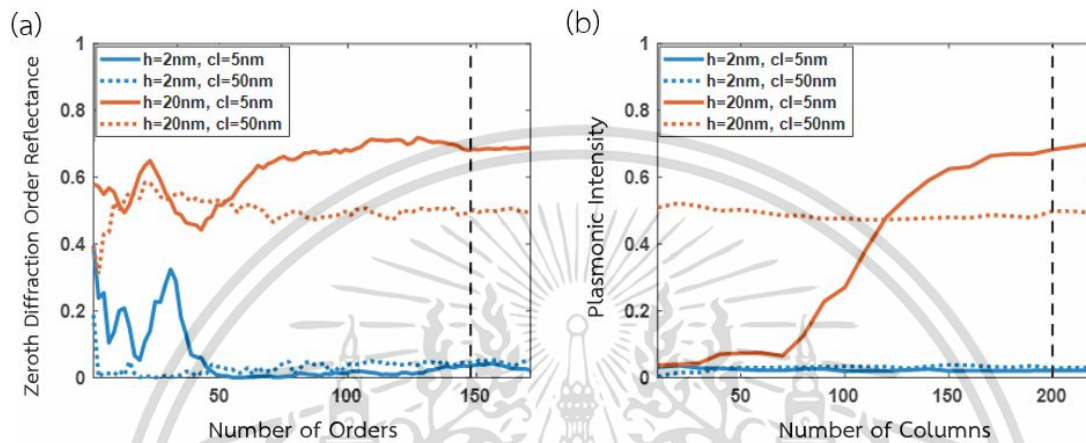


Figure 4.1 Shows results of (a) a convergence test on the number of diffraction orders and (b) a convergence test on the number of columns employed for four extreme cases of roughness profile [106].

The convergence test on the optimal number of diffraction orders was utilized for the four extreme cases of the investigation, which consisted of rough surfaces generated using (a)  $h$  of 2 nm and  $cl$  of 5 nm, (b)  $h$  of 20 nm and  $cl$  of 5 nm, (c)  $h$  of 2 nm and  $cl$  of 50 nm, and (d)  $h$  of 20 nm and  $cl$  of 50 nm, as illustrated in Figure 4.1a. The RCWA was employed to calculate the p-polarised HeNe laser's reflectance with multiple diffraction orders ranging from 1 to 171. The numerical fluctuation between the number of orders of 151 was  $7 \times 10^{-4}$ , 0.002, 0.020, and 0.003 for the four tested rough surfaces. Undeniably, a greater number of diffraction orders will yield lower fluctuation values; however, longer computing time and resources would be required. In this regard, the number of diffraction orders of 151 was employed in this research.

Figure 4.1b depicts the convergence test on the employed number of columns representing the rough surfaces. The number of columns ranging from 10 to 220 was investigated as the average  $I_{sp}$  of the three studied models which mentioned in section 3.2.1. Furthermore, the roughness convergence test was engaged in the same extreme cases. The fluctuation values, computed as a difference of  $I_{sp}$  between 200-columns and

เอกสารนี้เป็นเอกสารที่สงวนไว้สำหรับการใช้งานเพื่อการศึกษาเท่านั้น ไม่อนุญาตให้เผยแพร่ไปใช้ประโยชน์ด้านการค้า  
ไม่ว่ากรณีใดๆ ทั้งสิ้น อีกทั้งห้ามมิให้ดัดแปลงเนื้อหา และต้องอ้างอิงถึงเจ้าของเอกสารทุกครั้งที่มีการนำไปใช้

220-columns model, for (a)  $h$  of 2 nm and  $cl$  of 5 nm, (b)  $h$  of 20 nm and  $cl$  of 5 nm, (c)  $h$  of 2 nm and  $cl$  of 50 nm, and (d)  $h$  of 20 nm and  $cl$  of 50 nm were  $7 \times 10^{-4}$ , 0.002, 0.018, and 0.005. Therefore, the number of columns for the roughness model of 200 is adequate for the simulation of roughness frameworks.

## 4.2 Simulation VS Experiment

Undeniably, there is a controversy about whether the results from the combination of an RCWA simulation and Monte-Carlo simulation will be as accurate as the experimental results. Yang et al. [108] investigated the SPR spectra for a gold-based SPR sensor at roughness profiles. The experimental SPR-based sensor is composed of a 57.5 nm thick gold film, a sensing region as an air-based environment, and an incident wavelength of 632.8 nm. These gold films were sputter coated and then thermally annealed at 100°C, 200°C, 300°C, and 400°C for 15 minutes, yielding four surfaces with different root-mean-square (RMS) roughness. These RMS roughness values were measured with an atomic force microscope (AFM).

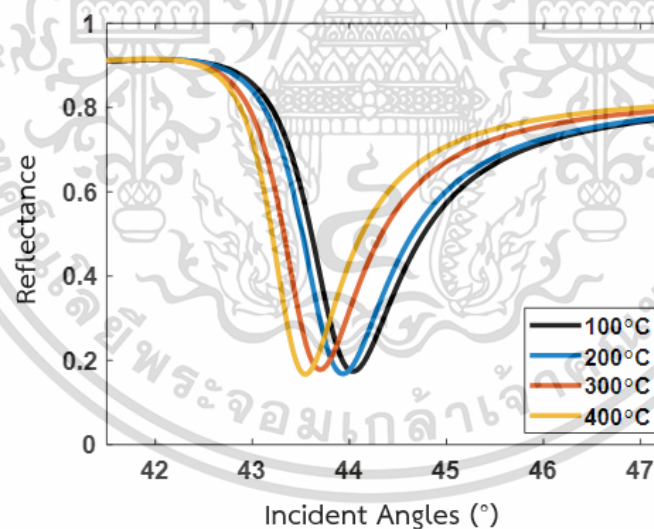


Figure 4.2 Shows the SPR spectra simulated based on the proposed roughness parameters reported by Yang et al. [106,108].

The reflectance spectra, as illustrated in Figure 4.2, were simulated based on the mentioned sensor's properties with a roughness level presented by Yang et al. The employed RMS roughness level, the experimental result of plasmonic angles, and the simulated reflectance curves' plasmonic angles are shown in Table 4.1. The  $h$  was

เอกสารนี้เป็นเอกสารที่สงวนไว้สำหรับการใช้งานเพื่อการศึกษาเท่านั้น ไม่อนุญาตให้นำไปใช้ประโยชน์ด้านการค้า  
ไม่ว่ากรณีใดๆ ทั้งสิ้น อีกทั้งห้ามมิให้ดัดแปลงเนื้อหา และต้องอ้างอิงถึงเจ้าของเอกสารทุกครั้งที่มีการนำไปใช้

reported; however, the  $cl$  was approximated from the AFM images. The information indicates that these values agree well with a minor discrepancy of  $0.09^\circ$  maximum. In the actual investigation, the gold film might not have been completely purified, which resulted in a slight difference between the results.

**Table 4.1** Indicates the plasmonic angle obtained from an experiment by Yang et al. [108] and the RCWA simulation for the proposed rough surfaces.

Thermal Annealing Temperature ( $^\circ\text{C}$ )	RMS Roughness (nm)	$h$ (nm)	$cl$ (nm)	Experimental $\theta_{sp}$ ( $^\circ$ )	Simulated $\theta_{sp}$ ( $^\circ$ )
100	1.260	6.1	20	44.04	44.04
200	0.906	3.7	20	43.94	43.93
300	0.700	2.9	30	43.75	43.70
400	0.415	1.5	30	43.65	43.56

### 4.3 Quantitative Performance Parameters for Investigated Surfaces

#### 4.3.1 Quantitative Performance Factors for Ideal Uniform Gold Sensor

To identify the theoretical limits of the SPR-based sensor, quantitative performance parameters for the theoretical uniform gold sensor were computed. The calculated  $\theta_{sp}$ , sensitivity, FWHM,  $\Delta I$ ,  $I_{sp}$ ,  $FOM_0$ , and  $FOM_{SPR}$  were  $71.33^\circ$ ,  $122.59 \text{ rad}/\mu\text{m}^2$ ,  $0.41 \text{ rad}\cdot\text{RIU}/\mu\text{m}$ ,  $0.90$ ,  $0.007$ ,  $299.00$ , and  $980.66$ , respectively. These values were calculated using Equations (2.33) to (2.38).

#### 4.3.2 Rough SPR-based Sensor: Plasmonic Angle

The average  $\theta_{sp}$  for the no BSA model, BSA with no sidewall model, and BSA with sidewall model at the investigated roughness region were indicated in Figure 4.3a. As described in section 2.7.1, the parameter is crucial for analysing the detection limit. Here, the rough surfaces with a  $cl$  of  $20 \text{ nm}$  were analysed and  $h$  was varied from  $0 \text{ nm}$  (ideal uniform surface) to  $15 \text{ nm}$ , as indicated in Figure 4.3b. It is observed that the  $\theta_{sp}$  increased as the roughness rose, resulting in a reduction of the detection limit. However, at  $h$  of  $15 \text{ nm}$ , the  $\theta_{sp}$  decreased, moderately recovered its limit of detection.

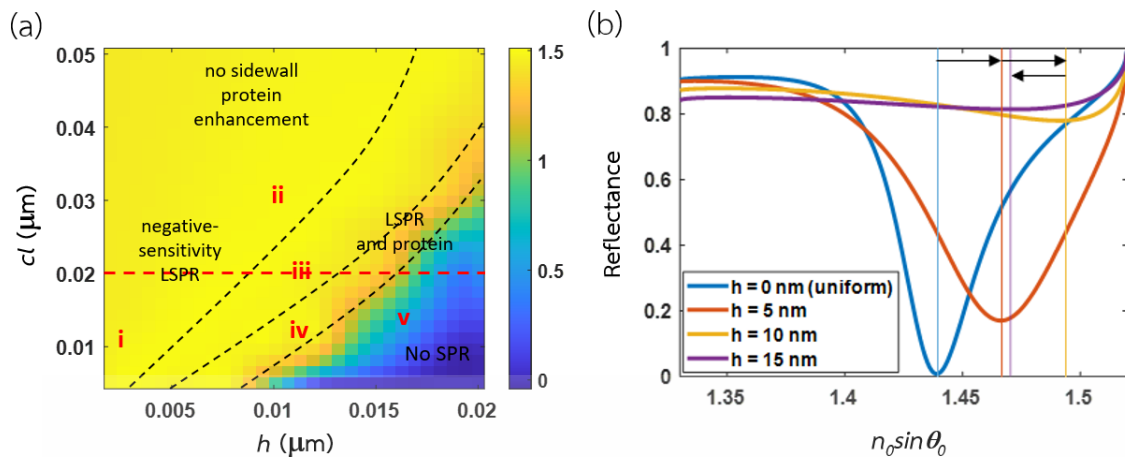


Figure 4.3 Shows (a) the average plasmonic angle as  $n_0 \sin \theta_{sp}$  for different roughness profiles, and (b) the SPR spectra simulated from surfaces with  $h$  of 0 nm (ideal uniform surface), 5 nm, 15 nm, and 20 nm, and an equivalent  $cl$  of 20 nm [106].

#### 4.3.3 Rough SPR-based Sensor: Sensitivity

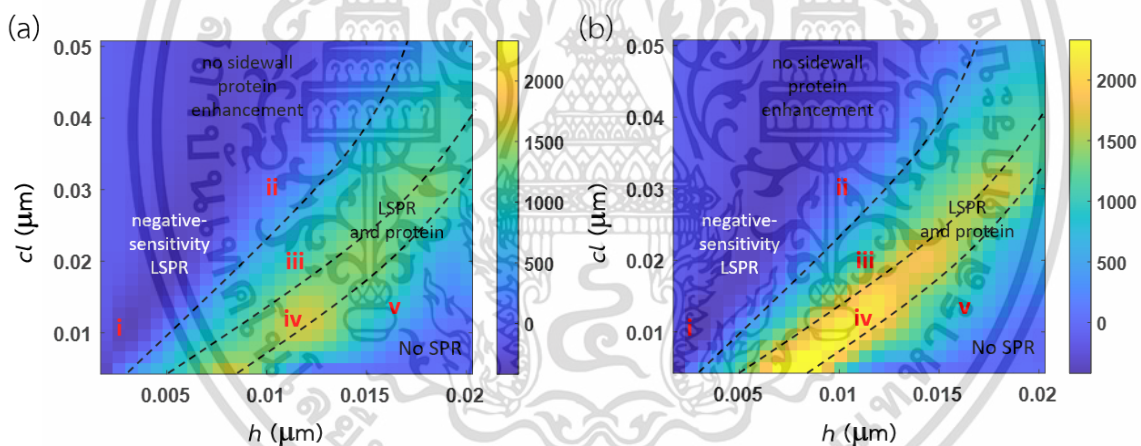


Figure 4.4 Shows the sensitivity in  $\text{rad}/\mu\text{m}^2$  obtained at different roughness profiles from (a) the BSA with no sidewall model and (b) the BSA with a sidewall model [106].

The binding sensitivity for the BSA with no sidewall model and the BSA with sidewall model was investigated for the mentioned roughness ranges, calculated using Equation (2.33), as illustrated in Figure 4.4. According to the results, the analysis of sensitivity was classified into four primary regions:

- (1) The "no sidewall protein enhancement" indicates a region where the sidewall protein is absent. In other words, because the roughness was relatively small, the appearance of sidewall protein was overlapped by the protein above the

เอกสารนี้เป็นเอกสารที่สงวนไว้สำหรับการใช้งานเพื่อการศึกษาเท่านั้น ไม่อนุญาตให้นำไปใช้ประโยชน์ด้านการค้า  
ไม่ว่ากรณีใดๆ ทั้งสิ้น อีกทั้งห้ามมิให้ดัดแปลงเนื้อหา และต้องอ้างอิงถึงเจ้าของเอกสารทุกครั้งที่มีการนำไปใช้

roughness peaks. In this regard, the non-sidewall BSA and the sidewall BSA models had no significant difference. Furthermore, it can be concluded that the only enhancement or deterioration effect came from the LSPR only. The SPR spectra yielded a negative sensitivity at the minimal roughness levels, labelled as “negative-sensitivity LSPR”. Here, the  $\theta_{SP}$  decreased concerning the appearance of the binding layer. The most negative sensitivity of  $-379.88 \text{ rad}/\mu\text{m}^2$  was obtained at  $h$  and  $cl$  of 3 nm and 10 nm, respectively, given as operating roughness “i”. Despite the unusual measuring technique, it was observed that the magnitude of the obtained sensitivity was threefold greater than the theoretical smooth sensor’s sensitivity. In addition, if the roughness was further increased toward the region’s boundary, the SPR reacquired its positive sensitivity property. However, the resulting binding sensitivity was degraded. Operating surface “ii” indicates the roughness at  $h$  of 10 nm and  $cl$  of 30 nm, yielding a sensitivity of only  $85.31 \text{ rad}/\mu\text{m}^2$  with a 30.41% reduction from an ideal uniform sensor. Figures 4.5a and 4.5b illustrate the reflectance spectra acquired from the operating surfaces “i” and “ii”.

- (2) The “positive-sensitivity LSPR” corresponds to a region where the reflectance curves were mainly affected by the LSPR wave effect. There was also a protein increment in this region; nevertheless, the amount was insignificant. Nevertheless, the sensitivity within the area was improved due to this wave effect. For instance, operating surface “iii” ( $h$  of 12 nm and  $cl$  of 20 nm) yielded a binding sensitivity of  $996.11 \text{ rad}/\mu\text{m}^2$  and  $1280.00 \text{ rad}/\mu\text{m}^2$  for the non-sidewall BSA model and sidewall BSA model, respectively. The reflectance spectra at this operating surface were depicted in Figure 4.5d.
- (3) The “LSPR and protein” indicates a rougher surface region where the SPR spectra were crucially affected by both LSPR and an increased binding area. Here, the roughness profile with  $h$  and  $cl$  of 9 nm and 8 nm, respectively, was chosen as the operating surface “iv”, which yielded reflectance curves shown in Figure 4.5c. In this operating surface, the non-sidewall BSA model acquired a sensitivity of  $1191.13 \text{ rad}/\mu\text{m}^2$ . This enhancement represents that the sensitivity had increased 9.72 times due to the LSPR effect alone. On the other hand, the BSA with sidewall model achieved an even greater sensitivity of  $1608.02 \text{ rad}/\mu\text{m}^2$ , which was 35% more than the non-sidewall BSA model’s sensitivity. This extraordinarily high

เอกสารนี้เป็นเอกสารที่สงวนไว้สำหรับการใช้งานเพื่อการศึกษาเท่านั้น ไม่อนุญาตให้นำไปใช้ประโยชน์ด้านการค้า

ไม่ว่ากรณีใดๆ ทั้งสิ้น อีกทั้งห้ามมิให้ดัดแปลงเนื้อหา และต้องอ้างอิงถึงเจ้าของเอกสารทุกครั้งที่มีการนำไปใช้

sensitivity was due to the deterioration in the SPR spectra, reducing the  $\theta_{SP}$  as mentioned in previous section. In addition, the percentage indicates the enhancement effect due to an increase in binding layer density, which agrees well with the percent increase in protein amount expressed in Figure 4.6.

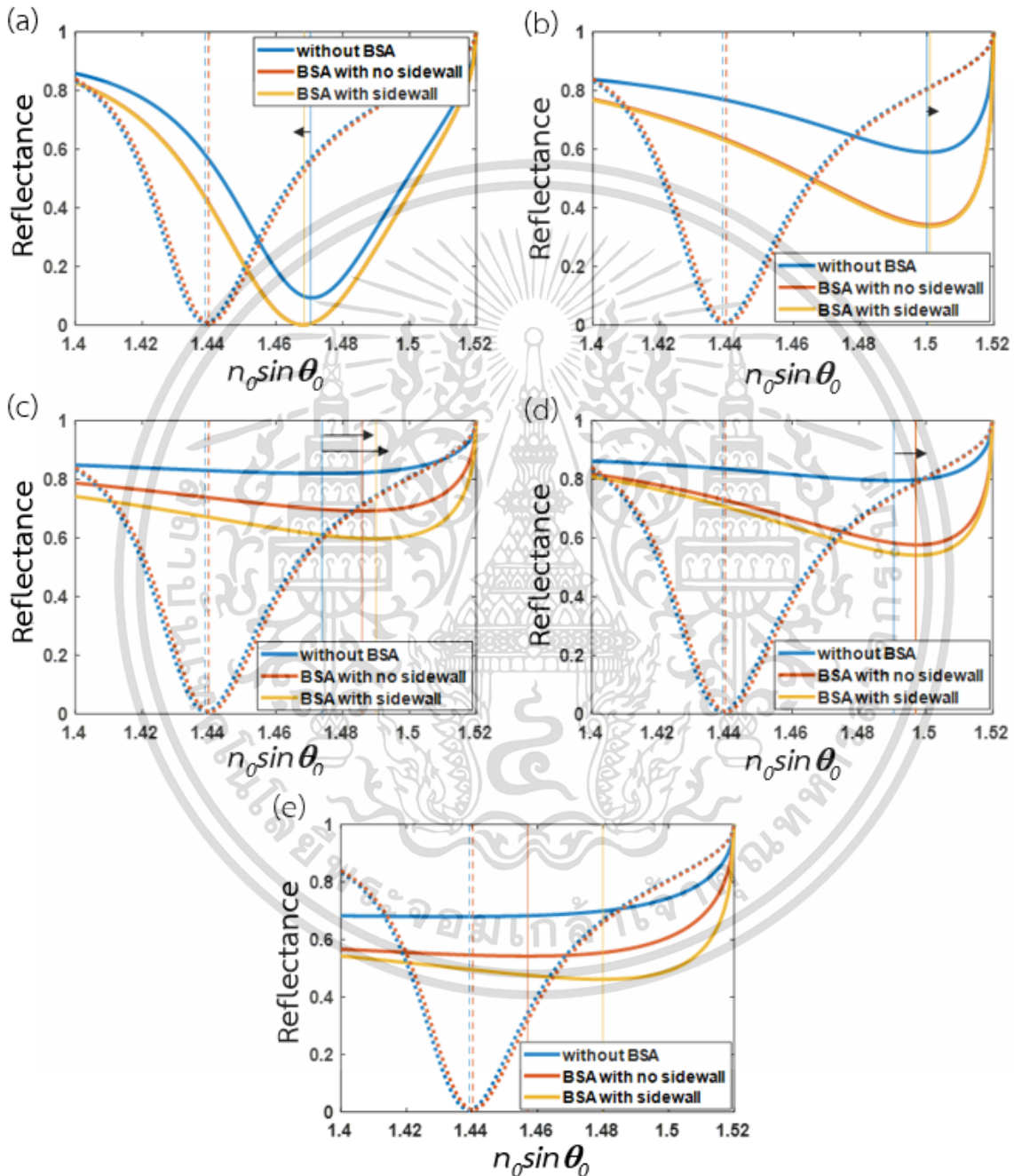


Figure 4.5 Shows the reflectance spectra obtained from (a) the operating surface “i”, (b) the operating surface “ii”, (c) the operating surface “iv”, (d) the operating surface “iii”, and (e) the operating surface “v”. Note that the dashed lines indicate the SPR response from the theoretical smooth surface sensor [106].

เอกสารนี้เป็นเอกสารที่สงวนลิขสิทธิ์กับการแข่งขันเพื่อการศึกษาเท่านั้น ไม่อนุญาตให้เผยแพร่ไปใช้ประโยชน์ด้านการค้า  
ไม่ว่ากรณีใดๆ ทั้งสิ้น อีกทั้งห้ามมิให้ตัดแปลงเนื้อหา และต้องอ้างอิงถึงเจ้าของเอกสารทุกครั้งที่มีการนำไปใช้

- (4) The “no SPR” is located at the extreme roughness level. Here, the rough surface profile provided a scattering loss [109] which completely deteriorated the structure of SPR curves, resulting in an unidentified  $\theta_{SP}$ . Moreover, the propagation length of SPP was crucially distorted due to rough surfaces, making the SPR undetectable [110]. Thus, this region cannot compute the sensitivity,  $FWHM$ ,  $\Delta I$ , and the figure of merit. As illustrated in Figure 4.5e, the reflectance spectra indicate the SPR output in the “no SPR” region, measured at the roughness with  $h$  of 18 nm and  $cl$  of 15 nm, given as an operating surface “v”.

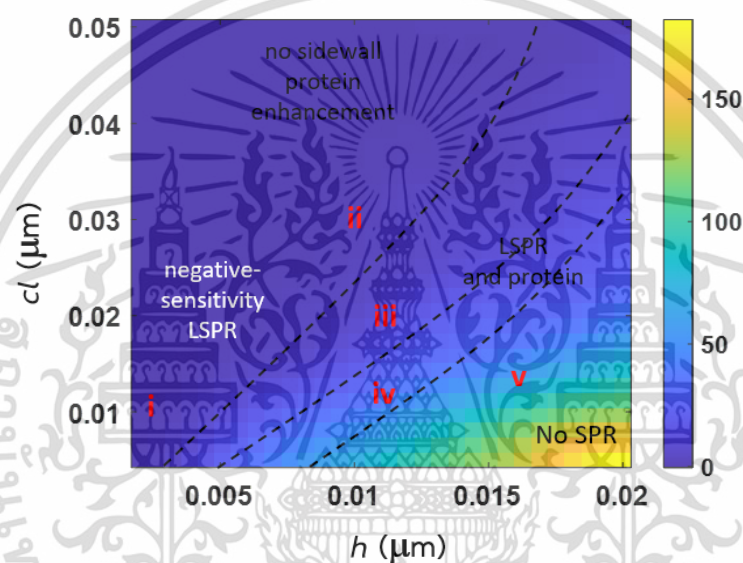


Figure 4.6 Shows the protein increment in percent due to the presence of sidewall protein on roughness profiles [106].

Figure 4.6 illustrates the increase in the binding BSA in percent as the roughness levels changed. This percentage of the additional sidewall protein was calculated by subtracting the sidewall BSA model from the BSA with no sidewall model and then divided by the initial protein amount. According to Figure 4.6, the protein increment in the “no sidewall protein enhancement” was negligible; however, the sidewall protein began to significantly affect the sensor’s performance at the “positive-sensitivity LSPR”. At an SPR operating roughness (with SPR dip structure retained), the highest protein increment was 40%.

เอกสารนี้เป็นเอกสารที่สงวนไว้สำหรับการใช้งานเพื่อการศึกษาเท่านั้น ไม่อนุญาตให้นำไปใช้ประโยชน์ด้านการค้า  
ไม่ว่ากรณีใดๆ ทั้งสิ้น อีกทั้งห้ามมิให้ดัดแปลงเนื้อหา และต้องอ้างอิงถึงเจ้าของเอกสารทุกครั้งที่มีการนำไปใช้

#### 4.3.4 Rough SPR-based Sensor: Full Width at Half Maximum

Figure 4.7a illustrates the *FWHM* for different rough surfaces, calculated as an average as expressed in Equation (2.34). The *FWHM* obtained from the BSA with no sidewall model and BSA with a sidewall model were not significantly different. Thus, only the non-sidewall model's *FWHM* was presented. At the gradual roughness level, with  $h$  of less than 5 nm, the parameter was primarily affected by  $h$  alone. The  $cl$  started to degrade the *FWHM after exceeding the threshold. In addition, it is concluded that the degraded *FWHM* originated from the LSPR wave effect only, while the additional protein has no effect. As depicted in Figure 4.7b, the reflectance spectra were obtained at a rough surface with  $h$  of 18 nm and  $cl$  of 40 nm. The hereby surface was selected to demonstrate the increase in *FWHM* of approximately twice the uniform sensor's value.*

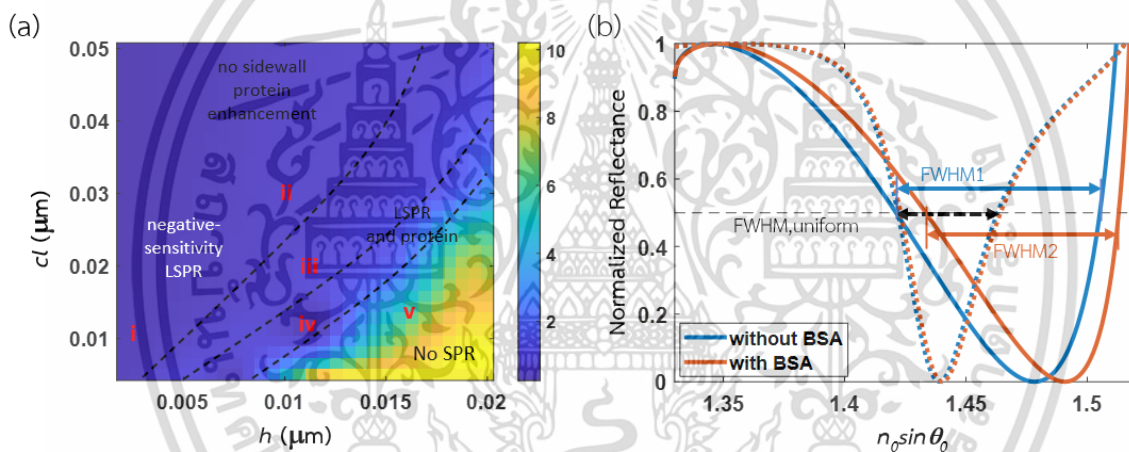


Figure 4.7 Shows the average *FWHM* of SPR responses from BSA with no sidewall and BSA with sidewall models at different roughness levels [106].

#### 4.3.5 Rough SPR-based Sensor: Intensity Contrast

The average  $\Delta I$  of the BSA with no sidewall model and BSA with sidewall model was computed using Equation (2.35) at the investigated roughness range, as shown in Figure 4.8. It is seen that the parameter crucially degraded as the roughness increased due to the LSPR effect from roughness. The operating surface "iv", for instance, had the  $\Delta I$  of 0.089, which was approximately 10 times less than the  $\Delta I$  achieved by an ideal smooth sensor. In addition, according to Figures 4.5c to 4.5e, additional protein can slightly increase the parameter.

เอกสารนี้เป็นเอกสารที่สงวนไว้สำหรับการใช้งานเพื่อการศึกษาเท่านั้น ไม่อนุญาตให้นำไปใช้ประโยชน์ด้านการค้า  
ไม่ว่ากรณีใดๆ ทั้งสิ้น อีกทั้งห้ามมิให้ดัดแปลงเนื้อหา และต้องอ้างอิงถึงเจ้าของเอกสารทุกครั้งที่มีการนำไปใช้

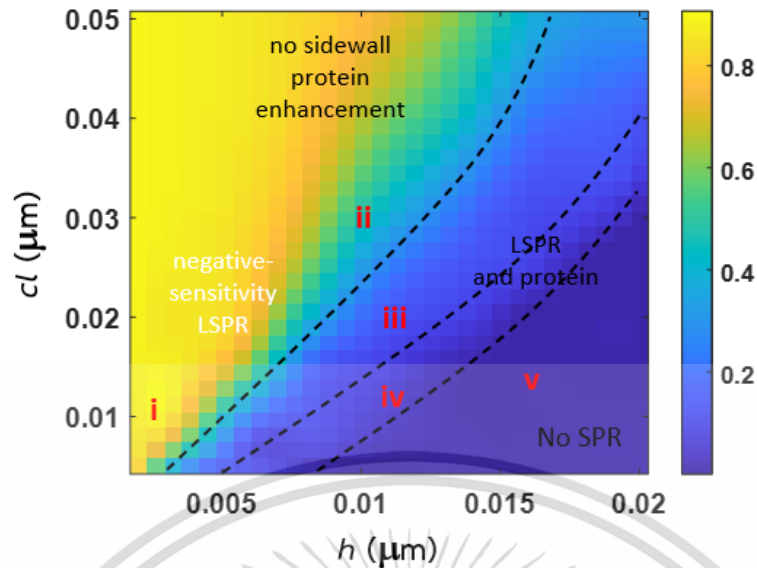


Figure 4.8 Shows the average  $\Delta I$  of SPR-based sensor outputs simulated based on BSA with no sidewall and BSA with sidewall models [106].

#### 4.3.6 Rough SPR-based Sensor: Plasmonic Intensity

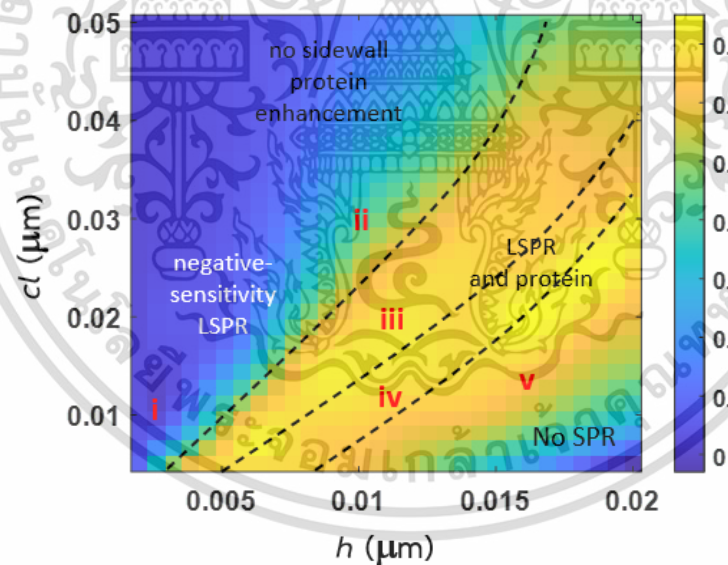


Figure 4.9 Shows the average  $I_{sp}$  of SPR-based sensor responses obtained from BSA with no sidewall and BSA with sidewall models [106].

Figure 4.9 indicates the average  $I_{sp}$  obtained from the inspected roughness levels, calculated using Equation (2.36). The parameter had a similar effect to  $\Delta I$ . Even though the presence of sidewall protein slightly reduced the  $I_{sp}$ , the LSPR effect significantly increased  $I_{sp}$  which strongly degrades the sensor's performance. At the operating surface

เอกสารนี้เป็นเอกสารที่สงวนไว้สำหรับการใช้งานเพื่อการศึกษาเท่านั้น ไม่นิยมนำไปใช้ประโยชน์ด้านการค้า  
ไม่ว่ากรณีใดๆ ทั้งสิ้น อีกทั้งห้ามมิให้ดัดแปลงเนื้อหา และต้องอ้างอิงถึงเจ้าของเอกสารทุกครั้งที่มีการนำไปใช้

“iii”, the  $I_{SP}$  crucially rose to 0.70 for the sidewall-BSA model, which was 100 times more than the theoretical limit.

#### 4.3.7 Rough SPR-based Sensor: Figure of Merits

The mentioned quantitative performance parameters were combined to determine the sensor’s overall performance, measured as the figure of merit. According to Figure 4.10, the roughness significantly affects both  $FOM_0$  and  $FOM_{SPR}$ . Firstly, the  $FOM_0$  for the BSA with no sidewall model and the BSA with sidewall model was calculated using Equation (2.37) at the roughness range, as illustrated in Figures 4.10a and 4.10b, respectively. Since the change in the  $FWHM$  was relatively small, the  $FOM_0$  mainly relies on sensitivity. Among the chosen operating surfaces, operating surface “iv” achieved the highest  $FOM_0$  of 1777.80 and 2400.02 for the non-sidewall BSA and BSA models, respectively. These values were over 5.94 times the ideal uniform sensor’s  $FOM_0$ .

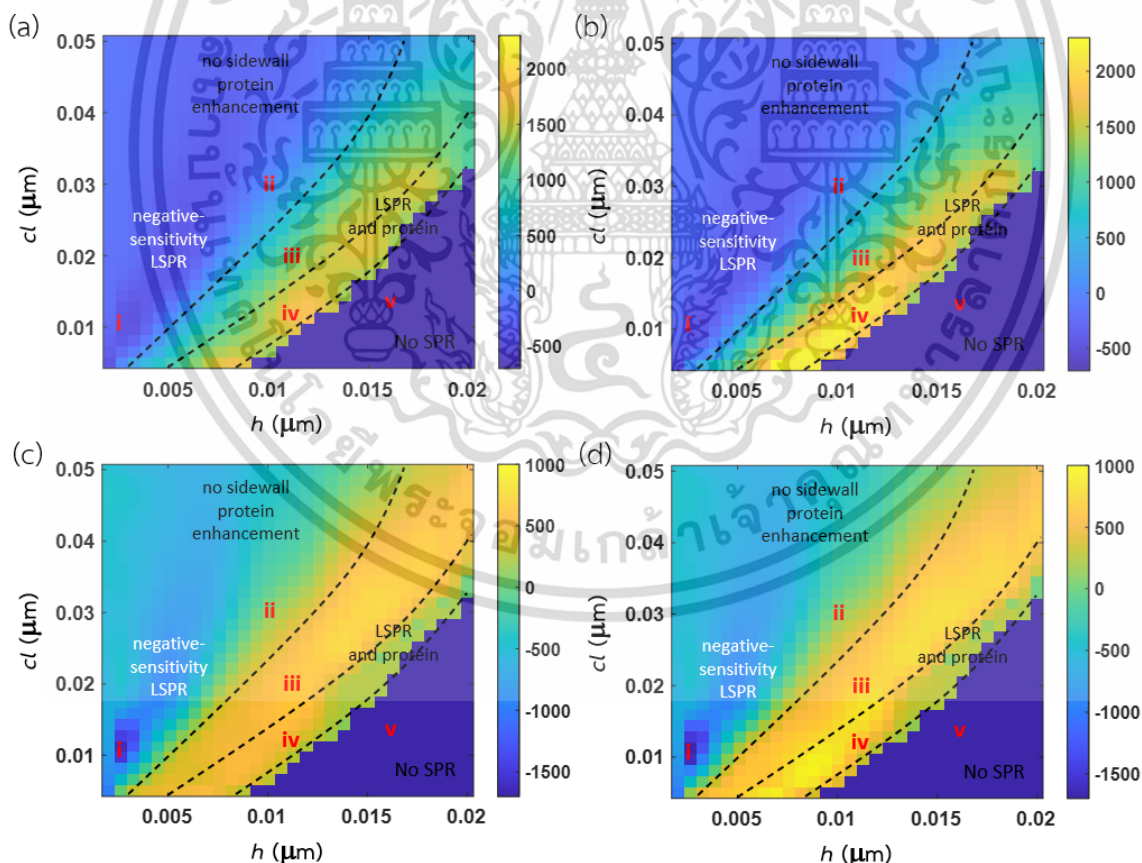


Figure 4.10 Shows the (a)  $FOM_0$  for the BSA with no sidewall model and (b) the BSA with a sidewall model, and (c) the  $FOM_{SPR}$  for the BSA with no sidewall model and (d) the BSA with sidewall model in different roughness levels [106].

เอกสารนี้เป็นเอกสารที่สงวนไว้สำหรับการใช้งานเพื่อการศึกษาเท่านั้น ไม่อนุญาตให้นำไปใช้ประโยชน์ด้านการค้า ไม่ว่าจะกรณีใดๆ ทั้งสิ้น อีกทั้งห้ามมิให้ดัดแปลงเนื้อหา และต้องอ้างอิงถึงเจ้าของเอกสารทุกครั้งที่มีการนำไปใช้

The  $FOM_{SPR}$  shows slightly different outcomes, as illustrated in Figures 4.10c and 4.10d. However, for the operating surfaces “iii” and “iv”, where the  $FOM_0$  was substantially enhanced, their  $FOM_{SPR}$  were not significantly increased. The operating surface “i”, on the other hand, had preserved  $FWHM$ ,  $\Delta I$ , and  $I_{sp}$  despite its negative sensitivity. As a result, the  $FOM_{SPR}$  of -1677.42 was achieved, which was 1.71 times improved in magnitude. This analysis indicates that negative sensitivity detection can potentially perform SPR applications. In conclusion, roughness can enhance the overall performance of the SPR-based sensor by providing an LSPR wave effect and the additional surface area for protein binding. Nevertheless, a more demanding numerical aperture (NA) must be required due to the protein increment.

#### 4.3.8 Performances of Operating Surfaces and Their EDRs

Table 4.1 summarizes all quantitative performance parameters, including  $\theta_{sp}$ , sensitivity,  $FWHM$ ,  $\Delta I$ ,  $I_{sp}$ ,  $FOM_0$ , and  $FOM_{SPR}$  for the five mentioned operating surfaces. The investigation illustrated that the presence of roughness could impact the sensing performance as a degradation effect (operating surface “ii”), enhancement effect (operating surfaces “iii” and “iv”), or deterioration effect (operating surface “v”). Moreover, there is a crucial trade-off between the sensitivity enhancement due to roughness (LSPR and protein increment) and significant degradation in  $FWHM$ ,  $\Delta I$ , and  $I_{sp}$ . A negative sensitivity detection scheme (operating surface “i”), where sensitivity was slightly increased and other performance parameters were maintained, can be employed to overcome this limitation.

The binding sensitivity,  $FOM_0$ , and  $FOM_{SPR}$  of the four operating surfaces were analyzed for the EDR ratio, calculated using Equations (3.1) to (3.3) and as depicted in Table 4.2. Here, the operating surface “v” was not mentioned due to the deteriorated sensing property. For the operating surfaces “i” and “ii”, the sidewall protein did not significantly affect the change in the performance parameters. Thus, the  $EDR_{total}$  values for these points were equal to their  $EDR_{LSPR}$ , while the  $EDR_{protein}$  was zero. Some EDRs in the investigated surface had a value of less than one. In this regard, the sensor experienced a degradation effect in sensitivity or figure of merits. On the other hand, the presence of sidewall protein crucially affected the change in the sensor’s performance for the operating surfaces “iii” and “iv”.

เอกสารนี้เป็นเอกสารที่สงวนไว้สำหรับการใช้งานเพื่อการศึกษาเท่านั้น ไม่อนุญาตให้นำไปใช้ประโยชน์ด้านการค้า  
ไม่ว่ากรณีใดๆ ทั้งสิ้น อีกทั้งห้ามมิให้ดัดแปลงเนื้อหา และต้องอ้างอิงถึงเจ้าของเอกสารทุกครั้งที่มีการนำไปใช้

Table 4.2 Shows the lists of performance parameters obtained from the five purposed operating surfaces.

Quantitative Performance Parameters	Uniform Surface Sensor	Operating Surface “i” (h of 3 nm, cl of 10 nm)		Operating Surface “ii” (h of 10 nm, cl of 30 nm)		Operating Surface “iii” (h of 12 nm, cl of 20 nm)	
		non-sidewall BSA	sidewall BSA	non-sidewall BSA	sidewall BSA	non-sidewall BSA	sidewall BSA
$\theta_{sp}$ (°)	71.33	76.99	76.99	82.22	82.22	79.59	79.80
Sensitivity (rad/ $\mu\text{m}^2$ )	122.59	-379.88	-379.88	85.31	85.31	996.11	1280.00
$FWHM$ (rad $\cdot$ RIU/ $\mu\text{m}$ )	0.41	0.58	0.58	0.79	0.79	0.66	0.65
$\Delta I$ (unitless)	0.90	0.88	0.88	0.47	0.47	0.13	0.15
$I_{sp}$ (unitless)	0.007	-0.018	0.018	0.41	-0.41	0.72	0.70
$FOM_0$ (unitless)	299.00	-654.97	-654.97	107.98	107.98	1509.26	1969.23
$FOM_{SPR}$ (unitless)	980.66	-1677.42	-1677.42	92.52	92.52	590.75	833.81
Quantitative Performance Parameters	Uniform Surface Sensor	Operating Surface “iv” (h of 9 nm, cl of 8 nm)		Operating Surface “v” (h of 16 nm, cl of 15 nm)			
		non-sidewall BSA	sidewall BSA	non-sidewall BSA	sidewall BSA		
$\theta_{sp}$ (°)	71.33	77.86	78.60	74.68 *	75.71 *		
Sensitivity (rad/ $\mu\text{m}^2$ )	122.59	1191.13	1608.02	-	-		
$FWHM$ (rad $\cdot$ RIU/ $\mu\text{m}$ )	0.41	0.67	0.67	0.77	0.75		
$\Delta I$ (unitless)	0.90	0.10	0.14	0.001	0.003		
$I_{sp}$ (unitless)	0.007	0.69	0.60	0.75	0.69		
$FOM_0$ (unitless)	299.00	1777.80	2400.02	-	-		
$FOM_{SPR}$ (unitless)	980.66	616.84	1020.33	-	-		

เอกสารนี้เป็นเอกสารที่สงวนไว้สำหรับการใช้งานเพื่อการศึกษาเท่านั้น ไม่อนุญาตให้นำไปใช้ประโยชน์ด้านการค้า  
ไม่ว่ากรณีใดๆ ทั้งสิ้น อีกทั้งห้ามมิให้ดัดแปลงเนื้อหา และต้องอ้างอิงถึงเจ้าของเอกสารทุกครั้งที่มีการนำไปใช้

Table 4.3 Shows the  $EDR$  for different operating surfaces and its quantification for  $EDR_{LSPR}$  and  $EDR_{protein}$ .

	Operating Surface "i" (h of 3 nm, cl of 10 nm)	Operating Surface "ii" (h of 10 nm, cl of 30 nm)	Operating Surface "iii" (h of 12 nm, cl of 20 nm)	Operating Surface "iv" (h of 9 nm, cl of 8 nm)
$EDR_{LSPR,S}$	-3.10	0.70	10.44	13.12
$EDR_{protein,S}$	-3.10 (100%)	0.70 (100%)	8.13 (77.87%)	9.72 (74.07%)
$EDR_{total,S}$	0 (0%)	0 (0%)	2.31 (22.13%)	3.40 (25.93%)
$EDR_{LSPR,FOM0}$	-2.19	0.36	6.59	8.03
$EDR_{protein,FOM0}$	-2.19 (100%)	0.36 (100%)	5.05 (76.64%)	5.95 (74.07%)
$EDR_{total,FOM0}$	0 (0%)	0 (0%)	1.54 (23.36%)	2.08 (25.93%)
$EDR_{LSPR,FOMSPR}$	-1.71	0.09	0.85	1.04
$EDR_{protein,FOMSPR}$	-1.71 (100%)	0.09 (100%)	0.60 (70.85%)	0.63 (60.45%)
$EDR_{total,FOMSPR}$	0 (0%)	0 (0%)	0.25 (29.15%)	0.41 (39.55%)

#### 4.3.9 Linearity Test

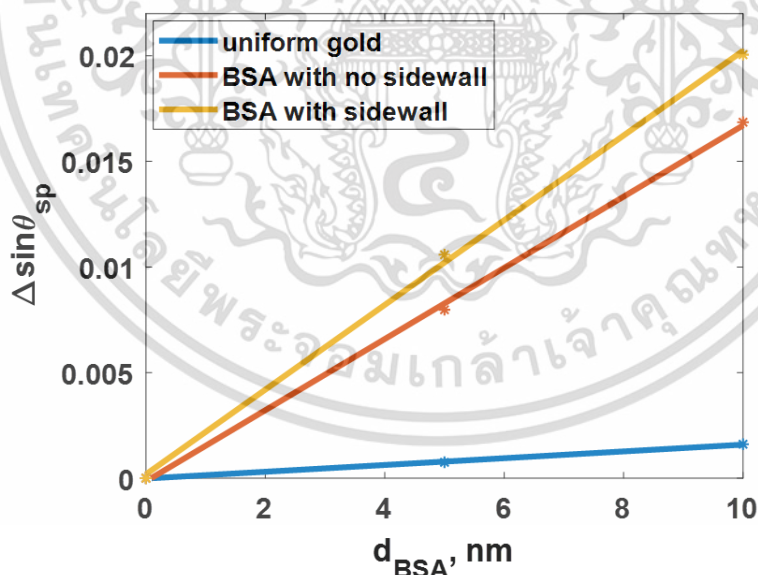


Figure 4.11 Shows the linearity test of sensitivity and varying the BSA thickness for the ideal uniform gold model, the BSA with no sidewall model, and the BSA with sidewall model with roughness employed as the operating surface "iv" [106].

เอกสารนี้เป็นเอกสารที่สงวนไว้สำหรับการใช้งานเพื่อการศึกษาเท่านั้น ไม่อนุญาตให้นำไปใช้ประโยชน์ด้านการค้า  
ไม่ว่ากรณีใดๆ ทั้งสิ้น อีกทั้งห้ามมิให้ดัดแปลงเนื้อหา และต้องอ้างอิงถึงเจ้าของเอกสารทุกครั้งที่มีการนำไปใช้

One crucial characteristic of the kinetic binding application for SPR detection was establishing a linear sensitivity response and protein concentration-response. The linearity test was investigated based on three models: uniform gold (blue), non-sidewall BSA (red), and sidewall BSA (yellow), as illustrated in Figure 4.11. Note that the rough surface was employed as the operating surface “iv” due to the highest  $FOM_0$  and  $FOM_{SPR}$  achieved. The sensitivity, measured as  $\Delta \sin \theta_{sp}$ , was measured for a BSA binding layer with a thickness ranging from 0 (no BSA) to 10 nm. The R-square values achieved by the ideal uniform gold, the non-sidewall BSA model, and the sidewall BSA model were 0.9985, 0.9990, and 0.9990, respectively. The slopes were also calculated for the three models: the theoretical smooth surface, non-sidewall BSA, and sidewall BSA achieved slopes of  $8.13 \times 10^{-4}$ ,  $1.69 \times 10^{-3}$ , and  $2.01 \times 10^{-3}$ , respectively. The sensitivity at the BSA thickness of 5 nm agrees well with the inspected values earlier. Therefore, the presented model can provide SPR detection with linear responses for the BSA layer with a thickness of up to 10 nm.

## CHAPTER 5

### DISCUSSION

#### 5.1 The LSPR Effect and Sidewall Protein Increment

According to Table 4.2, the primary effect on the SPR detection was the LSPR with  $EDR_{LSPR}$  of over 70% for sensitivity and fom0. The  $EDR_{protein}$  was very close to the percent increase of protein amount shown in Figure 4.6. This correlation indicates that the presence of additional protein increased the sensitivity of SPR detection proportionally. Furthermore, the  $FOM_{SPR}$  had a slightly greater  $EDR_{protein}$  with the maximum of 39.55% at the operating surface “iv” due to the reduction of the  $I_{sp}$  and increased the  $\Delta I$  due to the sidewall protein.

In this investigation, the detection mechanism of SPR on rough surfaces has been explained and provided. According to Chapter 4, it was observed that the presence of rough surfaces tremendously increased the sensitivity and  $FOM_0$  in exchange for a crucial degradation of  $FWHM$  and intensity-related parameters. Furthermore, the roughness provides a single SPR mode from a scattering effect of the SPPs [111], unlike the gratings structure, which could provide two or three SPR dips in a detection [112]. In other words, an average effect of the scattered SPPs and LSPR hotspots at sharp edges was achieved with a rough SPR-based sensor. Nevertheless, one significant drawback of a sensor with a rough surface is that there is no repeatability in the manufactured sensor. Unlike gratings SPR-based sensors, the surface profiles always differ after each fabrication. In addition, due to the randomly scattered SPPs in rough surfaces, it might not be suitable for optical imaging applications.

#### 5.2 Intensity and Phase Detection

In addition to angular interrogation, SPR measurements can be performed using the wavelength scanning method via intensity and phase detection, as in the angular interrogation studied in this investigation. Moreover, scanning wavelengths and angles does not affect these schemes. Figure 5.1 depicts the intensity and phase detection performances of the five discussed operation surfaces and the theoretical uniform surface sensor. Figure 5.1a illustrates that the roughness profiles can produce a greater optical intensity contrast than the theoretically smooth plasmonic layer case. For example, the

ไม่ว่ากรณีใดๆ ทั้งสิ้น อีกทั้งห้ามมิให้ตัดแปลงเนื้อหา และต้องอ้างอิงถึงเจ้าของเอกสารทุกครั้งที่มีการนำไปใช้

operating surface 'ii', which has a very low sensitivity, can significantly change the plasmonic intensity of 0.27. In addition, operating surface 'i', which yielded a negative sensitivity, has crucially improved both intensity and phase detection, as shown in Figures 5.1a and 51b, respectively. According to the observations, the negative sensitivity measurement of SPR with a rough surface is a potential target for monitoring binding kinetics.

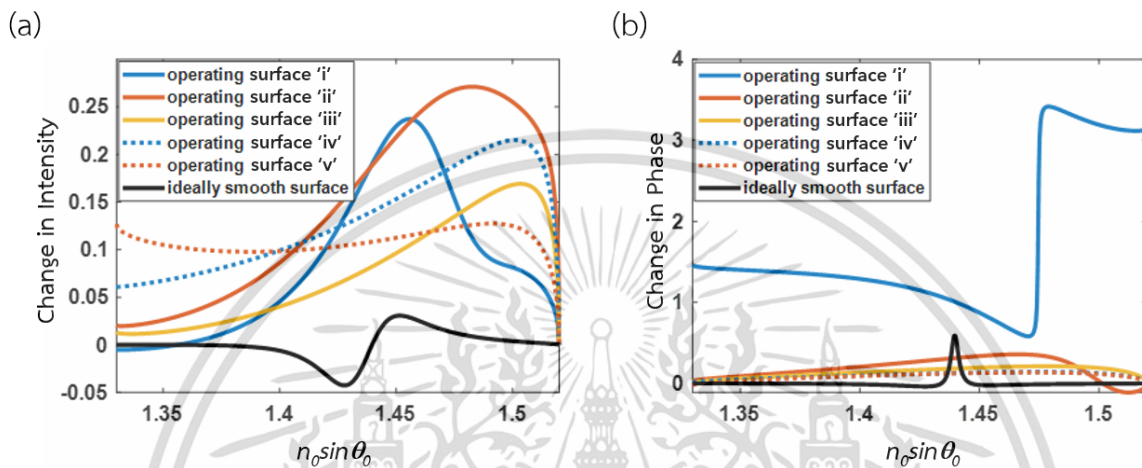


Figure 5.1 Shows the results for (a) intensity detection and (b) phase detection for the purposed operating surfaces [106].

### 5.3 Field Plots of SPR-based Sensor Structures

Light consists of electric and magnetic fields, and this characteristic of the electromagnetic waves was used to explain why the performance of the rough SPR-based sensor was significantly improved. Polarization can excite SPR effects in TM-polarized light only, or the electric field will influence the metallic surface along the x and z axis, with no magnetic fields in the dimensions. The total electric field intensity along the x-axis ( $|\mathbf{E}_x|^2$ ) and z-axis ( $|\mathbf{E}_z|^2$ ) is an excellent indicator for the sum of the LSPR strengths across the surface.

Figure 5.2 indicates the total electric field intensity in the SI unit,  $|\mathbf{E}_x|^2 + |\mathbf{E}_z|^2$ , in three different SPR-based sensor surfaces: a theoretical uniform gold layer, a gold gratings structure, and a rough gold film for the TM-polarization case in the x and z coordinates. The electric field intensity was evenly distributed along the gold surface for the uniform SPR-based sensor, with a maximum magnitude of  $11.28 \times 10^3$ , as shown in Figure 5.2a. The total power of the electric field for an SPR-based sensor with the gratings structure, on the other hand, can reach up to  $16.08 \times 10^5$ , which was a hundred times

เอกสารนี้เป็นเอกสารที่สงวนไว้สำหรับการใช้งานเพื่อการศึกษาเท่านั้น ไม่อนุญาตให้นำไปใช้ประโยชน์ด้านการค้า  
ไม่ว่ากรณีใดๆ ทั้งสิ้น อีกทั้งห้ามมิให้ดัดแปลงเนื้อหา และต้องอ้างอิงถึงเจ้าของเอกสารทุกครั้งที่มีการนำไปใช้

stronger than the field intensity of the value achieved by the smooth theoretical sensor. The colour scales in Figures 5.2b and 5.2c have been adjusted to clearly illustrate the intensity of the electric field across the entire surface (their maximum values exceed the provided colour bar limit). The height, period, and fill factor of the gratings of 24 nm, 500 nm, and 0.5 were chosen based on the rough surface model analysis.

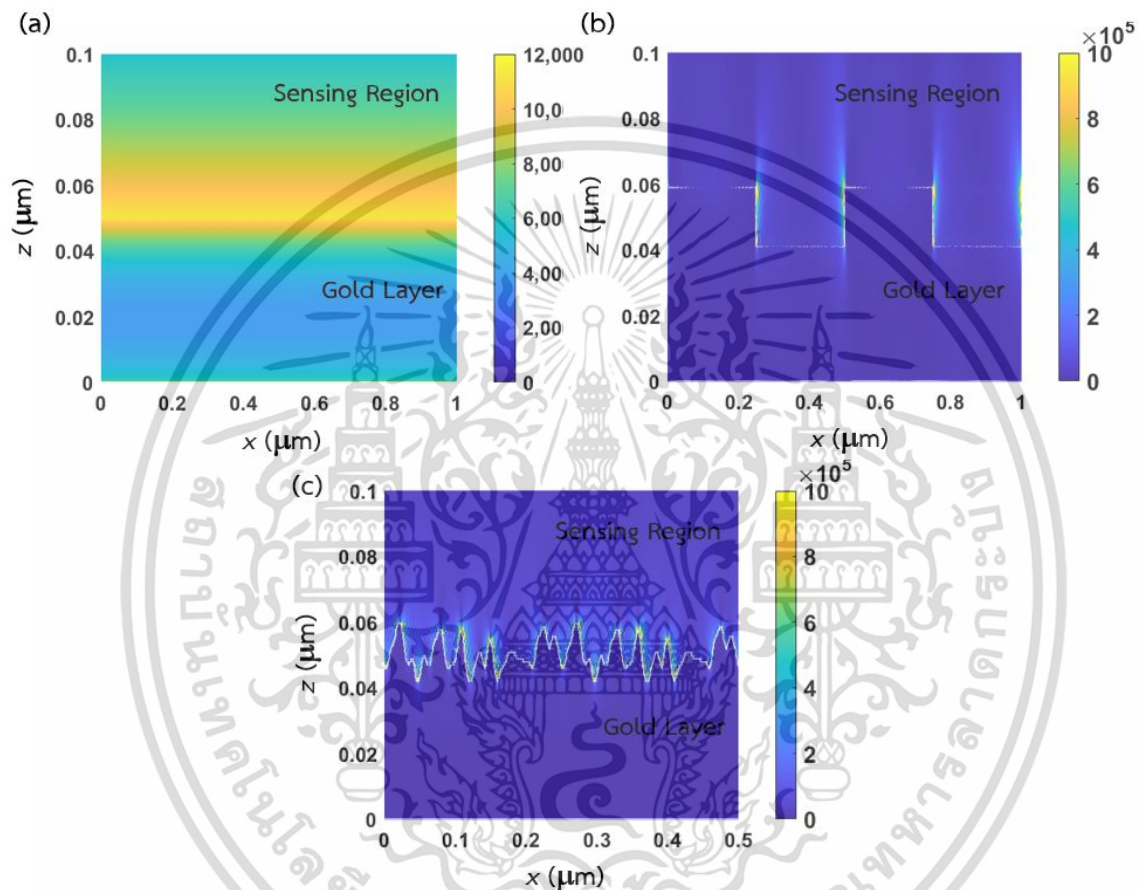


**Figure 5.2** Shows the intensity of electric fields represent as  $|E_x|^2 + |E_z|^2$  for (a) the ideal uniform surface sensor, (c) the SPR-based sensor with gratings structure, and (c) the SPR-based sensor with roughness as  $h$  of 9 nm and  $cl$  of 8 nm (operating point “iv”)

[106].

In addition, the crucially high intensity of the electric field appears only on the sharp edges of the gratings, whereas the groove area's intensity ranges from  $6.00 \times 10^3$  to  $30.00 \times 10^3$ . Due to the highest achieved figure of merits, the rough surface in the operating surface 'iv' ( $h$  of 9 nm and  $cl$  of 8 nm) was chosen to study the electric field behaviour. The maximum electric field intensity acquired can vary between  $14.92 \times 10^5$  and  $17.51 \times 10^5$ , depending on the randomly simulated surface. Despite the generated electric field

เอ็กสักรีนเป็นเอกสารที่สงวนลิขสิทธิ์ไว้เพื่อการศึกษาเท่านั้น ไม่อนุญาตให้เผยแพร่เชิงพาณิชย์ การค้า  
 ไม่ว่าจะกรณีใดๆ ทั้งสิ้น อีกทั้งห้ามมิให้ดัดแปลงเนื้อหา และต้องอ้างอิงถึงเจ้าของเอกสารทุกครั้งที่มีการนำไปใช้

intensities of the gratings and rough surfaces, the roughness model produced more sharp edges, leading to more LSPR hotspots and increased sensitivity.



เอกสารนี้เป็นเอกสารที่สงวนไว้สำหรับการใช้งานเพื่อการศึกษาเท่านั้น ไม่อนุญาตให้นำไปใช้ประโยชน์ด้านการค้า  
ไม่ว่ากรณีใดๆ ทั้งสิ้น อีกทั้งห้ามมิให้ดัดแปลงเนื้อหา และต้องอ้างอิงถึงเจ้าของเอกสารทุกครั้งที่มีการนำไปใช้

## CHAPTER 6

# CONCLUSION

The SPR-based sensor was sensitive to alterations in the plasmonic sensor surface. As a result, even minor changes in the surface morphology, such as roughness, can significantly impact the sensor's performance. This study investigates the impact of roughness on binding kinetic measurement for SPR detection using the RCWA and Monte Carlo simulation on a rough surface constructed based on the Gaussian random surfaces technique. The simulation relies on two main models: the BSA with no sidewall model, which indicated the same amount of protein as the roughness changed, and the BSA with the sidewall model, which indicated an increase in protein quantity as the roughness increased. A convergence test on the number of required diffraction orders and simulated columns to represent roughness and the SPR phenomenon were also utilised to obtain the optimal environment for the theoretical study. Afterwards, the calculated reflectance spectra were examined. The performance factors, including plasmonic angle, sensitivity, *FWHM*,  $\Delta I$ ,  $I_{sp}$ , and the figure of merits were then calculated and analyzed.

The generated LSPR and the additional protein amount cause the surface roughness to either enhance, degrade, or deteriorate the SPR sensing performance. Because of the distorted plasmonic dip structure, which reduced the plasmonic angle and field enhancement effect from the surface roughness, the sensor can have a crucially high sensitivity at a highly rough surface. However, using the rough surface results in a trade-off relationship between enhanced sensitivity, a significant decrease in intensity detection capability, and *FWHM* degradation. One approach suggested for the SPR application is to use negative-sensitivity SPR detection at low roughness levels. The reflectance spectra obtained from this region can triple the *S* of an ideal uniform gold sensor while preserving the *FWHM*,  $\Delta I$ , and  $I_{sp}$ . When compared to the sensor with a theoretically smooth surface, the operating points with the highest  $FOM_0$  and  $FOM_{SPR}$  increased the figure of merits by 8.03 and 1.04 times, respectively. The roughness level could also be used in other SPR measurement schemes, such as intensity and phase detection. Further investigation reveals that the LSPR effect of more than 70% influenced sensing

เอกสารนี้เป็นเอกสารที่สงวนไว้สำหรับการใช้งานเพื่อการศึกษาเท่านั้น ไม่อนุญาตให้นำไปใช้ประโยชน์ด้านการค้า  
ไม่ว่ากรณีใดๆ ทั้งสิ้น อีกทั้งห้ามมิให้ดัดแปลงเนื้อหา และต้องอ้างอิงถึงเจ้าของเอกสารทุกครั้งที่มีการนำไปใช้

improvement and degradation in most operating surfaces. Finally, knowledge of surface roughness can be used to improve the SPR-based sensor's protein binding sensing performance.

Finally, the investigation was published in the MDPI Sensors journal titled "Sensing Mechanisms of Rough Plasmonic Surfaces for Protein Binding of Surface Plasmon Resonance Detection" [106].



เอกสารนี้เป็นเอกสารที่สงวนไว้สำหรับการใช้งานเพื่อการศึกษาเท่านั้น ไม่อนุญาตให้นำไปใช้ประโยชน์ด้านการค้า  
ไม่ว่ากรณีใดๆ ทั้งสิ้น อีกทั้งห้ามมิให้ดัดแปลงเนื้อหา และต้องอ้างอิงถึงเจ้าของเอกสารทุกครั้งที่มีการนำไปใช้

## REFERENCES

- [1] Brongersma, M.L.; Kik, P.G. *Surface Plasmon Nanophotonics*; Springer: Dordrecht, the Netherlands, **2007**; Volume 131.
- [2] Somekh, M.G.; Pechprasarn, S. Surface plasmon, surface wave, and enhanced evanescent wave microscopy. In *Handbook of Photonics for Biomedical Engineering*; Springer: Dordrecht, the Netherlands: **2017**; pp. 503–543.
- [3] Homola, J.; Yee, S.S.; Gauglitz, G. Surface plasmon resonance sensors. *Sens. Actuators B Chem.* **1999**, *54*, 3–15.
- [4] Suda, Y.; Arano, A.; Fukui, Y.; Koshida, S.; Wakao, M.; Nishimura, T.; Kusumoto, S.; Sobel, M. Immobilization and clustering of structurally defined oligosaccharides for sugar chips: An improved method for surface plasmon resonance analysis of protein–carbohydrate interactions. *Bioconjugate Chem.* **2006**, *17*, 1125–1135.
- [5] Mariani, S.; Minunni, M. Surface plasmon resonance applications in clinical analysis. *Anal. Bioanal. Chem.* **2014**, *406*, 2303–2323.
- [6] Chen, J.; Park, B. Label-free screening of foodborne *Salmonella* using surface plasmon resonance imaging. *Anal. Bioanal. Chem.* **2018**, *410*, 5455–5464.
- [7] Douzi, B. Protein–protein interactions: Surface plasmon resonance. In *Bacterial Protein Secretion Systems: Methods and Protocols*; Humana Press: New York, NY, USA, **2017**; pp. 257–275.
- [8] Drescher, D.G.; Selvakumar, D.; Drescher, M.J. Analysis of protein interactions by surface plasmon resonance. *Adv. Protein Chem. Struct. Biol.* **2018**, *110*, 1–30.
- [9] Shen, M.; Learkthanakhachon, S.; Pechprasarn, S.; Zhang, Y.; Somekh, M.G. Adjustable microscopic measurement of nanogap waveguide and plasmonic structures. *Appl. Opt.* **2018**, *57*, 3453–3462.
- [10] Suvarnaphaet, P.; Pechprasarn, S. Enhancement of long-range surface plasmon excitation, dynamic range and figure of merit using a dielectric resonant cavity. *Sensors* **2018**, *18*, 2757.
- [11] de Mol, N.J.; Dekker, F.J.; Broutin, I.; Fischer, M.J.; Liskamp, R.M. Surface plasmon resonance thermodynamic and kinetic analysis as a strategic tool in drug design. Distinct ways for phosphopeptides to plug into Src-and Grb2 SH2 domains. *J. Med. Chem.* **2005**, *48*, 753–763.
- [12] Navratilova, I.; Hopkins, A.L. Emerging role of surface plasmon resonance in fragment-based drug discovery. *Future Med. Chem.* **2011**, *3*, 1809–1820.

เอกสารนี้เป็นเอกสารที่สงวนลิขสิทธิ์ไว้เพื่อการศึกษาเท่านั้น เมื่อผู้ผู้ใดเห็นนำไปใช้ประโยชน์ด้านการค้า

ไม่ว่ากรณีใดๆ ทั้งสิ้น อีกทั้งห้ามมิให้ตัดแปลงเนื้อหา และต้องอ้างอิงถึงเจ้าของเอกสารทุกครั้งที่มีการนำไปใช้

- [13] Chow, T.W.; Pechprasarn, S.; Meng, J.; Somekh, M.G. Single shot embedded surface plasmon microscopy with vortex illumination. *Opt. Express* **2016**, *24*, 10797–10805.
- [14] Englebienne, P.; Van Hoonacker, A.; Verhas, M. Surface plasmon resonance: Principles, methods and applications in biomedical sciences. *Spectroscopy* **2003**, *17*, 255–273.
- [15] Sangworasil, M.; Pechprasarn, S.; Larkthanakhachon, S.; Ittipornnusun, K.; Suvarnaphaet, P.; Albutt, N. Investigation on feasibility of using surface plasmons resonance (SPR) sensor for ultrasonic detection: A novel optical detection of ultrasonic waves. In Proceedings of 2016 9th Biomedical Engineering International Conference (BMEiCON), Laung Prabang, Laos, 7–9 December **2016**; pp. 1–3.
- [16] Suvarnaphaet, P.; Pechprasarn, S. Quantitative cross-platform performance comparison between different detection mechanisms in surface plasmon sensors for voltage sensing. *Sensors* **2018**, *18*, 3136.
- [17] Kretschmann, E.; Raether, H. Radiative decay of non radiative surface plasmons excited by light. *Z. Nat. A* **1968**, *23*, 2135–2136.
- [18] Zeng, Y.; Zhou, J.; Wang, X.; Cai, Z.; Shao, Y. Wavelength-scanning surface plasmon resonance microscopy: A novel tool for real time sensing of cell-substrate interactions. *Biosens. Bioelectron.* **2019**, *145*, 111717.
- [19] Ran, B.; Lipson, S. Comparison between sensitivities of phase and intensity detection in surface plasmon resonance. *Opt. Express* **2006**, *14*, 5641–5650.
- [20] Kabashin, A.V.; Patskovsky, S.; Grigorenko, A.N. Phase and amplitude sensitivities in surface plasmon resonance bio and chemical sensing. *Opt. Express* **2009**, *17*, 21191–21204.
- [21] Guo, J.; Keathley, P.D.; Hastings, J. Dual-mode surface-plasmon-resonance sensors using angular interrogation. *Opt. Lett.* **2008**, *33*, 512–514.
- [22] Crowell, J.; Ritchie, R. Surface-plasmon effect in the reflectance of a metal. *JOSA* **1970**, *60*, 794–799.
- [23] Braundmeier, A., Jr.; Arakawa, E. Effect of surface roughness on surface plasmon resonance absorption. *J. Phys. Chem. Solids* **1974**, *35*, 517–520.
- [24] Rahman, T.S.; Maradudin, A.A. Surface-plasmon dispersion relation in the presence of surface roughness. *Phys. Rev. B* **1980**, *21*, 2137.
- [25] Hoffmann, A.; Lenkefi, Z.; Szentirmay, Z. Effect of roughness on surface plasmon scattering in gold films. *J. Phys. Condens. Matter* **1998**, *10*, 5503.

เอกสารนี้เป็นเอกสารที่สงวนไว้สำหรับการใช้งานเพื่อการศึกษาเท่านั้น ไม่อนุญาตให้นำไปใช้ประโยชน์ด้านการค้า  
ไม่ว่ากรณีใดๆ ทั้งสิ้น อีกทั้งห้ามมิให้ดัดแปลงเนื้อหา และต้องอ้างอิงถึงเจ้าของเอกสารทุกครั้งที่มีการนำไปใช้

- [26] Kurihara, K.; Suzuki, K. Theoretical understanding of an absorption-based surface plasmon resonance sensor based on Kretschmann's theory. *Anal. Chem.* **2002**, *74*, 696–701.
- [27] Treebupachatsakul, T.; Shinnakerdchoke, S.; Pechprasarn, S. Analysis of effects of surface roughness on sensing performance of surface plasmon resonance detection for refractive index sensing application. *Sensors* **2021**, *21*, 6164.
- [28] Byun, K.M.; Yoon, S.J.; Kim, D. Effect of surface roughness on the extinction-based localized surface plasmon resonance biosensors. *Appl. Opt.* **2008**, *47*, 5886–5892.
- [29] Liu, H.; Wang, B.; Leong, E.S.; Yang, P.; Zong, Y.; Si, G.; Teng, J.; Maier, S.A. Enhanced surface plasmon resonance on a smooth silver film with a seed growth layer. *ACS Nano* **2010**, *4*, 3139–3146.
- [30] Schug, C.; Schempp, S.; Lamparter, P.; Steeb, S. Surface roughness of sputter-deposited gold films: A combined x-ray technique and AFM study. *Surf. Interface Anal.* **1999**, *27*, 670–677.
- [31] Ng, D.K.; Bhola, B.S.; Bakker, R.M.; Ho, S.T. Ultrasoother gold films via pulsed laser deposition. *Adv. Funct. Mater.* **2011**, *21*, 2587–2592.
- [32] Diebel, J.; Löwe, H.; Samori, P.; Rabe, J. Fabrication of large-scale ultra-smooth metal surfaces by a replica technique. *Appl. Phys. A* **2001**, *73*, 273–279.
- [33] Zhang, C.; Li, J.; Belianinov, A.; Ma, Z.; Renshaw, C.K.; Gelfand, R.M. Nanoaperture fabrication in ultra-smooth single-grain gold films with helium ion beam lithography. *Nanotechnology* **2020**, *31*, 465302.
- [34] Zhang, J.; Irannejad, M.; Yavuz, M.; Cui, B. Gold nanohole array with sub-1 nm roughness by annealing for sensitivity enhancement of extraordinary optical transmission biosensor. *Nanoscale Res. Lett.* **2015**, *10*, 238.
- [35] Subrahmanyam, N. *A textbook of optics*. S. Chand Publishing, **2004**.
- [36] Nyambuya, Golden G., A. Dube, and G. Musosi. "On Newton's Corpuscular Theory of Light." *Prespacetime Journal* 8.10, **2017**.
- [37] Shirley, John W. "An early experimental determination of Snell's law." *American Journal of Physics* 19.9, **1951**: 507-508.
- [38] Parazzoli, C. G., et al. "Experimental verification and simulation of negative index of refraction using Snell's law." *Physical Review Letters* 90.10, **2003**: 107401.
- [39] Bell, Arthur Ernest. *Christian Huygens*. Read Books Ltd, **2012**.
- [40] Miller, Dayton C. "The ether-drift experiment and the determination of the absolute motion of the earth." *Reviews of modern physics* 5.3, **1933**: 203.

เอกสารนี้เป็นเอกสารที่สงวนไว้สำหรับการใช้งานเพื่อการศึกษาเท่านั้น ไม่อนุญาตให้นำไปใช้ประโยชน์ด้านการค้า  
ไม่ว่ากรณีใดๆ ทั้งสิ้น อีกทั้งห้ามมิให้ดัดแปลงเนื้อหา และต้องอ้างอิงถึงเจ้าของเอกสารทุกครั้งที่มีการนำไปใช้

- [41] Grella, Raffaele. "Fresnel propagation and diffraction and paraxial wave equation." *Journal of Optics* 13.6, **1982**: 367.
- [42] Chauvat, Dominique, et al. "Huygens' principle and Young's experiment in the propagation of light beams." *American Journal of Physics* 71.11, **2003**: 1196-1198.
- [43] Kovetz, Attay. *Electromagnetic theory*. Vol. 975. Oxford: Oxford University Press, **2000**.
- [44] Morey, Richard D., Saskia Homer, and Travis Proulx. "Beyond statistics: Accepting the null hypothesis in mature sciences." *Advances in Methods and Practices in Psychological Science* 1.2, **2018**: 245-258.
- [45] Klein, Martin J. "Max Planck and the beginnings of the quantum theory." *Archive for History of Exact Sciences* 1 (**1961**): 459-479.
- [46] Kragh, Helge. "Max Planck: the reluctant revolutionary." *Physics World* 13.12 (**2000**): 31.
- [47] Ranganath, G. S. "Black-body radiation." *Resonance* 13.2 (**2008**): 115-133.
- [48] Pais, Abraham. "Einstein and the quantum theory." *Reviews of modern physics* 51.4 (**1979**): 863.
- [49] Klassen, Stephen. "The photoelectric effect: Reconstructing the story for the physics classroom." *Science & Education* 20 (**2011**): 719-731.
- [50] Evans, Robley D. *Compton effect*. Springer Berlin Heidelberg, **1958**.
- [51] Weinstein, L. A. "Electromagnetic waves." *Radio i svyaz', Moscow* (**1988**).
- [52] Smith, Glenn S. *An introduction to classical electromagnetic radiation*. Cambridge University Press, **1997**.
- [53] Oen, Ordean S., and Mark T. Robinson. "Computer studies of the reflection of light ions from solids." *Nuclear instruments and Methods* 132 (**1976**): 647-653.
- [54] Kortüm, Gustav, and Gustav Kortüm. "Regular and diffuse reflection." *Reflectance Spectroscopy: Principles, Methods, Applications* (**1969**): 5-71.
- [55] Donnat, Phillipe, and Jeffrey Rauch. "Modeling the dispersion of light." *Singularities and Oscillations*. Springer New York, **1997**.
- [56] Wolf, Emil. *Introduction to the Theory of Coherence and Polarization of Light*. Cambridge university press, **2007**.
- [57] Svirko, Yu P., and Nikolay I. Zheludev. *Polarization of light in nonlinear optics*. **2000**.
- [58] Rosales-Guzmán, Carmelo, Bienvenu Ndagano, and Andrew Forbes. "A review of complex vector light fields and their applications." *Journal of Optics* 20.12 (**2018**): 123001.

เอกสารนี้เป็นเอกสารที่สงวนไว้สำหรับการใช้งานเพื่อการศึกษาเท่านั้น ไม่อนุญาตให้นำไปใช้ประโยชน์ด้านการค้า  
ไม่ว่ากรณีใดๆ ทั้งสิ้น อีกทั้งห้ามมิให้ดัดแปลงเนื้อหา และต้องอ้างอิงถึงเจ้าของเอกสารทุกครั้งที่มีการนำไปใช้

- [59] Xiong, Hao, et al. "Optical polarizer based on the mechanical effect of light." *Optics Letters* 41.18 (2016): 4316-4319.
- [60] Schwartz, Brian T., and Rafael Piestun. "Total external reflection from metamaterials with ultralow refractive index." *JOSA B* 20.12 (2003): 2448-2453.
- [61] Axelrod, Daniel, Thomas P. Burghardt, and Nancy L. Thompson. "Total internal reflection fluorescence." *Annual review of biophysics and bioengineering* 13.1 (1984): 247-268.
- [62] Axelrod, Daniel, Thomas P. Burghardt, and Nancy L. Thompson. "Total internal reflection fluorescence." *Annual review of biophysics and bioengineering* 13.1 (1984): 247-268.
- [63] Yin, Xiaobo, and Lambertus Hesselink. "Goos-Hänchen shift surface plasmon resonance sensor." *Applied physics letters* 89.26 (2006): 261108.
- [64] Renard, Rémi H. "Total reflection: a new evaluation of the Goos-Hänchen shift." *JOSA* 54.10 (1964): 1190-1197.
- [65] Snyder, Allan W., and John D. Love. "Goos-Hänchen shift." *Applied optics* 15.1 (1976): 236-238.
- [66] Fish, Kenneth N. "Total internal reflection fluorescence (TIRF) microscopy." *Current protocols in cytometry* 50.1 (2009): 12-18.
- [67] Mattheyses, Alexa L., Sanford M. Simon, and Joshua Z. Rappoport. "Imaging with total internal reflection fluorescence microscopy for the cell biologist." *Journal of cell science* 123.21 (2010): 3621-3628.
- [68] Lok, Brent K., Yu-Ling Cheng, and Channing R. Robertson. "Total internal reflection fluorescence: a technique for examining interactions of macromolecules with solid surfaces." *Journal of Colloid and Interface Science* 91.1 (1983): 87-103.
- [69] Axelrod, Daniel. "Total internal reflection fluorescence microscopy in cell biology." *Traffic* 2.11 (2001): 764-774.
- [70] Harrick, N. J. "Surface chemistry from spectral analysis of totally internally reflected radiation." *The Journal of Physical Chemistry* 64.9 (1960): 1110-1114.
- [71] Harrick, N. J. "Study of physics and chemistry of surfaces from frustrated total internal reflections." *Physical Review Letters* 4.5 (1960): 224.
- [72] Schasfoort, Richard BM, ed. *Handbook of surface plasmon resonance*. Royal Society of Chemistry, 2017.
- [73] Kawata, Satoshi, Motoichi Ohtsu, and Masahiro Irie, eds. *Near-field optics and surface plasmon polaritons*. Vol. 81. Springer Science & Business Media, 2001.

เอกสารนี้เป็นเอกสารที่สงวนไว้สำหรับการใช้งานเพื่อการศึกษาเท่านั้น ไม่อนุญาตให้นำไปใช้ประโยชน์ด้านการค้า  
ไม่ว่ากรณีใดๆ ทั้งสิ้น อีกทั้งห้ามมิให้ดัดแปลงเนื้อหา และต้องอ้างอิงถึงเจ้าของเอกสารทุกครั้งที่มีการนำไปใช้

- [74] Hutter, Eliza, and Janos H. Fendler. "Exploitation of localized surface plasmon resonance." *Advanced materials* 16.19 (2004): 1685-1706.
- [75] Pitarke, J. M., et al. "Theory of surface plasmons and surface-plasmon polaritons." *Reports on progress in physics* 70.1 (2006): 1.
- [76] Lvovsky, Alexander I. "Fresnel equations." *Encyclopedia of Optical and Photonic Engineering (Print)-Five Volume Set*. CRC Press, 2015. 1-6.
- [77] Hénon, S., and J. Meunier. "Microscope at the Brewster angle: Direct observation of first-order phase transitions in monolayers." *Review of Scientific Instruments* 62.4 (1991): 936-939.
- [78] Hoenig, Dirk, and Dietmar Moebius. "Direct visualization of monolayers at the air-water interface by Brewster angle microscopy." *The Journal of Physical Chemistry* 95.12 (1991): 4590-4592.
- [79] Fahrenfort, J. "Attenuated total reflection: A new principle for the production of useful infra-red reflection spectra of organic compounds." *Spectrochimica Acta* 17.7 (1961): 698-709.
- [80] Dawson, Paul, B. A. F. Puygranier, and J. P. Goudonnet. "Surface plasmon polariton propagation length: A direct comparison using photon scanning tunneling microscopy and attenuated total reflection." *Physical Review B* 63.20 (2001): 205410.
- [81] Akowuah, Emmanuel K., Terry Gorman, and Shyqyri Haxha. "Design and optimization of a novel surface plasmon resonance biosensor based on Otto configuration." *Optics express* 17.26 (2009): 23511-23521.
- [82] Bowles, Mark R., et al. "Studies of protein interactions by biosensor technology: an alternative approach to the analysis of sensorgrams deviating from pseudo-first-order kinetic behavior." *Analytical biochemistry* 244.1 (1997): 133-143.
- [83] Mohamed, Shaimaa K., et al. "A ligand-based conjugate solid sensor for colorimetric ultra-trace gold (III) detection in urban mining waste." *Colloids and Surfaces A: Physicochemical and Engineering Aspects* 581 (2019): 123842.
- [84] Zagorodko, Oleksandr, et al. "Surface plasmon resonance (SPR) for the evaluation of shear-force-dependent bacterial adhesion." *Biosensors* 5.2 (2015): 276-287.
- [85] Lu, Cenbin, et al. "Discovery of antagonists of PqsR, a key player in 2-alkyl-4-quinolone-dependent quorum sensing in *Pseudomonas aeruginosa*." *Chemistry & biology* 19.3 (2012): 381-390.

เอกสารนี้เป็นเอกสารที่สงวนไว้สำหรับการใช้งานเพื่อการศึกษาเท่านั้น ไม่อนุญาตให้นำไปใช้ประโยชน์ด้านการค้า  
ไม่ว่ากรณีใดๆ ทั้งสิ้น อีกทั้งห้ามมิให้ดัดแปลงเนื้อหา และต้องอ้างอิงถึงเจ้าของเอกสารทุกครั้งที่มีการนำไปใช้

- [86] Stenberg, Esa, et al. "Quantitative determination of surface concentration of protein with surface plasmon resonance using radiolabeled proteins." *Journal of colloid and interface science* 143.2 (1991): 513-526.
- [87] Zlatanovic, Sanja, et al. "Photonic crystal microcavity sensor for ultracompact monitoring of reaction kinetics and protein concentration." *Sensors and Actuators B: Chemical* 141.1 (2009): 13-19.
- [88] Rupert, Déborah LM, et al. "Determination of exosome concentration in solution using surface plasmon resonance spectroscopy." *Analytical chemistry* 86.12 (2014): 5929-5936.
- [89] Pol, Ewa, et al. "Evaluation of calibration-free concentration analysis provided by Biacore™ systems." *Analytical Biochemistry* 510 (2016): 88-97.
- [90] Shah, Veenita Grover, et al. "Calibration-free concentration analysis of protein biomarkers in human serum using surface plasmon resonance." *Talanta* 144 (2015): 801-808.
- [91] Pattnaik, Priyabrata. "Surface plasmon resonance: applications in understanding receptor-ligand interaction." *Applied biochemistry and biotechnology* 126 (2005): 79-92.
- [92] Bianchi, Nicoletta, et al. "Biosensor technology and surface plasmon resonance for real-time detection of HIV-1 genomic sequences amplified by polymerase chain reaction." *Clinical and Diagnostic Virology* 8.3 (1997): 199-208.
- [93] Thadson, K.; Sasivimolkul, S.; Suvamaphaet, P.; Visitsattapongse, S.; Pechprasarn, S. Measurement precision enhancement of surface plasmon resonance based angular scanning detection using deep learning. *Sci. Rep.* **2022**, *12*, 2052.
- [94] Zhang, J.; Pitter, M.C.; Liu, S.; See, C.; Somekh, M.G. Surface-plasmon microscopy with a two-piece solid immersion lens: Bright and dark fields. *Appl. Opt.* **2006**, *45*, 7977–7986.
- [95] Chu, Y.; Schonbrun, E.; Yang, T.; Crozier, K.B. Experimental observation of narrow surface plasmon resonances in gold nanoparticle arrays. *Appl. Phys. Lett.* **2008**, *93*, 181108.
- [96] Treebupachatsakul, T.; Boosamalee, A.; Chaithatwanitch, K.; Pechprasarn, S. Generalized figure of merit for plasmonic dip measurement-based surface plasmon resonance sensors. *Biomed. Opt. Express* **2022**, *13*, 1784–1800.
- [97] O'Donnell, K.; Mendez, E. Experimental study of scattering from characterized random surfaces. *JOSA A* **1987**, *4*, 1194–1205.

เอกสารนี้เป็นเอกสารที่สงวนไว้สำหรับการใช้งานเพื่อการศึกษาเท่านั้น ไม่อนุญาตให้นำไปใช้ประโยชน์ด้านการค้า  
ไม่ว่ากรณีใดๆ ทั้งสิ้น อีกทั้งห้ามมิให้ดัดแปลงเนื้อหา และต้องอ้างอิงถึงเจ้าของเอกสารทุกครั้งที่มีการนำไปใช้

- [98] Moharam, M.; Grann, E.B.; Pommet, D.A.; Gaylord, T. Formulation for stable and efficient implementation of the rigorous coupled-wave analysis of binary gratings. *J. Opt. Soc. Am. A* **1995**, *12*, 1068–1076.
- [99] Moharam, M.; Gaylord, T. Rigorous coupled-wave analysis of planar-grating diffraction. *JOSA* **1981**, *71*, 811–818.
- [100] Saleem, M.R.; Ali, R. Polymer Resonant Waveguide Gratings. In *Emerging Waveguide Technology*; IntechOpen: London, UK, 2018.
- [101] Nuutinen, T.; Karvinen, P.; Rahomäki, J.; Vahimaa, P. Resonant waveguide grating (RWG): Overcoming the problem of angular sensitivity by conical, broad-band illumination for fluorescence measurements. *Anal. Methods* **2013**, *5*, 281–284.
- [102] Mayet, A.S.; Cansizoglu, H.; Gao, Y.; Ghandiparsi, S.; Kaya, A.; Bartolo-Perez, C.; AlHalaili, B.; Yamada, T.; Devine, E.P.; Elrefaie, A.F. Surface passivation of silicon photonic devices with high surface-to-volume-ratio nanostructures. *JOSA B* **2018**, *35*, 1059–1065.
- [103] Zhang, C.; Zhou, Y.; Mi, L.; Ma, J.; Wu, X.; Fei, Y. High performance of a metal layer-assisted guided-mode resonance biosensor modulated by double-grating. *Biosensors* **2021**, *11*, 221.
- [104] Barer, R.; Tkaczyk, S. Refractive index of concentrated protein solutions. *Nature* **1954**, *173*, 821–822.
- [105] Johnson, P.B.; Christy, R.-W. Optical constants of the noble metals. *Phys. Rev. B* **1972**, *6*, 4370.
- [106] Treebupachatsakul, Treesukon, Siratchakrit Shinnakerdchoke, and Suejit Pechprasarn. "Sensing Mechanisms of Rough Plasmonic Surfaces for Protein Binding of Surface Plasmon Resonance Detection." *Sensors* **23.7 (2023)**: 3377.
- [107] Thadson, K.; Visitsattapongse, S.; Pechprasarn, S. Deep learning-based single-shot phase retrieval algorithm for surface plasmon resonance microscope based refractive index sensing application. *Sci. Rep.* **2021**, *11*, 16289.
- [108] Yang, Z.; Liu, C.; Gao, Y.; Wang, J.; Yang, W. Influence of surface roughness on surface plasmon resonance phenomenon of gold film. *Chin. Opt. Lett.* **2016**, *14*, 042401.
- [109] Agarwal, S.; Prajapati, Y.; Singh, V. Influence of metal roughness on SPR sensor performance. *Opt. Commun.* **2017**, *383*, 113–118.
- [110] Pechprasarn, S.; Chow, T.W.; Somekh, M.G. Application of confocal surface wave microscope to self-calibrated attenuation coefficient measurement by Goos-Hänchen phase shift modulation. *Sci. Rep.* **2018**, *8*, 8547.

เอกสารนี้เป็นเอกสารที่สงวนไว้สำหรับการใช้งานเพื่อการศึกษาเท่านั้น ไม่อนุญาตให้นำไปใช้ประโยชน์ด้านการค้า  
ไม่ว่ากรณีใดๆ ทั้งสิ้น อีกทั้งห้ามมิให้ดัดแปลงเนื้อหา และต้องอ้างอิงถึงเจ้าของเอกสารทุกครั้งที่มีการนำไปใช้

- [111] Wy, Y.; Jung, H.; Hong, J.W.; Han, S.W. Exploiting plasmonic hot spots in Au-based nanostructures for sensing and photocatalysis. *Acc. Chem. Res.* **2022**, *55*, 831–843.
- [112] Sasivimolkul, S.; Pechprasarn, S.; Somekh, M.G. Analysis of open grating-based Fabry–Pérot resonance structures with potential applications for ultrasensitive refractive index sensing. *IEEE Sens. J.* **2021**, *21*, 10628–10636.



เอกสารนี้เป็นเอกสารที่สงวนไว้สำหรับการใช้งานเพื่อการศึกษาเท่านั้น ไม่อนุญาตให้นำไปใช้ประโยชน์ด้านการค้า  
ไม่ว่ากรณีใดๆ ทั้งสิ้น อีกทั้งห้ามมิให้ดัดแปลงเนื้อหา และต้องอ้างอิงถึงเจ้าของเอกสารทุกครั้งที่มีการนำไปใช้

## BIOGRAPHY

Name	Mr. Siratchakrit Shinnakerdchoke
Date of Birth	25 May 2000
Address	80/434 Tippawan Village Soi 24, Theparak Road, Bang Mueng Sub-district, Mueng District, Samutprakarn, 10270
Education	2021 Bachelor of Engineering, Biomedical Engineering (First Class Honor), King Mongkut's Institute of Technology Ladkrabang
Specialized field	1) Biosensor 2) Optics
Publication and Awards	
2021	- Publication "Analysis of Effects of Surface Roughness on Sensing Performance of Surface Plasmon Resonance Detection for Refractive Index Sensing Application" in MDPI Sensors journal.
2022	- Publication "Cuff-Less Blood Pressure Prediction from ECG and PPG Signals Using Fourier Transformation and Amplitude Randomization Preprocessing for Context Aggregation Network Training" in MDPI Biosensors journal. - Publication "Performance Analysis of Machine Learning Models for Angular Interrogation of Surface Plasmon Resonance" in BMEiCON 2022.
2023	- Publication "Sensing Mechanisms of Rough Plasmonic Surfaces for Protein Binding of Surface Plasmon Resonance Detection" in MDPI Sensors journal.

เอกสารนี้เป็นเอกสารที่สงวนไว้สำหรับการใช้งานเพื่อการศึกษาเท่านั้น ไม่อนุญาตให้นำไปใช้ประโยชน์ด้านการค้า  
ไม่ว่ากรณีใดๆ ทั้งสิ้น อีกทั้งห้ามมิให้ดัดแปลงเนื้อหา และต้องอ้างอิงถึงเจ้าของเอกสารทุกครั้งที่มีการนำไปใช้